Numerical Simulation of Wave Focusing and Scattering in Shock Wave Lithotripsy

Thesis by

Jeff Krimmel

In Partial Fulfillment of the Requirements

for the Degree of

Doctor of Philosophy

California Institute of Technology

Pasadena, California

2010

(Defended March 22, 2010)

In loving memory of my grandmother, Ruby A. Brown.

Acknowledgments

First and foremost, I need to thank my advisor, Tim Colonius, for expertly guiding me through the many ups and downs that have led to this point. Of course I have learned a great deal about fluid mechanics generally, and shock wave lithotripsy specifically, under Tim's guidance. But more importantly, I have also begun to learn what is required to become a great engineer, which is something I hope to carry with me far into the future.

I also need to thank the members of my faculty committee, Dr.s Chris Brennen, John Dabiri, and Joe Shepherd. I decided to pursue my graduate studies at Caltech for a multitude of reasons, one of which was to surround myself with scientists and engineers of the highest caliber who would help drive my professional development. My faculty committee members met and wildly exceeded my expectations, and I feel honored, humbled, and privileged to have been able to pursue my research endeavors under their supervision.

The Computational Flow Physics Group, the research group directed by Tim and to which I belong, has provided a great work environment and support system for me during my time at Caltech. Former members Guillaume Bres, Jennifer Franck, Kristjan Gudmundsson, Eric Johnsen, Hongyu Ran, Kunihiko (Sam) Taira, and Michel Tanguay, and current members Keita Ando, Rick Burnes, Sebastian Cabrera, Vedran Coralic, Matthew Inkman, and Won Tae Joe, have been world-class colleagues and have made my years of research much more pleasurable than they otherwise would have been. I particularly need to thank Jen for all of her help administering the various computational resources required by our group. She was a tremendous help on that front.

I have had the great fortune to befriend a large number of wonderful people since I have been in California. Though there are too many to name individually, I want to thank all of them for making life that much more enjoyable and, at times equally important, that much less stressful. I will value

these friendships forever.

Finally, I need to thank my friends and family, people who have been supportive of me since well before my arrival in California. Specifically, my friendship with Bobby and Elizabeth Wallace means more to me than I will ever be able to express in words. They have been with me through the highs and the lows, and their support and encouragement has been incredibly helpful throughout my time at Caltech. My grandfather, Albert D. Brown, and all of my extended family have been uniformly supportive of my efforts. Frankly whatever success I achieved at Caltech simply would not have been possible if not for the love and support of my brother and his wife, Jeremy and Meredith Krimmel, and my parents, James and Judy Krimmel. I have had the amazing fortune of being surrounded by the most wonderful people imaginable, and not for a day will I ever take that for granted.

Abstract

In this work we simulate shock wave focusing and scattering that occurs during shock wave lithotripsy, a noninvasive medical treatment for kidney stone disease. Shock waves are generated outside the body of the patient and are focused at the kidney stone with the intention of pulverizing the stone while it remains inside the patient. The patient can then ostensibly pass the debris naturally. We use a multidimensional second-order method of the Godunov type with slope limiters and shock capturing capability to solve the inviscid Euler equations. Because we begin with the fundamental statements of conservation of mass, momentum, and energy, we simulate all the relevant acoustics occurring during a typical treatment.

Lithotripters, the machines that generate and focus shock waves, can be classified according to the mechanism of shock generation. In this work, we simulate three different types of lithotripters: electrohydraulic, piezoelectric, and electromagnetic. We choose one representative of each lithotripter type: the Dornier HM3, a research piezoelectric lithotripter array, and the XX-Es, respectively. We first study a model of the *in vitro* setting for each lithotripter, where shock waves are generated and focus in a bath of pure water. Next, we introduce different heterogeneous materials near the focus of the lithotripter to model the effect of the body of an actual patient, i.e., the *in vivo* condition. We use two approaches in this modeling effort. One approach is to use simple geometrical models for the body cavity and kidney that we created ourselves. The other approach is to import real anatomical data made available from the VOXEL-MAN Group.

In studying the focal region acoustics, we specifically examine the maximum calculated pressures. These pressures represent the forces that will ultimately cause the kidney stone to break. We also study the pulse intensity integral, i.e., the energy density carried by the focusing shock wave. In addition to these pressures and energy densities, we are interested in investigating how soft tissue in the focal

region may potentially be damaged by the resulting wavefields. We isolate two mechanisms that are thought to be important in soft tissue injury: shearing and cavitation. We calculate estimates for the maximum principal normal and shear strains in the focal region in addition to the corresponding strain rates and use these as metrics for the potential for damage via shearing. We study the calculated negative pressure fields in this region as a surrogate for potential damage caused by cavitation.

We find that our simple geometrical anatomical models cause little deviation from the acoustics observed in a water bath. However, when the real anatomical data of the VOXEL-MAN Group is used, the fields of the various relevant flow quantities become more highly oscillatory and produce secondary extrema that could produce damage not predicted from the water bath case. In addition to the conclusions from our own work, we discuss how our results motivate future studies that will hopefully help elucidate specific mechanisms by which kidney stones break and soft tissue becomes damaged.

Contents

List of Figures

List of Tables

Glossary

$\boldsymbol{f}$	flux vector in the axial direction
$\boldsymbol{g}$	flux vector in the radial direction
$\boldsymbol{q}$	state vector of conserved variables
$\boldsymbol{s_g}$	geometric source term vector
γ	parameter in stiffened gas equation of state
ρ_0	atmospheric fluid density
ρ	fluid density
c_0	small signal sound speed
e_t	total specific energy
e	specific internal energy
p_0	atmospheric fluid pressure
p_s	parameter in stiffened gas equation of state
p	fluid pressure
r	radial coordinate
t	time
u	fluid axial velocity
v	fluid radial velocity
x	axial coordinate

Chapter 1

Introduction

1.1 Motivation

Extracorporeal shock wave lithotripsy is a noninvasive treatment modality where shock waves are generated outside the body and focused at the site of the stone[15, 14]. Shock wave lithotripsy was first developed and used clinically in the early 1980s. Over the years its use and popularity has increased. A lithotripter is the machine used to both generate and subsequently focus the shock wave(s). A coupling agent of some form is used to transfer as much energy to the stone site as possible, and an imaging mechanism helps locate the stone to improve aiming of the shock waves.

It is well known that highly sought improvements in newer lithotripters have been difficult to realize[3]. It is, however, not well known exactly why various design changes have not led to the enhanced efficacies expected with an evolving design process. Our motivation is to improve the understanding of the acoustics occurring during a typical shock wave lithotripsy treatment. By studying the spatial distribution and temporal evolution of important flow variables like pressure and energy, we will explore the acoustic footprint of various lithotripters and help elucidate the important mechanisms that contribute both to stone comminution and tissue injury.

1.2 Background

Before we provide details of our investigation of shock wave lithotripsy, we will discuss kidney stone disease and the most often used treatments. We will also describe how shock wave lithotripters work and discuss modern design changes.

1.2.1 Kidney Stone Disease

Approximately 12% of men and 5% of women will develop a kidney stone over the course of their lifetime [20]. It is estimated the cost of urolithiasis in the United States is approximately $2 billion annually[64]. Unfortunately kidney stone disease is often accompanied with other health issues. For example, the links between stone disease and coronary heart disease[44] and hypertension[60] have been studied. Much effort has been undertaken to identify risk factors associated with stone disease in the hope that more effective preventative measures can subsequently be developed[77, 26].

The specific mechanisms by which kidney stones form are still largely unknown[34]. Approximately 80% of stones are composed of calcium oxalate and calcium phosphate. The remaining stones are made mostly of struvite or uric acid. Stones less than 5 mm in diameter are likely to pass naturally through the body. Stones with diameters between 5 and 7 mm have approximately 50% chance to pass, while stones with diameters larger than 7 mm almost always require treatment[20]. Various treatment modalities exist for large kidney stones: percutaneous nephrolithotomy, intracorporeal stone fragmentation, and (extracorporeal) shock wave lithotripsy, among others[34].

In percutaneous nephrolithotomy, a small incision is made in the patient's back. Via this incision, a hollow tube is inserted directly into the kidney. Either whole stones are removed by being carried back out through the inserted tube, or in some cases the stone is first pulverized and the fragments are subsequently removed. Intracorporeal stone fragmentation involves the *in vivo* application of energy to fragment stones, often through endoscopic techniques. Some examples of energy sources are ultrasound transducers, spark sources, mechanical pulverizers, and lasers. The details of an extracorporeal shock wave lithotripsy treatment are discussed in the following subsection.

1.2.2 How Shock Wave Lithotripsy Works

Early lithotripters often used an electrohydraulic mechanism to generate shock waves. The lithotripter consisted of a pair of electrodes submerged in water whose gap was positioned at one focus of an ellipsoidal bowl. The patient was oriented such that the kidney stone was positioned at the second focus of the bowl. Current was passed through the electrodes, and the resulting spark across the electrode gap vaporized the nearby water and created a spherically diverging shock wave. The shock

wave reflected from the ellipsoidal bowl and focused at the stone[18].

Another class of lithotripters generates shocks via the action of piezoelectric elements. Often the piezoelectric elements line the surface of a rigid spherical cap[88, 16]. Current is then passed through the elements, causing their surfaces to displace from their rest positions. This surface motion induces a nonlinear acoustic pulse in the surrounding fluid that eventually becomes a shock wave before arriving at the geometrical focus (i.e., the stone site).

A third class of lithotripters use electromagnetic mechanisms to generate shock waves. One approach is to use a diaphragm attached to a planar coil. When current is passed through the coil, the diaphragm displaces, generating a planar nonlinear acoustic pulse. An acoustic lens is then used to focus the pulse at the site of the stone[82]. A second approach is to use a spherically shaped coil to generate a nonlinear pulse that is self-focusing[32]. In this case, the dynamics are similar to the previously described class of piezoelectric lithotripters.

When lithotripter technology was first introduced, most lithotripters were submerged in a water bath where the patient was also placed. The water bath provided the acoustic coupling of the extracorporeally generated shocks and the kidney stone in the body of the patient. As lithotripsy matured, the dry head configuration became more popular. In this configuration, the shock wave generation mechanism is enclosed in a rubber bag which is filled with a waterlike fluid. During treatment the dry head assembly is positioned against the body of the patient. A coupling gel is used between the dry head and the body to make the wave path as acoustically homogeneous as possible[68].

1.3 Physics

In this section, we discuss the fundamental physics observed during a typical shock wave lithotripsy statement. We will first discuss shock focusing in general and how the geometry of a lithotripter varies from the canonical experimental treatments. We then move on to discuss the proposed mechanisms by which kidney stones break and soft tissue is damaged.

1.3.1 Shock Focusing

The focusing of a lithotripter pulse has much in common with the focusing of a planar shock front, as described in detail by Sturtevant and Kulkarny[75]. The lithotripter shocks are classified as weak. One metric of the shock strength is

$$\epsilon = \frac{u^*}{c_s}, \tag{1.1}$$

where u^* is the velocity of the fluid processed by the shock and c_s is the speed of the shock front. Conservatively we can take c_s to be the small signal sound speed of the medium. Using this metric, for our simulations, the maximum shock strength for any of the lithotripters is approximately 0.02.

Sturtevant and Kulkarny studied multiple cases of shock focusing, and the lithotripsy case is most like the case where a weak planar shock is reflected from a concave wall, eventually forming a perfect focus. The Sturtevant and Kulkarny setup differs from the lithotripsy arrangement in a number of ways, at least two of which are fundamental. First, Sturtevant and Kulkarny study the case where a planar shock reflects from a paraboloidal surface, resulting in focusing at a point. In the lithotripsy case, specifically for the Dornier HM3, a spherical shock reflects from an ellipsoidal surface, also focusing at a point. For the piezoelectric and electromagnetic lithotripters we study, the motion of a spherical membrane induces a self-focusing shock front. This difference is shown in figure 1.1. Second, the profile of the planar shock consists of just a shock front. In the lithotripsy case, the initial shock front is immediately followed by an expansion. This added feature of the initial waveform leads to differences in the character of the focused wave. The different profiles are shown in figure 1.2.

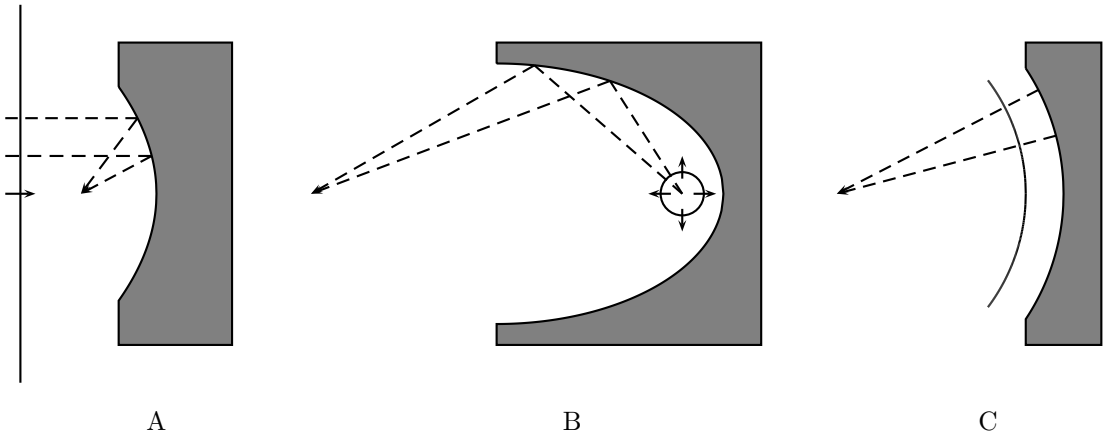

Figure 1.1: Planar shock front reflecting from parabaloidal surface (A). Spherically diverging shock front reflecting from ellipsoidal surface (B). Self-focusing shock front originating from boundary motion of spherical diaphragm (C).

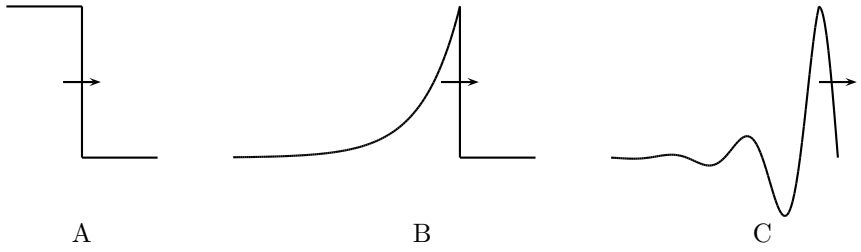

Figure 1.2: Initial waveform profile for planar shock as studied by Sturtevant and Kulkarny (A), spherical shock as studied in this work for the case of the Dornier HM3 (B), and self-focusing shock as studied in this work for the case of the piezoelectric lithotripter array and XX-Es (C).

1.3.2 Stone Pulverization

The pressure measured at the focus of a lithotripter as a function of time generally shows a nearly instantaneous pressure increase as a result of the arrival of the shock wave followed by an expansion region that produces negative pressures. The pressure then reaches equilibrium at atmospheric values. In most cases the pulse is between 5 and 15 μs in duration. Some lithotripters produce multiple compression and rarefaction phases in a single pulse. Waveforms with leading negative phases have also been observed. Figure 1.3 shows a modeled form of the focal pressure waveform measured in an electrohydraulic lithotripter[17].

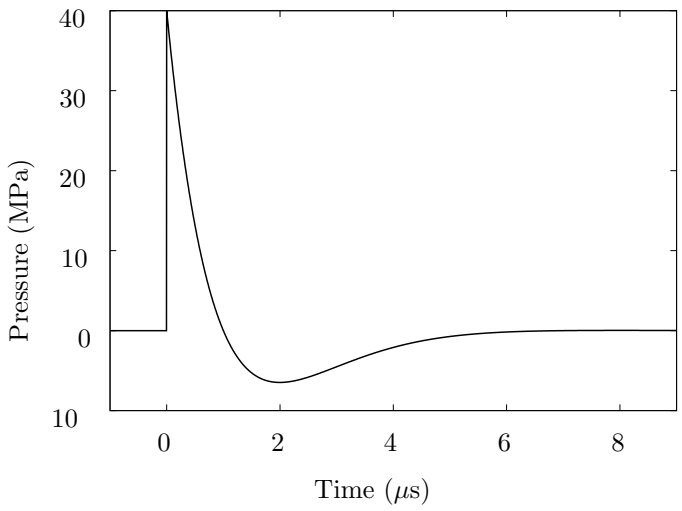

Figure 1.3: Modeled form of the focal pressure waveform measured in an electrohydraulic lithotripter.

Kidney stones are brittle composite materials that are stronger under compression than in tension. The fundamental description of how shock waves breaks stones involves the nucleation of microcracks which grow, merge, and under repeated loadings eventually cleave the stone [59]. No consensus yet exists regarding the details of how exactly the microcracks are nucleated or grow. Several different mechanisms has been proposed and shown to be important in various circumstances. Generally speaking, stones break either as a direct result of interaction with the shock wave or indirectly via cavitation activity induced by the shock. In the case of direct interaction, two primary mechanisms have been acknowledged: spallation and circumferential squeezing.

In the case of spallation, the waveform is transmitted into the stone but upon reflection from the acoustically soft distal stone surface, the waveform inverts. The inverted compression phase interacts constructively with the rarefaction phase that has yet to reflect from the surface, producing a maximum tensile stress. The stone experiences this maximum tensile stress at a distance $l = c_l \Delta t/2$ from the distal surface, where c_l is the longitudinal wave speed in the stone and Δt is the temporal duration between the peak positive and negative pressure amplitudes[69]. Using $c_l = 3000$ m/s and $\Delta t = 2$ μs, reasonable values for a kidney stone and lithotripter pulse, a maximum tensile stress is expected approximately 3 cm from the distal end of the stone, roughly in agreement with experimental observations.

Circumferential squeezing occurs when the incoming shock wave has a broader spatial extent than the stone in the direction transverse to its direction of propagation[33]. The portion of the wavefront

transmitted in the stone races ahead of the portion outside the stone because the longitudinal wave speed in the stone is greater than the sound speed in the surrounding liquid. The portion of the wavefront encircling the stone's surface squeezes the stone quasi-statically.

1.3.3 SWL-induced Tissue Damage

The hope is that wave amplitudes are sufficiently low away from the stone so that soft tissue is not damaged as a result of SWL treatment. In practice, various degrees of renal trauma are often observed and long-term complications can potentially result[35]. Hematuria (blood in the urine) is observed in nearly every patient, which is indicative of urinary tract damage[2]. A nontrivial portion of patients also suffer from hemorrhage and/or edema[52]. Most damage is seen in the focal region and largely consists of damaged blood vessels that produce the observed bleeding and blood clots[30, 10].

Like the case for stone comminution, no consensus yet exists regarding exactly how shock waves damage tissue, though it is generally believed damage occurs as a result of shearing and/or cavitation dynamics, both being induced by the focusing shock wave[23]. One proposal is that cavitation micro-jetting attacks the stone surface, and possibly surrounding tissue, much like a solid projectile[25]. It has been observed that suppressing cavitation does indeed reduce observed tissue damage[36]. When a pressure release reflector was used with the Dornier HM3 in place of a rigid reflector, cavitation fields were weakened and less pitting of aluminum foil samples was observed [5]. Cavitation has indeed been detected both in urine and in renal tissue during a SWL treatment[6] and could explain a nontrivial portion of the observed stone comminution and tissue injury.

Another proposed mechanism of tissue injury is shearing in the focal region resulting from the dynamics of the focusing shock wave. Experiments with thin membranes have shown failure in fatigue as a consequence of shearing[48]. Further experiments with red blood cells in a cavitation-free environment show cell lysis in varying degrees of shear[58]. A simulation of the renal vasculature has indicated it is possible shear accumulates with successive shocks and could be responsible for the initiation of tissue damage in the parenchyma[37]. While these experimental and numerical efforts have demonstrated the capacity of shock-induced shearing to damage tissue, no conclusive observations have been made regarding the relative strength of the proposed damage mechanisms or how they may differ in different

SWL treatments.

1.4 Contributions and Overview

The significant contributions of this thesis are listed below.

- Multi-dimensional simulation of different types of lithotripters using a single numerical framework.
- Introduction of heterogeneous materials, and hence nonuniform acoustic impedances, to study the resulting shock dynamics without a restriction to *in vitro* conditions.
- Leveraging the output of the fluid mechanics calculations to make estimates of the soft tissue damage potential of the focal region acoustics.
- Using the output from the Rayleigh-Plesset equation for single bubble dynamics to model shock wave generation by the vaporization of water in an electrohydraulic lithotripter.
- Integration of a method to account for ultrasonic absorption by soft tissue into the numerical framework used to solve the classical inviscid Euler equations.

In chapter 2 we discuss the computational methods we use to simulate the behavior of different classes of lithotripters (electrohydraulic, piezoelectric, and electromagnetic). In chapter 3 we explore the case of *in vitro* SWL. Much of the previous work done in SWL simulation has concentrated on this case. We discuss the rich wave mechanics occurring in an open water bath along with the case where a stonelike material is placed in the focal region of each lithotripter. In chapter 4 we move on to the case where a tissuelike material surrounds the focal region. We explore the acoustical phenomena of scattering and absorption, because these phenomena occur in the *in vivo* propagation of shock waves. In chapter 5, we discuss potential mechanisms of tissue injury. Using our results for the *in vitro* case, we make estimates regarding where cavitation damage may be most likely to occur and where the effect of strain is strongest in our tissuelike materials. Finally, we make concluding remarks in chapter 6.

Chapter 2

Computational Infrastructure

2.1 Previous Work

Most simulations of shock wave lithotripsy to date have involved simulating the acoustics in an electrohydraulic lithotripter like the Dornier HM3. These models have utilized geometrical acoustics[53], the KZK equation [85, 54], and geometrical shock dynamics[80]. Geometrical acoustics is a linear theory and operates in the high frequency limit. Waves travel along rays normal to the wavefront. Converging rays yield infinite amplitudes at ray intersections in this theory, and thus the theory breaks down near a focus. Hamilton uses this theory to calculate the transient axial solution for a geometry like that of an electrohydraulic lithotripter [45]. The KZK equation is an augmented form of the Burgers equation that accounts for weak nonlinearity, diffraction (in the parabolic approximation), and absorption in directional sound beams. This theory performs better than geometrical acoustics near a focus, however it is also restricted to high frequencies and assumes quasi-one-dimensional propagation of the sound beam. Averkiou and Cleveland use this approach to model the pressure field of an electrohydraulic lithotripter[4]. Geometrical shock dynamics is a nonlinear theory and assumes the shock front propagates through ray tubes. An expression is derived relating the local shock Mach number to the ray tube area, and the tube area is never allowed to vanish as in geometrical acoustics. As a result, geometrical shock dynamics avoids the problem of infinite amplitudes. The theory does, however, neglect the interaction of the flow behind the shock with the shock itself. Cates and Sturtevant use geometrical shock dynamics to study shock focusing in geometries similar to that of the Dornier HM3[13].

2.2 Physical Model

In order to simulate the interesting wave mechanics occurring during a shock wave lithotripsy treatment, we solve the fully nonlinear Euler equations in an axisymmetric geometry:

$$\frac{\partial \boldsymbol{q}}{\partial t} + \frac{\partial \boldsymbol{f}}{\partial x} + \frac{\partial \boldsymbol{g}}{\partial r} = \boldsymbol{s_g}, \tag{2.1}$$

where t is time, x is the axial coordinate, r is the radial coordinate, $\boldsymbol{q}$ is the state vector of conserved variables, $\boldsymbol{f}$ and $\boldsymbol{g}$ are the flux vectors in the axial and radial directions, respectively, and $\boldsymbol{s_g}$ is the geometrical source term vector:

$$\boldsymbol{q} = \begin{bmatrix} \rho \\ \rho u \\ \rho v \\ \rho e_t \end{bmatrix}, \quad \boldsymbol{f} = \begin{bmatrix} \rho u \\ \rho u^2 + p \\ \rho uv \\ (\rho e_t + p)\, u \end{bmatrix}, \quad \boldsymbol{g} = \begin{bmatrix} \rho v \\ \rho uv \\ \rho v^2 + p \\ (\rho e_t + p)\, v \end{bmatrix}, \quad \boldsymbol{s_g} = \begin{bmatrix} -\frac{\rho v}{r} \\ -\frac{\rho uv}{r} \\ -\frac{\rho v^2}{r} \\ -\frac{(\rho e_t + p)v}{r} \end{bmatrix}. \tag{2.2}$$

In this formalism, ρ is the fluid density, u and v are the fluid velocities in the axial and radial directions, respectively, e_t is the total specific internal energy, and p is the pressure.

The total specific energy e_t has the following definition:

$$\rho e_t = \rho e + \frac{1}{2}\rho \left(u^2 + v^2\right), \tag{2.3}$$

where e is the specific internal energy. We require an equation of state to close the system (2.1), relating ρe to known quantities in the state vector. In this work, we simulate shock propagation in fluids, e.g., water in the *in vitro* case and a soft tissuelike fluid in the *in vivo* case. As a result, we choose the stiffened gas equation of state[46]:

$$\rho e = \frac{p + \gamma p_s}{\gamma - 1}. \tag{2.4}$$

For a perfect gas, γ is the ratio of specific heats and $p_s = 0$, meaning a stiffened gas is a perfect gas

already experiencing a prescribed overpressure. For liquids, as in our case, the γ and p_s terms control the stiffness, and hence the sound speed, of the medium. In this work, for water we use $\gamma = 5.5$ and $p_s = 4036$ atm, yielding a small signal sound speed c_0= 1500 m/s when combined with an atmospheric density of ρ_0= 1000 kg/m^3. These values are most similar to those chosen by Shyue[72] and close to those of other researchers[72, 70, 21, 78, 43, 73]. The thermodynamics of the stiffened gas equation of state have been discussed elsewhere[51].

2.3 Numerical Method

We use a second-order finite volume Godunov method with slope limiters to solve (2.1). Specifically, we use the freely available AMROC (Adaptive Mesh Refinement in Object-oriented C++) framework already documented in the literature [28, 29, 27] and used in other studies[62, 56]. AMROC provides an implementation of the block structured adaptive mesh refinement of Berger and Oliger[7] proposed by Berger and Collela [8]. Arbitrary geometries are handled by a level set-based ghost fluid method.

We use three grid levels for all of our simulations. The base, or first level, grid is spatially uniform with a resolution of 0.5 mm. The second level grid is a factor of two finer than the first level grid, and the third level grid is a factor of sixteen finer than the first level grid. Thus the smallest spatial scale in our simulations is 31.25 μm. The smallest temporal scale is then 18.75 ns. The grid is refined when the difference between normalized densities in adjacent cells is greater than a prescribed threshold. Grid convergence was established by noting minimal changes in the computed results when resolutions were increased by 50%.

2.4 Dornier HM3

The electrohydraulic lithotripter we model is the Dornier HM3, which is considered the gold standard of shock wave lithotripters and has been both used and studied extensively since SWL first became popular[24], [74]. The HM3 consists of a spark gap formed by a pair of electrodes positioned at one focus (F1) of a truncated ellipsoidal reflector[18]. The kidney stone is positioned at the second focus (F2) of the reflector. Figure 2.1 shows the computational domain we use in our simulations of the HM3,

while figure 2.2 shows the relevant geometry.

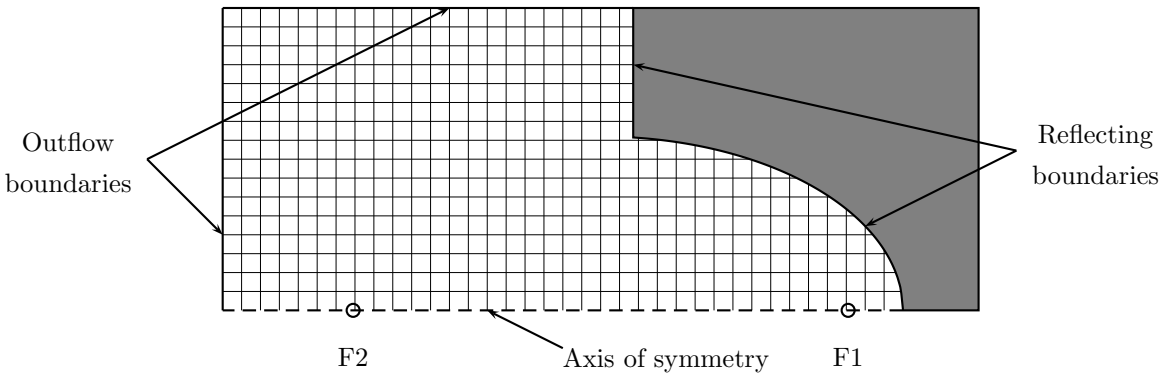

Figure 2.1: The computational domain used in this work to simulate the Dornier HM3 electrohydraulic lithotripter. A level set method was used to construct the reflecting boundaries.

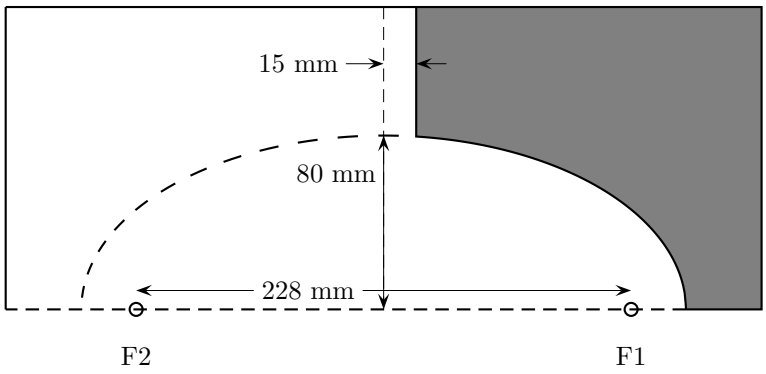

Figure 2.2: Geometry of the ellipsoidal reflector used in this work.

A capacitor is used to pass current through the electrodes surrounding F1 such that the water in the gap is ionized, resulting in the rapid growth of a vapor bubble cluster. The expansion of this vapor region produces an outgoing wavefront that is approximately spherical. The spherical wavefront reflects from the surface of the ellipsoid and diffracts past its truncated edge, creating a wavefront that focuses in the neighborhood of the second focal point of the reflector. We will now describe how we handle this shock wave generation process numerically.

2.4.1 Model Bubble at F1

We mimic the vaporization event by first assuming a model vapor bubble rests at F1. This model bubble is designed to reproduce to an approximate degree the behavior of the physical vaporization bubble originating in the spark gap. As in the work of Church[17], we use the Gilmore equation of bubble dynamics to compute the radius $R \equiv R(t)$ and wall velocity $\dot{R} \equiv \dot{R}(t) = dR/dt$ at time t of the model bubble as it is impulsively forced,

$$R\left(1-\frac{\dot{R}}{c}\right)\frac{\dot{R}}{dt}+\frac{3}{2}\left(1-\frac{\dot{R}}{3c}\right)\dot{R}^2=\left(1+\frac{\dot{R}}{c}\right)H+\frac{\dot{R}}{c}\left(1-\frac{\dot{R}}{c}\right)R\frac{dH}{dR}, \tag{2.5}$$

where H, the enthalpy of the liquid, is given as

$$H \equiv H(t) = \int_{p_\infty(t)}^{p(R(t))} \frac{dp}{\rho}. \tag{2.6}$$

Here $p_\infty(t)$ is the pressure in the liquid at infinity at time t, $p(R(t))$ is the liquid pressure at the bubble wall, and p and ρ are the time-varying liquid pressure and density, respectively. The formalism is further described in Church[17].

Now we need an expression for the pressure in the liquid at the bubble wall[11], $p(R(t))$:

$$p(R(t)) = p_b(t) + \frac{2S}{R(t)}. \tag{2.7}$$

Here $p_b(t)$ is the uniform pressure inside the bubble and S is the surface tension coefficient. The pressure inside the bubble is then

$$p_b(t) = p_{sv} + p_{g,0}R(t)^{-3\gamma}, \tag{2.8}$$

where p_{sv} is the saturated vapor pressure and $p_{g,0}$ is the pressure of the gas that comprises the microbubble at $t = 0$. This gas pressure is

$$p_{g,0} = p_\infty(0) - p_{sv} + \frac{2S}{R_0}. \tag{2.9}$$

The strength of the impulse, $p_\infty(t)$, is chosen so that the collapse time of the model bubble is in general agreement with measured values [87], approximately 2.65 ms. We choose an equilibrium bubble radius $R_0 = 10\mu$m. We force the growth of this bubble by prescribing a decrease in the pressure in the surrounding liquid of the form

$$p_\infty(t) = p_{\text{atm}} + p_\infty \exp\left[-\left(\frac{t-t_0}{b}\right)^2\right], \tag{2.10}$$

where $p_\infty = -4500$ atm, $t_0 = 5\mu$s, and $b = 1\mu$s.

2.4.2 Form of Mass and Energy Sources

In the study of linear acoustics, a simple source radiates sound equally in all directions. The excess pressure resulting from the action of such a source is given as[57],

$$p - p_0 = \frac{\dot{q}_m(t - r/c)}{4\pi r}, \tag{2.11}$$

where p is the observed fluid pressure, p_0 and ρ_0 are ambient values of fluid pressure and density, $q_m(t) = \rho_0 q_v(t)$ is the rate of mass outflow from the source, $q_v(t)$ is the rate of volume outflow from the source, r is the distance from the source to the point of observation, and c is the small signal speed of sound in the fluid. In our case, we calculate the mass of fluid the model bubble at F1 displaces,

$$q_m(t) = \rho_\infty \dot{V}(t), \tag{2.12}$$

where $\dot{V}(t) = dV(t)/dt$ is the rate at which the volume of the bubble is growing, and $V(t) = 4/3\pi R(t)^3$ is the current volume of the bubble. This rate of mass outflow is used as a mass source in our continuity equation,

$$\frac{\partial \rho}{\partial t} + \nabla \cdot (\rho \vec{u}) = S_m(\vec{x}, t), \tag{2.13}$$

where

$$S_m(\vec{x},t) = \frac{q_m(t)}{V(t)} = 3\rho_\infty \frac{\dot{R}(t)}{R(t)}. \tag{2.14}$$

This expression holds for values of $\vec{x}$ within the bubble volume. Outside this volume $S_m(\vec{x},t) = 0$. In this sense, we have computed the rate of mass outflow from the source, $q_m(t)$, and we are distributing this added mass over a volume equal to that of the model bubble, $V(t)$. The mass being "added" by the action of the model bubble at F1 carries with it added energy, and as a result we have a source term in our energy equation,

$$\frac{\partial \rho e_t}{\partial t} + \nabla \cdot (\rho e_t + p)\,\vec{u} = S_e(\vec{x},t), \tag{2.15}$$

where again this expression holds for $\vec{x}$ within the bubble volume but vanishes for points outside this volume. Because we have appealed to linear acoustics in the motivation of the form of our mass source, we can use the acoustic relation,

$$e_t' = \frac{c^2}{\gamma - 1}\rho', \tag{2.16}$$

where e_t' and ρ' are small fluctuations in the specific total internal energy and density, respectively, to determine the form of the energy source,

$$S_e(\vec{x},t) = \frac{c^2}{\gamma - 1} S_m(\vec{x},t). \tag{2.17}$$

Figure 2.3 shows $R(t)$ and $\dot{R}(t)$ for a bubble whose equilibrium radius is 10 μm and which was impulsively forced to yield a 2 ms collapse time. The plots show the dynamics over the first 30 μs of the bubble's growth cycle, because this duration is the one in which the spherically outgoing shock wave is generated.

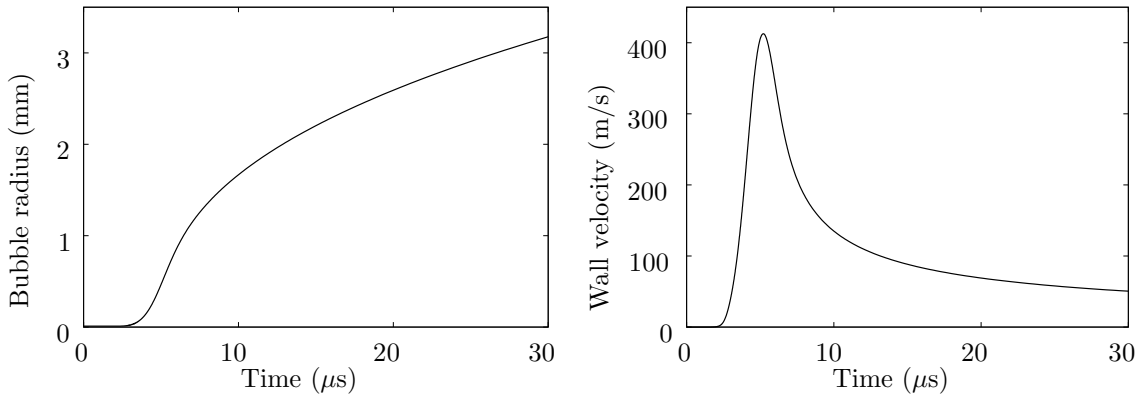

Figure 2.3: Bubble radius $R(t)$ versus time (left) and bubble wall radial velocity $\dot{R}(t)$ versus time (right) for an impulsively forced 10 μm bubble with a 2 ms collapse time.

2.5 Piezoelectric Lithotripter Array

Chitnis et al. use a 170-element piezoelectric lithotripter array to study various customized acoustic fields[16]. The elements line the inner surface of a 150 mm radius spherical cap with an aperture diameter of 154 mm. The firing of each element is independently controlled, and by fixing the relative timing of the firing of various elements, the resulting acoustic field was customized for various cases. Figure 2.4 shows the placement of the 170 elements in the spherical cap. Figures 2.5 and 2.6 show the computational domain we use for this lithotripter and the relevant geometry, respectively.

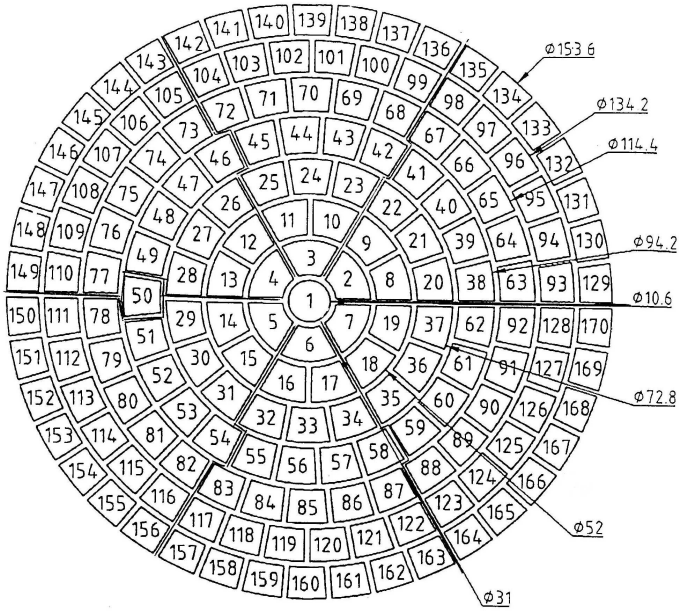

Figure 2.4: A diagram of the placement of the 170 elements forming the piezoelectric lithotripter array.

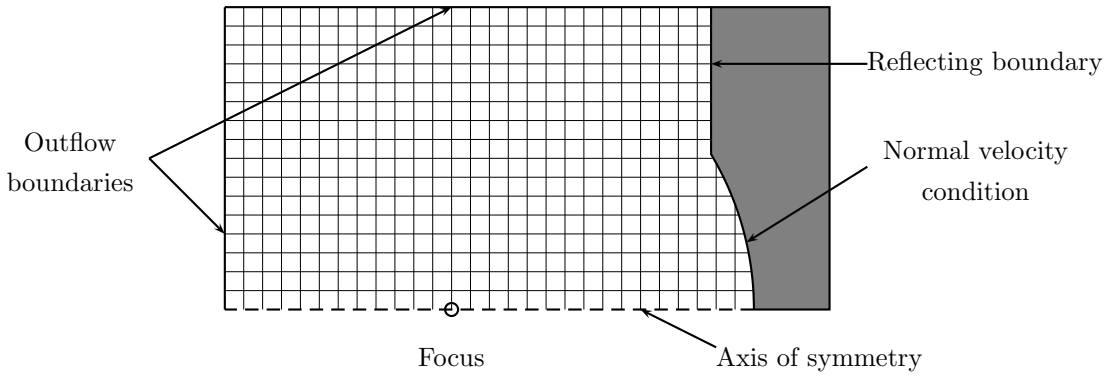

Figure 2.5: The computational domain used in this work to simulate the piezoelectric lithotripter array. A level set method was used to construct the reflecting boundary and the boundary with the normal velocity condition.

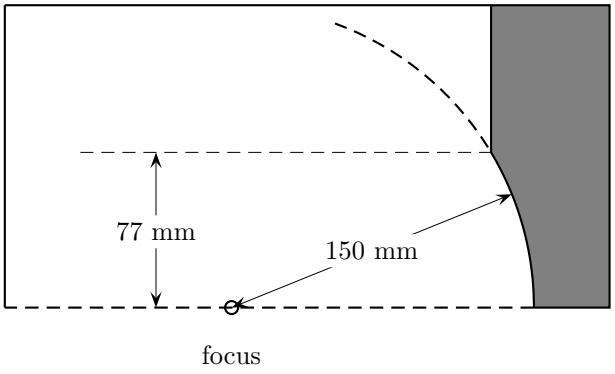

Figure 2.6: Geometry of the piezoelectric lithotripter array used in this work.

Parag Chitnis and Robin Cleveland provided us with several sets of experimental measurements for this lithotripter array. One set is the recorded pressure versus time at the focus for the case where the center element (element #1) is fired alone. The peak positive and negative pressures in this case are approximately ±0.2 MPa. We used these measurements to calculate an estimate for the displacement of the element's surface as a function of time using the Rayleigh integral[65],

$$p(\vec{x},t) = \frac{\rho_0}{2\pi} \int\int \frac{\dot{v}_n(x_s, y_s, t - R/c)}{R} dx_s dy_s, \tag{2.18}$$

where $p(\vec{x},t)$ is the measured pressure at the point with position vector $\vec{x}$ at time t, ρ_0 is the ambient fluid density, $\dot{v}_n$ is the normal velocity of the element's surface, c is the small signal speed of sound, and R is the distance from the point on the element's surface (x_s, y_s) to the point of observation,

$$R^2 = z^2 + (x - x_s)^2 + (y - y_s)^2. \tag{2.19}$$

In this formalism, the element's surface resides in the $z = 0$ plane. With the measured values of $p(\vec{x},t)$, we can compute values of $\dot{v}_n(t)$ and use them as a boundary condition for each ring of elements in our axisymmetric geometry. Figure 2.7 shows a comparison of the experimental measurements with our numerical results for the case where the center element is fired alone using $\dot{v}_n(t)$ as the boundary condition.

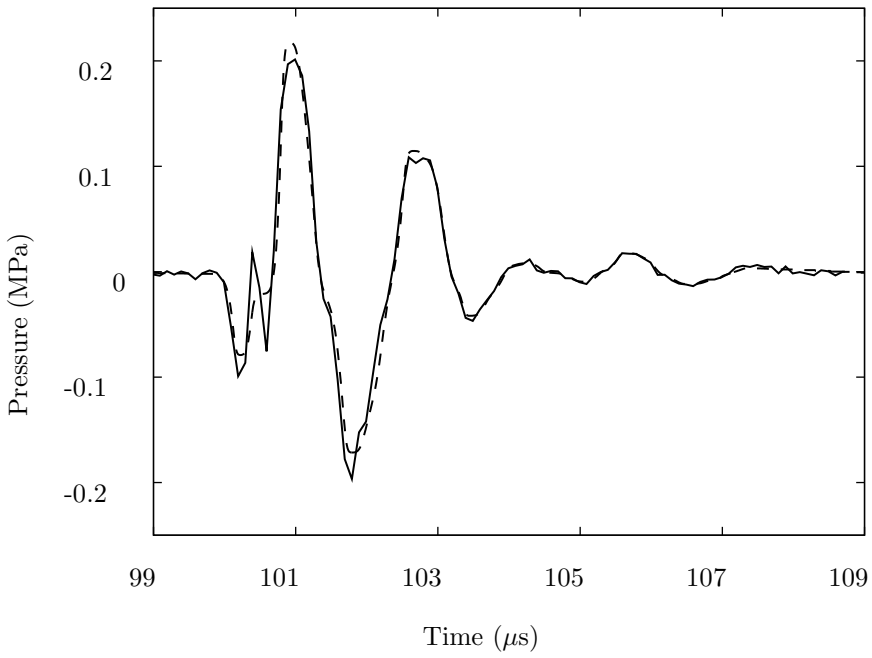

Figure 2.7: Pressure versus time for the case where only the center element of the piezoelectric lithotripter array is fired. Experimental measurements (———); computational results (– – –).

2.6 XX-Es

The XX-Es is an electromagnetic lithotripter comprised of a self-focusing electromagnetic "wide focus" shock-wave generator designed at the University of Stuttgart[32]. This generator was used in Xixin lithotripters and tested in China. A spherically shaped solenoid with a 200 mm radius of curvature and a 120 mm aperture diameter is used to displace a copper diaphragm, generating a self-focusing shock wave that first travels through a water-filled rubber coupling cushion and then into the body. Figures 2.8 and 2.9 show the computational domain we use to simulate the XX-Es and the relevant geometry, respectively.

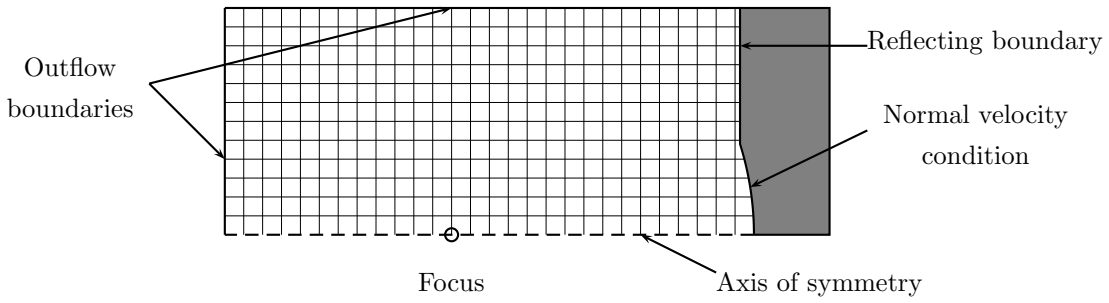

Figure 2.8: The computational domain used in this work to simulate the XX-Es lithotripter. A level set method was used to construct the reflecting boundary and the boundary with the normal velocity condition.

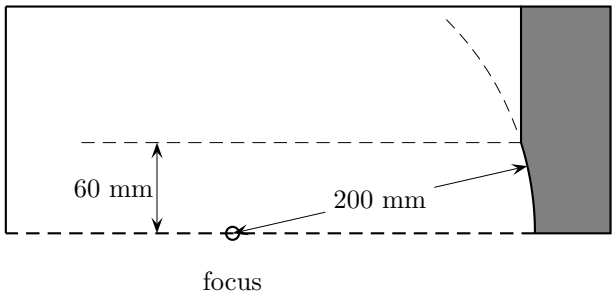

Figure 2.9: Geometry of the XX-Es lithotripter used in this work.

From a computational perspective, the treatment of the copper diaphragm motion is the same as the surface of the elements in the piezoelectric lithotripter array. We need to find a normal velocity $\dot{v}_n(t)$ for the copper diaphragm that generates the observed focal pressure waveforms. Unfortunately we could not find measured values of the displacement or velocity of the diaphragm as a function of time. Granz et al.[42] published displacement versus time curves for three different coil configurations in a different electromagnetic lithotripter, the LITHOSTAR Modularis by Siemens. This data is shown in figure 2.10.

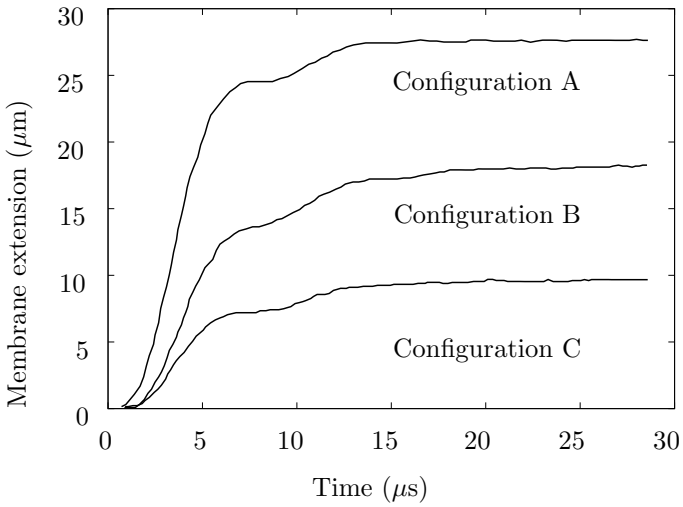

Figure 2.10: Membrane extension versus time for the coil of the LITHOSTAR Modularis electromagnetic lithotripter by Siemens.

We used this data as motivation to construct an estimate for the displacement versus time curve for the copper diaphragm in the XX-Es. Inspection of the data in figure 2.10 led us to believe a sigmoid function could reproduce the important features of the boundary motion. After experimenting with the hyperbolic tangent and error functions and finding unsatisfactory results, we discovered the Gompertz function, which has the form,

$$f(t) = ae^{be^{ct}}, \tag{2.20}$$

where $f(t)$ is the displacement of the diaphragm as a function of time, e is the base of the natural logarithm, a is the upper asymptote of the displacement curve, $c < 0$ is the growth rate, and $b < 0$ is an arbitrary parameter. Gompertz introduced this model in 1825 in his study of demographics [39]. Laird used this model to study the dynamics of tumor growth[55], and Zweitering et al. used it to model bacteria growth[89].

We in fact used a sum of two Gompertz functions as the displacement versus time curve in our simulations. One motivation for this decision is two displacement events can be seen in figure 2.10, roughly around 2 and 7 μs. Another motivation is the fact that the temporal pressure waveform at the focus has two compression and rarefaction events, meaning the diaphragm experienced two instances of

rapid movement from its equilibrium position. The specific displacement curve $f(t)$ we used to calculate our normal velocity boundary condition $v(t) = df(t)/dt$ was

$$f(t) = a_1 e^{b_1 e^{c_1 (t-t_1)}} + a_2 e^{b_2 e^{c_2 (t-t_2)}}, \tag{2.21}$$

where $a_1 = 12.572$ μm, $a_2 = 5.437$ μm, $b_1 = b_2 = -1$, $c_1 = c_2 = 6 \times 10^5$ s^{-1}, $t_1 = 13.33$ μs, and $t_2 = 20.50$ μs. In chapter 3 we will show the comparison of our simulated focal pressure waveform using this boundary condition with the measured waveform. Figure 2.11 shows a comparison of the diaphragm displacement curve for our model (time shifted to the left by 3 μs) with that for the LITHOSTAR Modularis configuration B, as shown in figure 2.10. It is important to note that we are not attempting to replicate the displacement curve for the LITHOSTAR Modularis. We used this data to motivate our attempts to capture the relevant, and unknown to us, dynamics of the XX-Es diaphragm. The purpose of the comparison is to demonstrate that our estimate for the boundary motion is reasonable given what is known about another electromagnetic lithotripter, i.e., the LITHOSTAR Modularis.

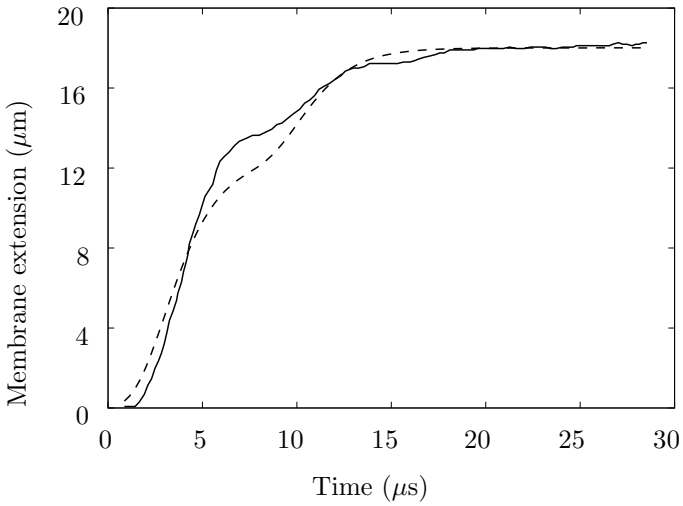

Figure 2.11: Diaphragm displacement curve for our model (dashed line) compared with that for the LITHOSTAR Modularis configuration B (solid line).

Chapter 3

Simulation of *In Vitro* Shock Wave Lithotripsy

3.1 Overview

Most SWL simulation efforts are of *in vitro* treatments. These treatments often provide the most reproducible environments in which to isolate and study the various dynamics occurring as a result of shock wave generation and propagation. The reader should refer to chapter 2 for references on previous work in SWL simulation. In this work, we simulate the dynamics of three types of lithotripters: electrohydraulic (Dornier HM3), piezoelectric (piezoelectric lithotripter array), and electromagnetic (XX-Es). In this chapter, we describe the dynamics of each of these lithotripters in a water bath, a setting designed to mimic *in vitro* conditions. In chapters 4 and 5 we discuss the ramifications these dynamics may have during an *in vivo*-like treatment.

3.2 Dornier HM3

As explained in chapter 2, current is passed through a pair of electrodes submerged in water and positioned at the first focal point of a hemiellipsoidal reflector. The water in the electrode gap is vaporized, creating a spherically diverging shock wave that reflects from the reflector and focuses at the second geometrical focus.

One of the first observations made about the focusing shock front in the context of the Dornier HM3 is the nonuniform strength of the focusing shock. Because of spherical spreading, the strength of the direct wave decays as $1/r$ as it travels farther from F1. As a result, the portion of the shock

front traveling along the axis is strongest, because this portion travels the shortest distance from the generation event at F1 to the reflector surface. Conversely, the portion of the shock front that reflects from the surface nearest the truncation plane of the reflector is weakest. As the direct wave diffracts past the truncated edge of the reflector, an edge wave is formed. The genesis of the edge wave is shown in figure 3.1.

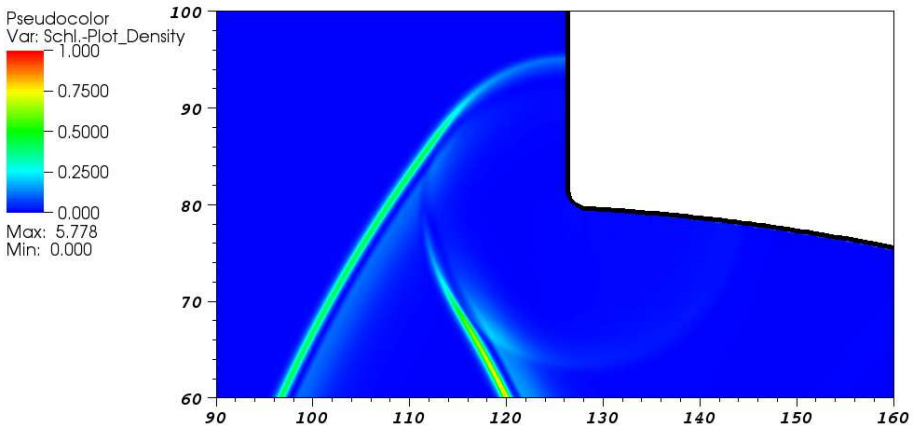

Figure 3.1: Flooded schlieren contour plot showing the generation of the edge wave as the direct and reflected shock fronts pass the truncated edge of the reflector. Axis labels indicate distance from focus in millimeters.

An additional waveform feature is seen for the lithotripsy pulse that is not observed in the case of a planar shock reflecting from a concave wall. The added rarefaction in the incident lithotripter pulse, following the leading shock, produces an additional compressive front after reflection that evolves during the focusing process, much as the diffraction shock evolves as described by Sturtevant and Kulkarny. As a result, a fourth front is seen in addition to the expected three shock intersection near the focus. Flooded schlieren contours showing the various shock fronts in the focal region are shown in figure 3.2. The bottom contour plot in figure 3.2 shows the hallmark of weak shock focusing, a crossed and folded wavefront. Sturtevant and Kulkarny also observe this feature in their work and discuss it in detail.

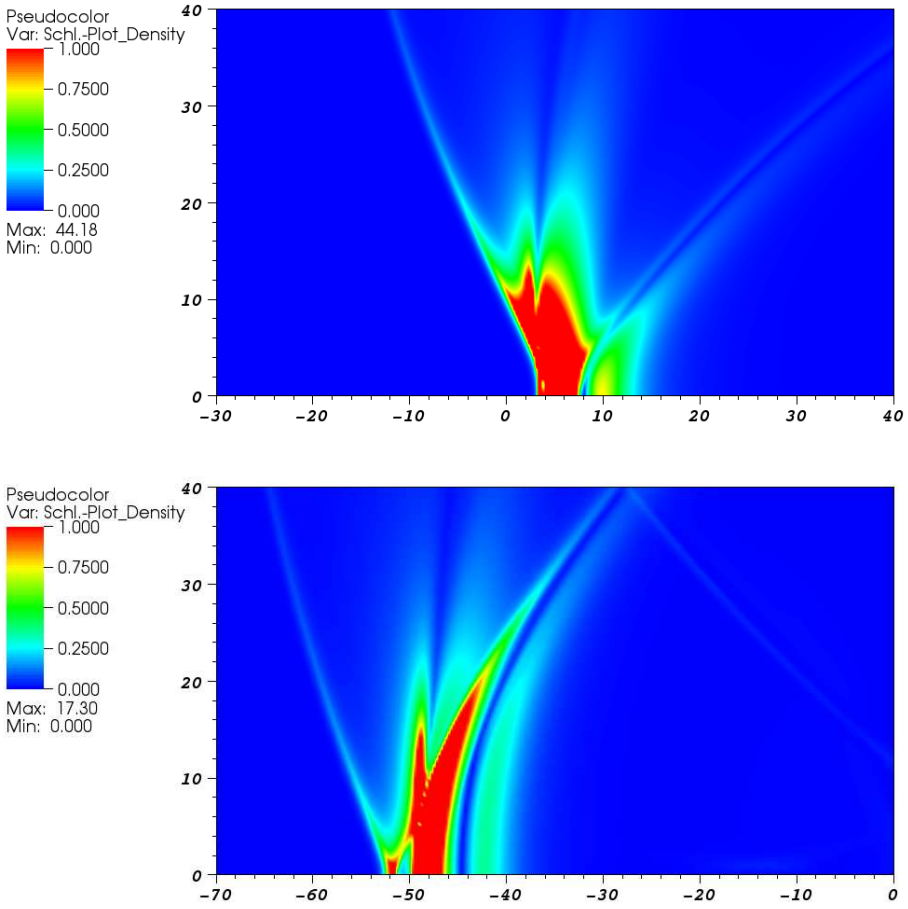

Figure 3.2: Flooded schlieren contour plots of focusing shock front as it approaches the focus (top) and as it passes beyond the focus (bottom). Axis labels indicate distance from focus in millimeters.

Figure 3.3 shows our computed pressure versus time for three points: the focus (F2), 5 mm prefocus, and 5 mm postfocus. Prefocal locations are between the electrode gap (F1) and F2; postfocal locations are beyond F2 when looking from F1. The data for the nonfocal points have been time shifted such that the shock fronts arrive concurrently for all three locations.

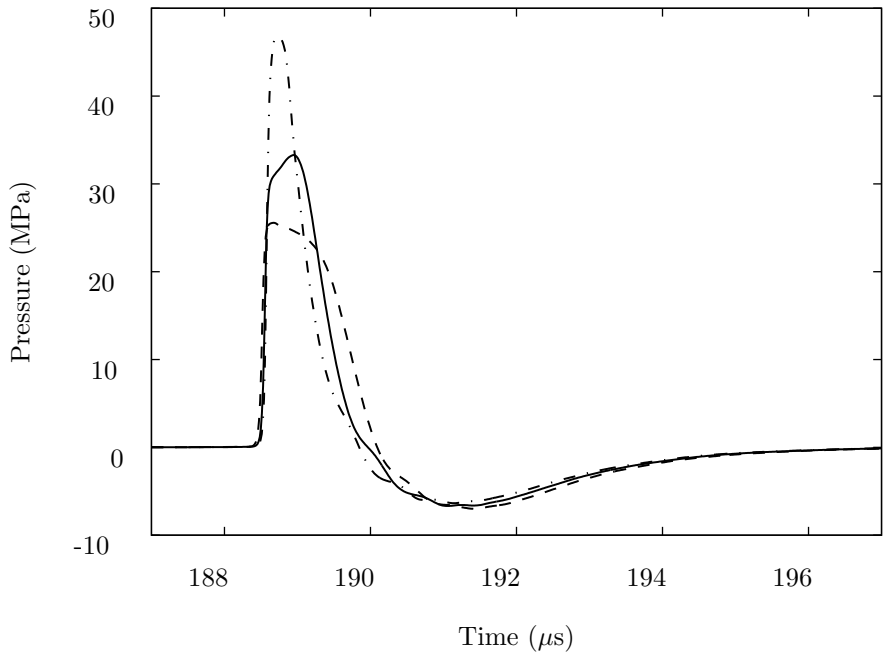

Figure 3.3: Pressure versus time waveforms at F2 and at 5 mm pre- and postfocal locations. Focus (———); 5 mm prefocal (– – –); 5 mm postfocal (–·–·–).

The waveform structure varies considerably in the 10 mm axial window surrounding F2. Computed peak positive pressures increase from 25 to 45 MPa. The shock front is followed by an expansion in the pre- and postfocal cases whereas at F2 itself a secondary pressure increase follows the arrival of the shock. The width of the positive pressure region decreases slightly as the wave propagates downstream. The width of the negative pressure region and the negative pressure amplitudes are essentially uniform through this segment of the axis.

The appearance of the shock tip at F2 is not expected given available experimental measurements. A similar effect has been shown, however, in a previous simulation[49]. Figure 3.4 shows a comparison of the computed results of this study and those of Iloreta et al.[49], where the effect was attributed to insufficient grid resolution. In our case, we find this secondary pressure increased after the arrival of the initial shock front to be grid independent beyond a sufficient level of resolution.

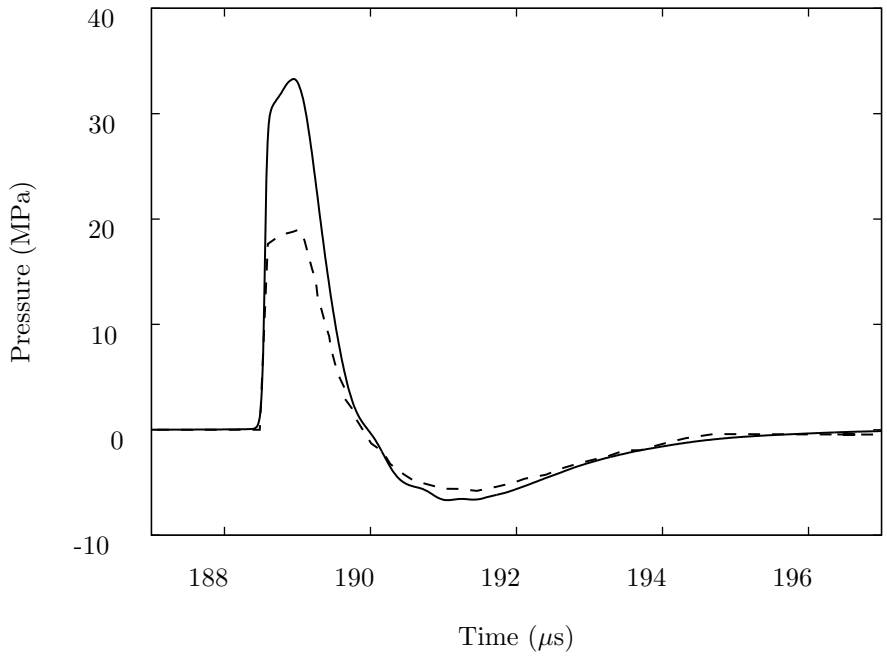

Figure 3.4: Pressure versus time at F2. Computed results of this study (———) versus those of Iloreta et al. [49] (– – –).

Several facets of the simulation could possibly explain this subsequent pressure increase after the arrival of the shock in the focal waveform. First, we use an axisymmetric geometry, and as such we generate shocks that focus in a stronger fashion than those observed in experiments. The ratio of the strength of the focusing shock front on the axis relative to the strength away from the axis is greater for our simulations than would be the case in experiments. The portion of the focusing shock front along the axis then races ahead of the off-axis portion, and the difference in arrival times at F2 is manifested as the further rise in pressure after the arrival of the shock front. One violation of the assumption of axisymmetry in experiments is found with the support structure for the electrodes. The spark gap is typically positioned at F1 obliquely relative to the axis. The cage surrounding the electrode gap disrupts the initial propagation of the spherically diverging shock, and the resulting diffraction events perturb the focusing in ways not found in our simulation. Second, we do not model the gas phase present at F1 after the initial vaporization event. In experiments, the spherically diverging shock reflects from the reflector, and a portion of the front travels back through the vapor cloud. In our simulation, we only have a single phase and ignore the mismatch of acoustic impedances around F1. Both of these

effects perturb the focusing process, particularly near the axis, potentially to a sufficient degree that experimental measurements would not show the waveform structure we compute at F2.

Even though the appearance of the focal shock tip does not match expectations given observed pressure measurements, our code does produce sharply focused shocks around 5 mm postfocus and beyond. This result is consistent with the explanation for the appearance of the focal waveform that the portion of the shock front traveling along the axis races ahead of the front farther from the axis. These fronts would then arrive simultaneously slightly beyond the focus, where even though the shock along the axis is traveling slightly faster it must also travel farther to reach postfocal locations as a result of the ellipsoidal geometry of the reflector. Figure 3.5 shows computed pressure waveforms at 5, 15, and 25 mm postfocus.

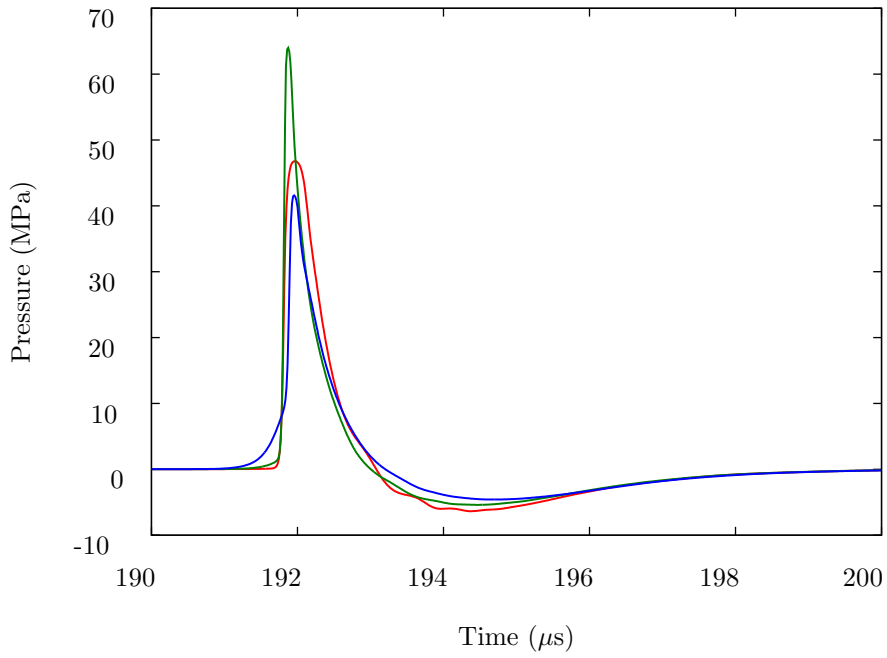

Figure 3.5: Pressure versus time at various postfocal locations. 5 mm postfocus (red); 15 mm postfocus (green); 25 mm postfocus (blue).

Peak positive pressures around 65 MPa occur approximately 15 mm postfocally. Negative pressure amplitudes decrease slowly as the pulse propagates beyond the focus. The width of the positive pressure region increases as the edge wave has now inverted, i.e., is a compression, and races ahead of the rest of the pulse, as has been predicted in the linear theory[45] and observed experimentally[24]. This effect

is clearly seen in the 25 mm postfocal waveform shown in figure 3.5.

3.3 Piezoelectric Lithotripter Array

As discussed in chapter 2, we use the measured pressures generated from the actuation of a single piezoelectric element to compute an estimate for the displacement profile of that element. We then use this estimated profile for all the elements in our simulation. Because of our use of axisymmetric geometries, the only single element we model is the one whose center lies on the axis of the lithotripter, i.e., the element numbered 1 in figure 2.4. We then model seven additional rings of elements without accounting for the interelement spacing within each ring. We do, however, correctly account for the spacing between the rings of elements.

Figure 3.6 shows flooded schlieren contours of the piezoelectric lithotripter array approximately 20 μs after all the elements are fired. Several important features of the behavior of the individual elements can be seen. Three primary fronts are seen for each ring of elements that has been fired. These multiple fronts are the result of the ringing of the elements, i.e., when current is discharged through the elements, the initial motion is away from the bowl, but then the elements retreat toward their equilibrium position, overshoot this position, and again move away from the bowl. This oscillatory behavior produces multiple fronts that each focus and are clearly seen in the focal waveforms. Like the case for the Dornier HM3, diffraction waves are formed as the fronts diffract into quiescent fluid. For the Dornier HM3, this effect was observed when the direct and reflected fronts diffracted past the truncated edge of the reflector. For the piezoelectric lithotripter array, the same effect happens when the fronts diffract past the edges of the individual elements. In fact, our simulation produces fewer diffraction waves than would be observed experimentally, because the axisymmetric geometry prevents us from capturing the diffraction events that would take place between the various elements in a single ring.

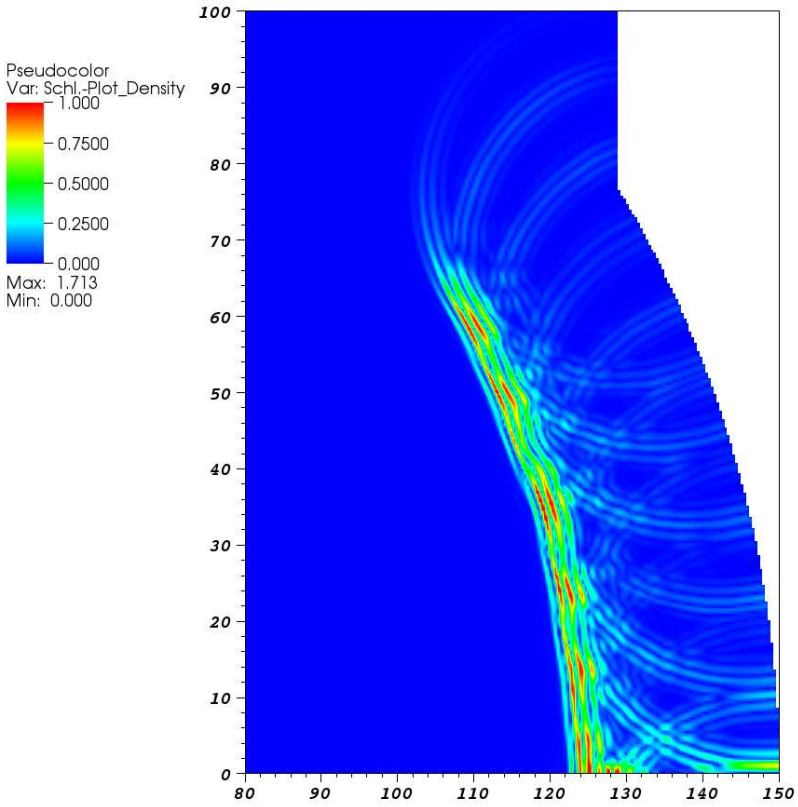

Figure 3.6: Flooded schlieren contours for piezoelectric lithotripter array approximately 20 μs after firing. Axis labels show distance from the focus in millimeters.

Figure 3.7 shows a comparison of the computed focal pressure waveform versus experimental measurements. The peak positive and negative pressure amplitudes and the pulse widths for the compressions and rarefactions agree well with the measured values. The second shock front arrives approximately one-tenth of a microsecond sooner in our case than seen in the measured data. We compute the third compression event to occur about half a microsecond ahead of where it is seen experimentally. As in the case of the XX-Es lithotripter, these small discrepancies will not effect the observations we make about the focal region dynamics. We believe these small discrepancies between the computed results and the experimental measurements to largely be the result of our inability to reproduce the temporal jitter in interelement firings found in experiments.

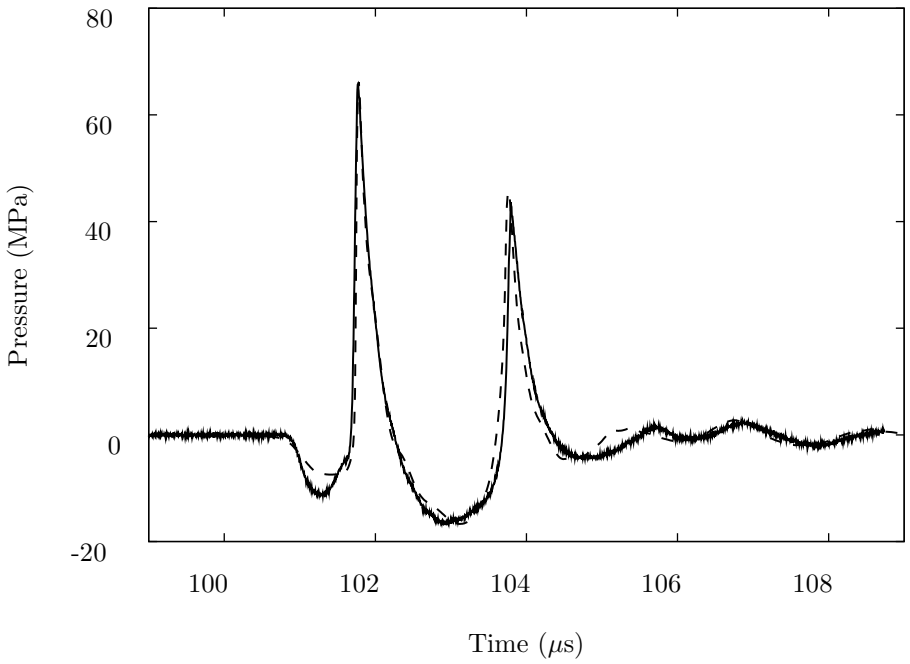

Figure 3.7: Pressure versus time at the focus for the piezoelectric lithotripter array. Experimental measurements (———); computed results (– – –).

We generated the displacement profile for the piezoelectric elements by using the measured values for the firing of a single element and computing the surface velocities using the Rayleigh integral, as was discussed in chapter 2. In that case, we did not have to consider interelement delays. For the computed waveform shown in figure 3.7, we had to introduce delays between the firing of different rings of elements to better match the measured data. Figure 3.8 shows a comparison of our computed waveforms when we fire the rings synchronously versus when we introduce a delay to account for the temporal jitter in the firing of different elements. Table 3.1 shows the relative delay in firing of each ring of elements, where the firing of the third ring (ring 3) occurs first and is thus taken as having zero delay. The rings of elements are identified in figure 2.4. Ring 3 consists of elements 8 through 19.

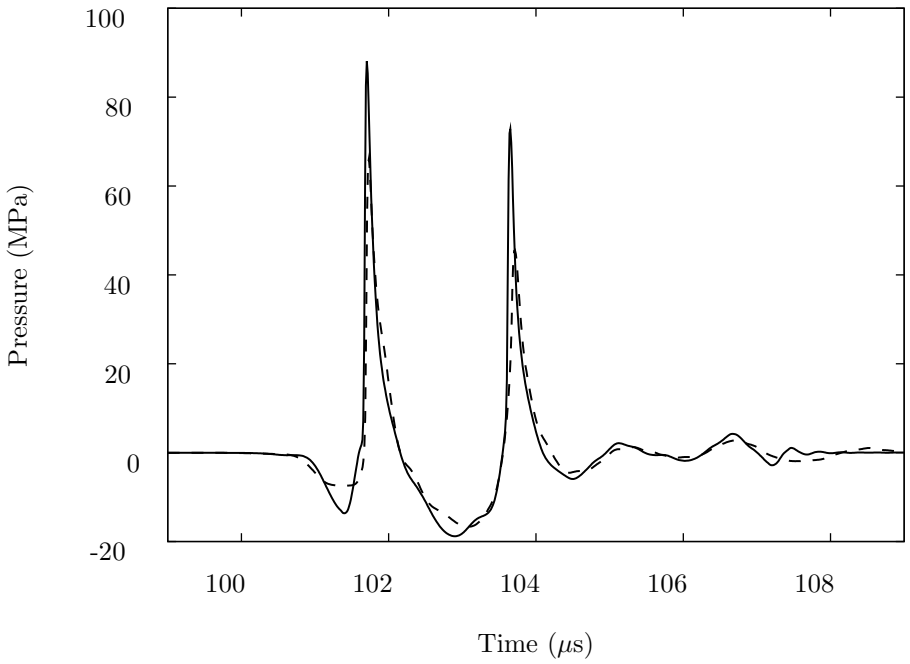

Figure 3.8: Computed pressure versus time at the focus for the piezoelectric lithotripter array. All elements fired synchronously (———); elements fired with delays of hundreds of nanoseconds (– – –).

Table 3.1: Temporal delay in firing of each ring of elements for the piezoelectric lithotripter array relative to the firing of the third ring of elements (ring 3), ring 1 is the center element.

Ring number	Firing delay (ns)
1	424.6
2	125.4
3	0.0
4	204.6
5	495.0
6	19.8
7	217.8
8	422.4

The waveforms in figure 3.8 were time shifted to align the first shock fronts. Because the delay case has smaller amplitudes, the fronts travel slower and arrive at the focus later than the fronts in

the synchronous case. In the experimental arrangement, the maximum interelement temporal jitter was measured to be less than 50 ns. In our case, we had to introduce delays in the relative firing of different rings as large as 500 ns. The primary reason such large delays were required was the fact that we must simulate the firing of all elements in a given ring at exactly the same time due to the axisymmetric geometry. The outermost ring consists of 42 elements, nearly one fourth of the elements in the piezoelectric lithotripter array. We need delays in the relative firing of different rings larger than 50 ns to account for the fact that we must fire such a large portion of the elements in a truly synchronous fashion. As shown in figure 3.8, the delays required to match the measured data suppress the peak positive pressures at the focus by over 20 MPa and consequently have a nontrivial effect on the various flow quantities in the focal region.

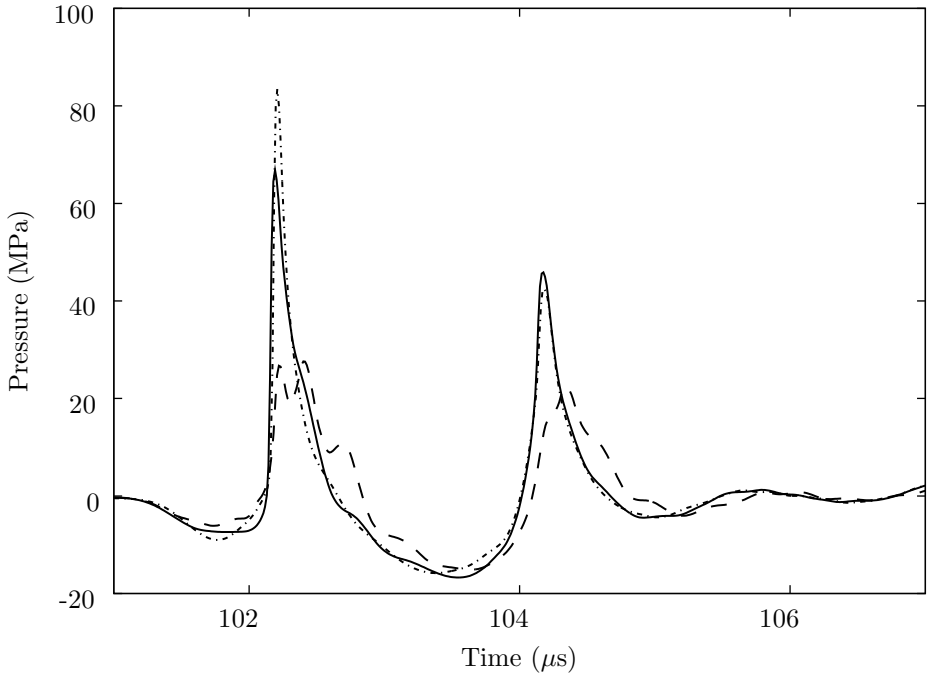

Figure 3.9: Computed pressure versus time at the focus and locations 5 mm pre- and postfocus for the piezoelectric lithotripter array: focus (———), 5 mm prefocus (– – –), 5 mm postfocus (–·–·–).

3.4 XX-Es

As explained in chapter 2, electrical current is discharged through a coil, which causes an attached truncated spherical diaphragm to displace from its rest position and create a self-focusing nonlinear pulse.

The pulse front forms a shock on its way to the focus. Using the previously described approximation for the diaphragm motion, we simulate this waveform creation event, and figure 3.10 shows a comparison of our computed focal waveform and the measured waveform published in the work of Eisenmenger et al.[32].

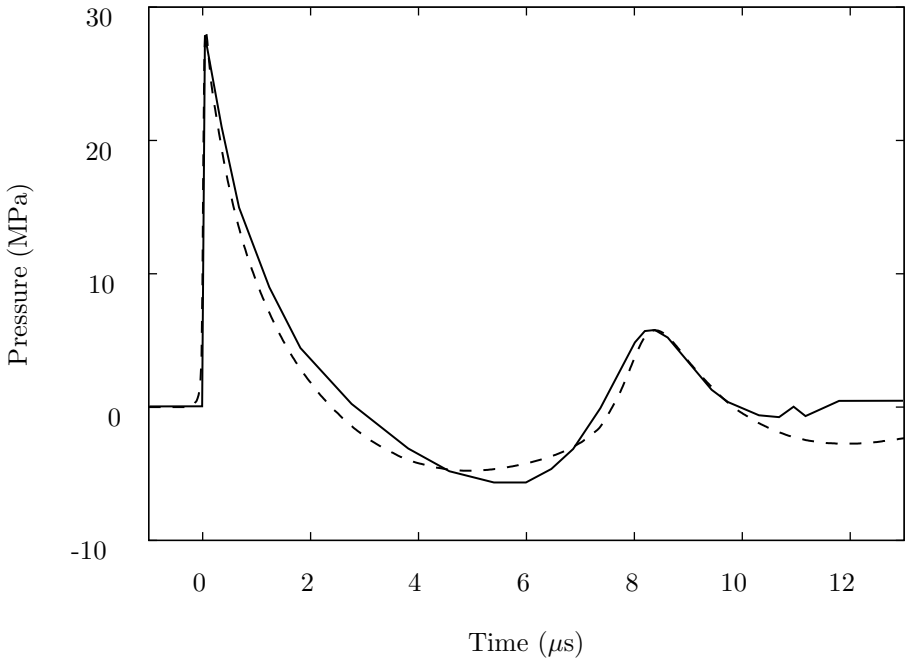

Figure 3.10: Pressure versus time at the focus for the XX-Es. Experimental measurements (———); computed results (– – –).

The disagreements between the computed and focal waveforms are a result of our incomplete knowledge of the details of the diaphragm motion. We used the LITHOSTAR Modualris displacement data as motivation for our estimates for the XX-Es. We then adjusted the free parameters in the Gompertz model equations until our computed results agreed with the experimental measurements to a satisfactory degree. The peak positive amplitudes of the compression waves, observed at approximately 0 and 8 μs in figure 3.10, are in good agreement. The positive pressure pulse widths for both compressions are slightly narrower than the measured values, by a few tenths of a microsecond. The calculated peak negative pressure amplitude for the first rarefaction is slightly weaker than the measured value, while for the second rarefaction the computed values are stronger.

The Gompertz functions we use as model equations for the displacement profile of the spherically

shaped diaphragm clearly do not produce ideal agreement between the computed and measured data. However, for the purposes of our study, the agreement is sufficient to investigate the dynamics of interest. The observations we make are insensitive to the small discrepancies between the computed and measured waveforms. Using measurements of the diaphragm motion as source conditions in these calculations would remove most of the observed discrepancies. Given the data to which we have access at this time, we are satisfied with the results of our simulation given the physics in which we have an interest.

The waveforms measured at the focus and at 5 mm pre- and postfocal locations appear nearly identical as a result of the wide focus of the lithotripter. Figure 3.11 shows waveforms measured at the focus and at 25 mm pre- and postfocal locations. The waveform at 25 mm prefocus has not yet formed a shock front. Additionally, the diffraction waves following the lead compression have not yet caught up with the front, and as a result the negative pressures are lower in the prefocal region than at the focus itself. This phenomenon was also seen with the HM3 and has been studied experimentally[74]. The inverted edge wave is beginning to move ahead of the shock front in the postfocal waveform, which in part accounts for the reduced peak positive pressure compared with the focal waveform. The peak negative pressures become less negative as the wave propagates downstream.

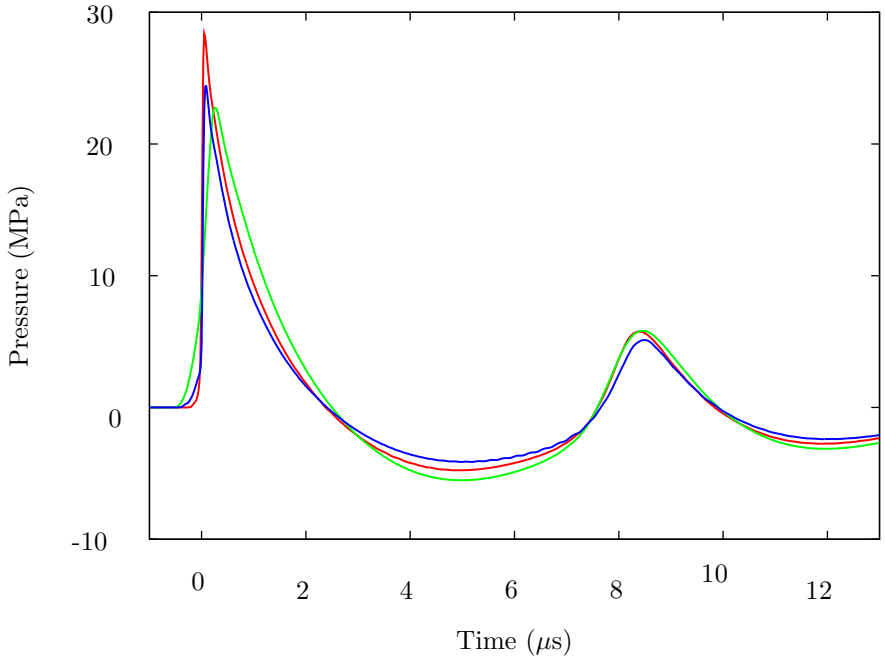

Figure 3.11: Pressure versus time waveforms at F2 and at 25 mm pre- and postfocal locations. Focus (red); 25 mm prefocal (green); 25 mm postfocal (blue).

3.5 Summary

In this chapter, we discussed the fundamental characteristics of shock generation, propagation, and focusing in a pure water bath, a model for the *in vitro* environment in which most lithotripsy experiments are performed. The details of the shock generation mechanism for each lithotripter were provided. We showed the ability of our numerical method to capture the sharp shock fronts expected at the focus of a shock wave lithotripter. Finally, we presented a comparison with experimental data for each lithotripter and explained why differences are seen between this data and our computed results. With this foundation established, we are now ready to discuss the various effects observed as a result of the introduction of heterogeneous materials into the focal region of each lithotripter.

Chapter 4

Simulation of *In Vivo* Shock Wave Lithotripsy

4.1 Overview

In chapter 3 we discussed the water bath wave propagation characteristics of three classes of shock wave lithotripters: electrohydraulic (Dornier HM3), piezoelectric (piezoelectric lithotripter array), and electromagnetic (XX-Es). In this chapter, we will investigate the change in the dynamics resulting from the presence of materials with densities and/or sound speeds differing from those of the waterlike medium in which the shock waves are generated. The motivation for introducing new materials to our domain is to mimic the effect of soft tissue on the wave propagation during an *in vivo* treatment.

The effects of high intensity sound on tissue have been studied at least as far back as 1927[83]. Researchers then sought a more complete understanding of the acoustic properties of tissue, and in 1950, the specific gravity and sound speed of living human tissue were measured as 1.06 and 1540 m/s, respectively[61]. In the context of shock wave lithotripsy, the presence of soft tissue in the shock path has been shown to have a nonnegligible effect on focal pressure waveforms. *In vivo* measurements in pigs have shown waveforms of similar appearance to the *in vitro* case but with suppressed amplitudes[19]. *In vitro* experiments have shown that when layers of soft tissue, nominally the same thickness as seen by a shock wave traveling through the body, are placed upstream of the focus, the waveform amplitudes are attenuated and additional peaks are introduced[48]. In this chapter, we will study the changes in focal region dynamics that occur as a result of the introduction of tissuelike materials that mimic in isolation the body cavity and the kidney itself, and finally the effect of the two together.

As we discussed in chapter 2, one of the conservation equations we integrate is for the total energy per unit volume,

$$\rho e_t = \rho e + \frac{1}{2}\rho\left(u^2 + v^2\right), \tag{4.1}$$

where ρe is the internal energy per unit volume. Taking advantage of the stiffened gas equation of state, we have

$$\rho e = \frac{p + \gamma p_\infty}{\gamma - 1}. \tag{4.2}$$

The terms γ and p_∞ are set for each material in our simulation. For water, we use $\gamma = 5.5$ and $p_\infty = 4036$ atm. We are free to choose different values to model the properties of soft tissue. The infinitesimal sound speed of the medium, c, is given by

$$c^2 = \gamma\frac{p_0 + p_\infty}{\rho_0}, \tag{4.3}$$

where p_0 and ρ_0 are the atmospheric pressure and density, respectively. The results of our simulation are sensitive to the sound speed of the medium, but in general are largely insensitive to the specific choice of γ and p_∞. In addition to changing one or both of these parameters, we can also change the atmospheric density of a material. In this sense, we can introduce contrasts in acoustic impedance by changing the sound speed and/or the atmospheric density, and introducing these contrasts will allow us to investigate how the focal region acoustics will change with the presence of soft tissuelike materials.

4.2 Scattering and Absorption

Scattering and absorption are the dominant processes by which propagation through soft tissue changes wave amplitudes and waveform geometries[63]. Scattering, in whose definition we also include effects like internal reflection, occurs at interfaces of mismatching acoustic impedances, which requires a heterogeneous medium. Absorption is the conversion of acoustic energy into thermal energy and is observed in both homogeneous and heterogeneous materials. We model the scattering effect by changing the

density and sound speed of the tissue, as described in the previous section. In our numerical framework as currently described, however, we have no capacity to model thermoviscous absorption, or indeed absorption of any variety. Measurements show, though, a frequency-dependent absorption of ultrasound in various soft tissues. Carstensen et al. published frequency-dependent absorption data for blood in 1953[12]. In 1956, Goldman and Heuter published a collection of human tissue absorption values from various researchers, and these values were mostly found in the range of 0.5 to 2 dB/cm/MHz[38]. Dunn et al. published a muscle absorption of 0.13 dB/cm and a fat absorption of 0.05 dB/cm, both at 1 MHz[31]. They also noted that these absorption values were proportional to frequency. Goss et al. twice published compilations of the available experimental data measuring absorption in various soft tissues[40, 41]. We would like to find a way to model the effect of absorption.

One difficulty with absorption is an absorption law is usually provided in the frequency domain, i.e., $\alpha = \alpha(f)$, where $\alpha(f)$ is the absorption in the material for a signal of frequency f. We integrate the conservation laws in our code, however, in the time domain. Yang and Cleveland overcame this problem by using a modified form of the KZK equation to simulate the propagation of nonlinear acoustic beams through a tissuelike material[84]. The frequency-dependent absorption was approximated via the use of two relaxation processes. Details can be found in the cited reference. The density and sound speed of their tissuelike material were $\rho = 1050$ kg/m^3 and $c_0 = 1540$ m/s, respectively, and the power law used to model the absorption in tissue was

$$\alpha(f) = \alpha_0 \left(\frac{f}{f_0} \right)^{\eta}, \tag{4.4}$$

where $\alpha_0 = 3.4538$ Np/m, $\eta = 1.1$, and $f_0 = 1$ MHz. The absorption is then 0.3 dB/cm at 1 MHz for this case. Following the lead of Yang and Cleveland, we modified our own code to include the same relaxation processes. The details of the various necessary numerical manipulations can be found in Appendix A.

Figure 4.1 shows calculated pressure versus time for a simulation where we specify a higher density and sound speed in a circular region around the focus to mimic the presence of the body cavity of a patient. This model is described more thoroughly in the following section. Figure 4.1 shows results from simulations with and without the use of absorption. We chose the simple body cavity model for

this purpose because the effect of absorption is isolated, i.e., scattering plays a negligible role since only one acoustic impedance interface with a very simple geometry exists. These results show that absorption alone leads to a decrease in focal wave amplitudes of less than 10%, and the only dispersive effect is to increase the rise time of the focal shock. We will see later that the effects of scattering from multiple acoustic impedance interfaces are much stronger than this effect of absorption. While the effect of absorption is nontrivial, we disabled this feature for the simulations whose results we discuss for the remainder of this document for purposes of improving computational efficiency. The effect of absorption on all of our results is simply to diminish amplitudes by 5% to 10% without any appreciable change in the waveform geometries.

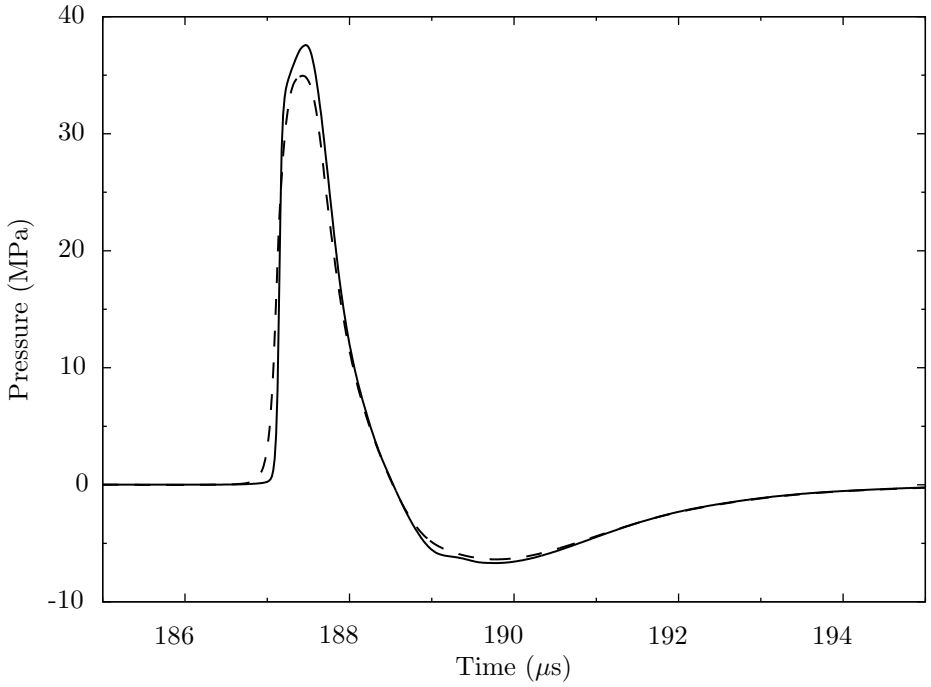

Figure 4.1: Pressure versus time for the Dornier HM3 simulation using a simple model of a body cavity, without absorption (———) and with absorption (– – –).

4.3 Heterogeneous Materials

Figure 4.2: Color image of a sample slide from the Visible Human Project made available by the VOXEL-MAN Group[1]. The arrow points in the direction of an approximate blast path for treatment of the left kidney (on the right side of the image; in this orientation the patient is facing the bottom of the page).

We have constructed three different computational domains to study shock scattering from material interfaces in shock wave lithotripsy. In the first case, we use a circular region to model the cross section of the human body. We arbitrarily chose a radius of 15 cm for this region, and the center of the model body cavity was positioned such that the shock must travel through 6 cm of tissue along the axis before reaching the focus, which matches values used by other researchers[22, 4]. The initial density of the body cavity was chosen to be 1025 kg/m^3 and a value of $\gamma = 6.06$ was used to give a small signal sound speed of 1555 m/s. These values are reasonable given the available experimental data on the acoustic properties of various soft tissues. Our purpose here is to study the dominant effects material interfaces have on shock propagation. We are most interested in how material interfaces perturb the acoustic relative to the water bath environment. We leave for future work the study of how these results further change as a function of changing values of density and sound speed along the various interfaces.

In the second domain, we again use the previously described body cavity model, but now we add an arbitrarily created model of the kidney. Our motivation for creating this model was to mimic large scale anatomical features of the kidney. We are limited by a number of factors in this regard, with

the most significant limitation being the axisymmetric geometry. As a result of this restriction, we will necessarily be unable to model the kidney in an anatomically accurate fashion. However, we should be able to study some first order effects produced by the existence of a material interface of roughly the same size and shape as seen in the human body. For the model kidney, we chose an initial density of 1050 kg/m^3 and $\gamma = 6.37$, which produces a small signal sound speed of 1575 m/s.

In the third domain, we use digitized data from the Visible Human Project to establish initial conditions. The VOXEL-MAN Group at the University Medical Center Hamburg-Eppendorf has made sample data available, and one sample image is of the human midsection[1]. Using this segmented data, we were able to assign values of density and sound speed to different classes of soft tissue. To match our arbitrarily constructed models, the density of all tissue except kidney and fat was set to 1025 kg/m^3. The kidney tissue was given a density of 1050 kg/m^3, while fat was prescribed a density of 900 kg/m^3. The values for γ for the different tissue were allowed to change, to achieve particular sound speeds. All soft tissue was assumed *a priori* to have a sound speed of 1555 m/s. We then used the tissue classifications provided in the VOXEL-MAN Group data to make adjustments. Some tissue was specifically marked as unclassified, and we decreased the sound speed in this region to fall between general soft tissue and fat. The tissue classified as general is mostly muscle. The values used for the various tissue types are given in Table 4.1.

Table 4.1: Sound speeds assigned to different tissue types.

Tissue type	density (kg/m^3)	sound speed (m/s)	γ
water	1000	1500	5.5
unclassified	1025	1535	5.904
general	1025	1555	6.058
fat	900	1465	4.722
kidney	1050	1575	6.367

We do not make the claim that the values chosen are to be preferred over other reasonable values. The particular values we have selected are in general agreement with what is seen in the literature, and more importantly, because we are studying the first-order effects introduced by changes in acoustic

impedance, the specific values of density and sound speed should not affect the general observations we will make. We leave to future work an investigation of these effects in three dimensions and a more thorough study of the particular choices for acoustic properties.

Figures 4.3 and 4.4 show contour plots of the initial values for nondimensional density and γ, respectively, for the piezoelectric lithotripter array simulation. The density is nondimensionalized by the ambient density for water (1000 kg/m^3). As a result, the nondimensional density $\hat{\rho}$ for water is 1. The contour maps for the other lithotripter simulations look identical to those shown for the piezoelectric case.

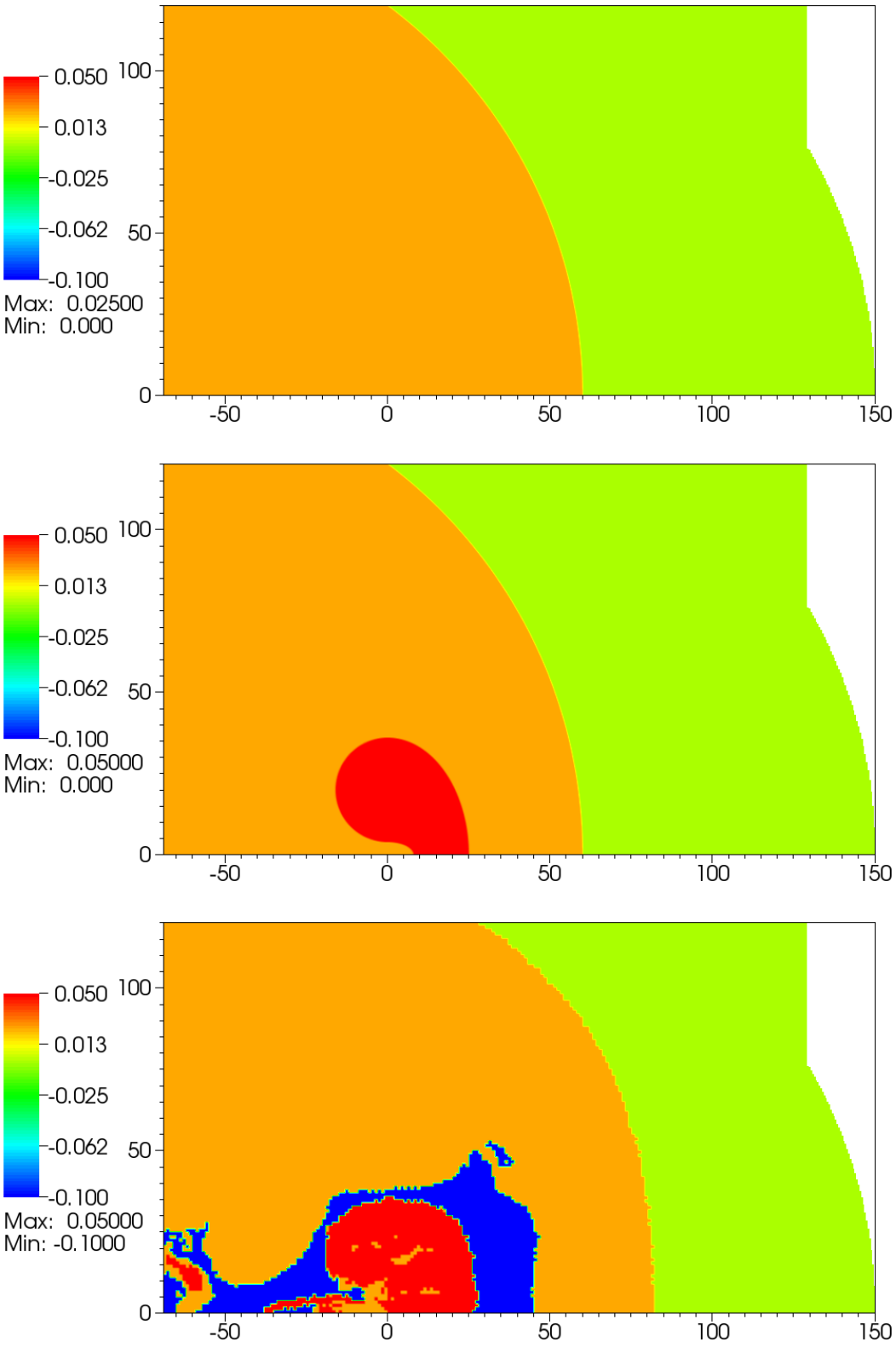

Figure 4.3: Flooded contours of nondimensional density at $t = 0$ for the piezoelectric lithotripter array simulation. Quantity plotted is $\hat{\rho} - 1$, where $\hat{\rho} = 1$ for water.

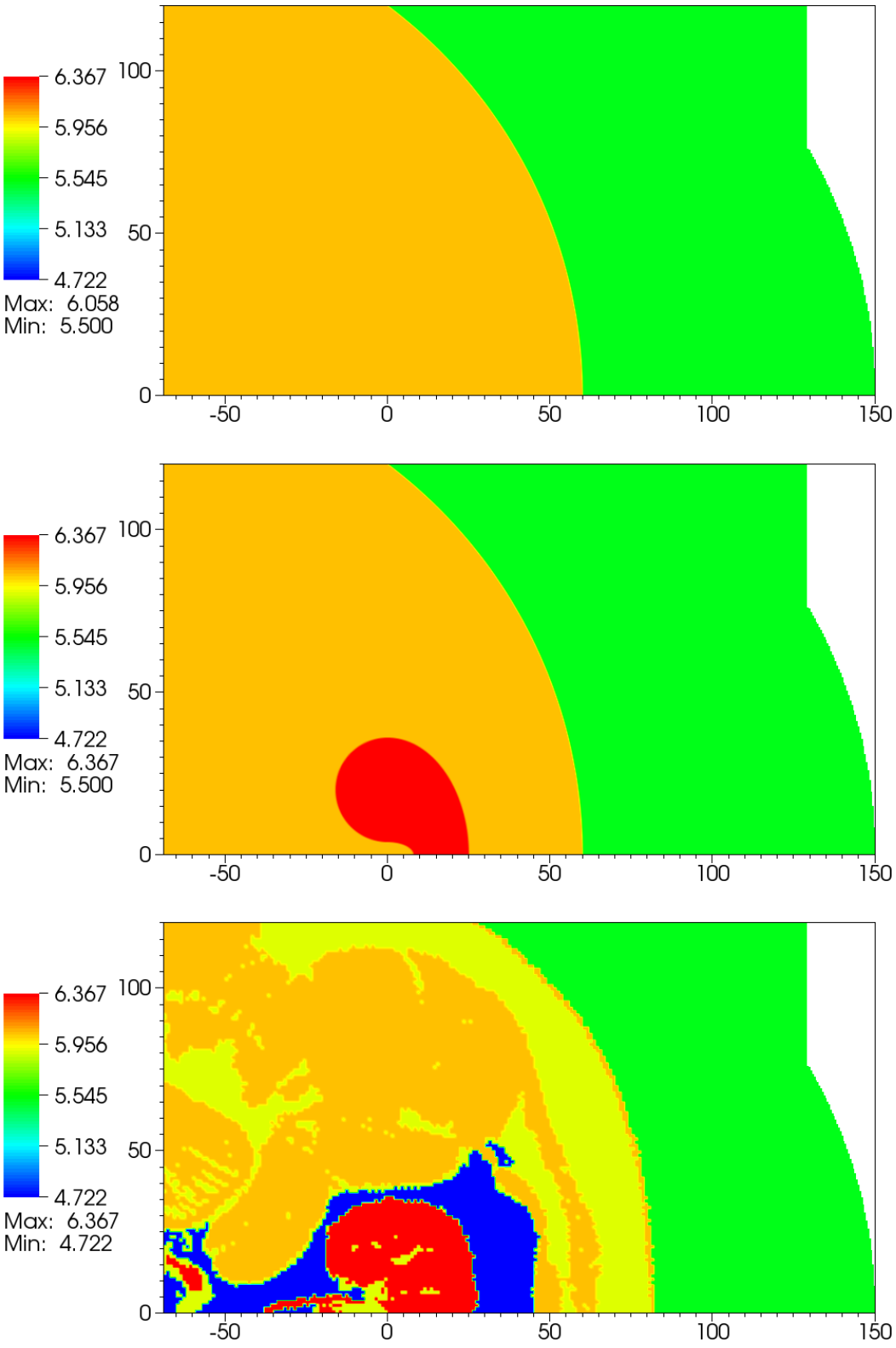

Figure 4.4: Flooded contours of γ at $t = 0$ for the piezoelectric lithotripter array simulation. For water, $\gamma = 5.5$.

For the Dornier HM3, the portion of the wavefront that first passes an acoustic impedance interface is the portion generated at the truncated edge of the reflector. Similarly, for the piezoelectric and electromagnetic lithotripters, the portion of the wavefront farthest from the axis first sees a change in acoustic impedance. The reason is the geometry of the domain. In the case of our arbitrarily constructed body cavity model, the body cavity has a circular cross section of 15 cm radius centered at a point on the axis 9 cm postfocus. Thus the portion of the wave traveling along the axis must traverse 6 cm of tissue before reaching the focus, which is roughly in agreement with what is observed in practice. If the body cavity was centered at the focus, all parts of the focusing wavefront would impinge on the interface simultaneously. However, because the curvature of the body cavity model is different than the curvature of the focusing wavefront, the portion of the wavefront farthest from the axis first sees a change in acoustic impedance.

4.4 Focal Region Waveforms

All waveforms have been time-shifted so the first focusing shock front is aligned in all cases. Arrival times are different in the different cases because of differences in the sound speed profiles encountered by the focusing wavefront on its approach to and through the focal region.

4.4.1 Dornier HM3

Because our body cavity model has a higher sound speed than the surrounding water, the far off-axis portion of the wavefront travels more quickly to the focus than it does in the water bath case. In Section 3.2, we discussed the appearance of the shock tip at the focus for the Dornier HM3 lithotripter. The initial shock wave was followed by a secondary, continuous pressure increase that was then followed by the expected expansion. We posited that the reason we observe this secondary pressure increase numerically is because the portion of the focusing wavefront along the axis arrives at the focus before the portion farther off-axis, as a result of nonlinear effects. Now that the path to the focus for the off-axis portion of the wavefront takes it through more soft tissue than the near-axis portion, the wavefronts arrive at the focus with a smaller relative delay. Figure 4.5 shows pressure versus time calculated at the focus for four cases: the water bath, with the model body cavity, with the model body cavity and

kidney, and with the VOXEL-MAN Group data.

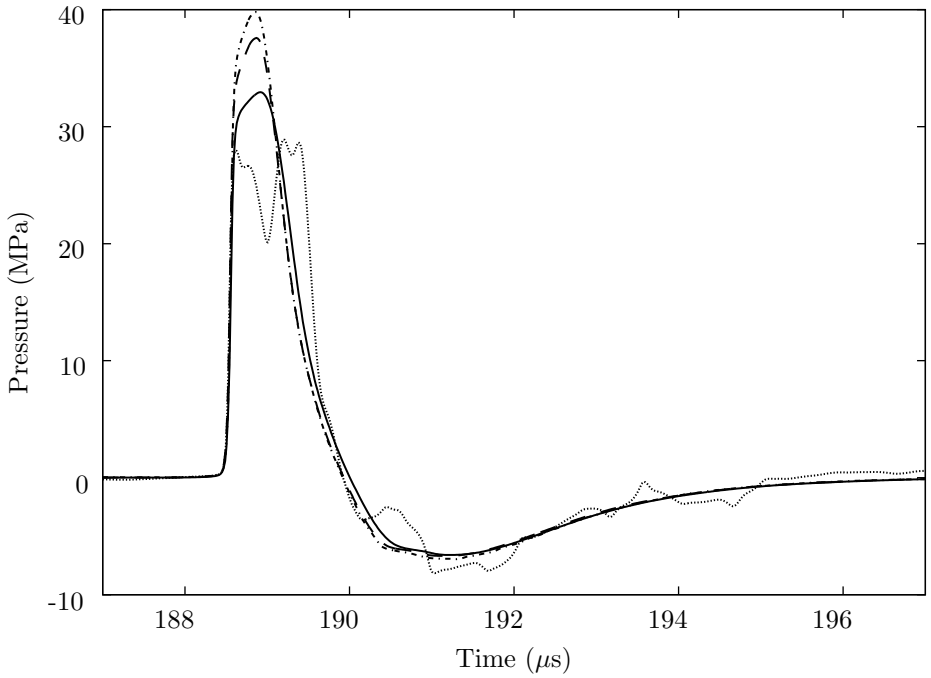

Figure 4.5: Pressure versus time at the focus for the Dornier HM3: water bath (———), body cavity (– – –), body cavity and kidney (–·–·–), VOXEL-MAN Group data (·····).

The peak focal pressures increase for the cases with the model body cavity and kidney relative to the water bath case. This effect is expected as the off-axis portion of the focusing wavefront now more closely follows the arrival of the near-axis portion. In the linear case, the entire focusing wavefront would arrive simultaneously, and the focus would produce the largest pressures observed in the domain (indeed they would be singular). With nonlinear and diffraction effects, the focus does not produce the largest observed pressures. As the delay in arrival between the off-axis and near-axis portions of the wavefront decreases, peak focal pressures rise, and the actual focal waveform geometry better agrees with expectations.

Figures 4.6 and 4.7 show pressure versus time at two different points along the axis, 5 mm prefocus and 5 mm postfocus, respectively. These two waveforms show the same trends as the focal waveform. Peak positive pressures increase, positive pulse widths decrease, and peak negative pressures remain largely unchanged. All of these effects can be explained by the decrease in delay of the arrival of the various portions of the focusing shockfront. Figure 4.8 shows pressure versus time in the focal plane at

a point 5 mm off-axis. This plot shows the same effects are observed in a neighborhood surrounding the focus, both on- and off-axis.

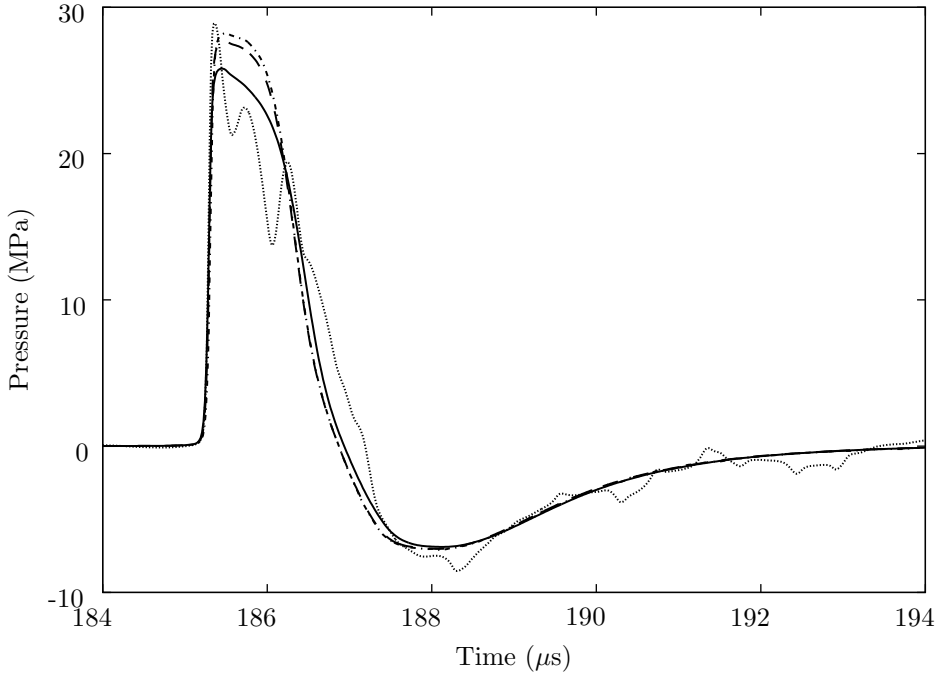

Figure 4.6: Pressure versus time at a point on the axis 5 mm prefocus for the Dornier HM3: water bath (———), with body cavity (– – –), with body cavity and kidney (–·–·–), VOXEL-MAN Group data (·····).

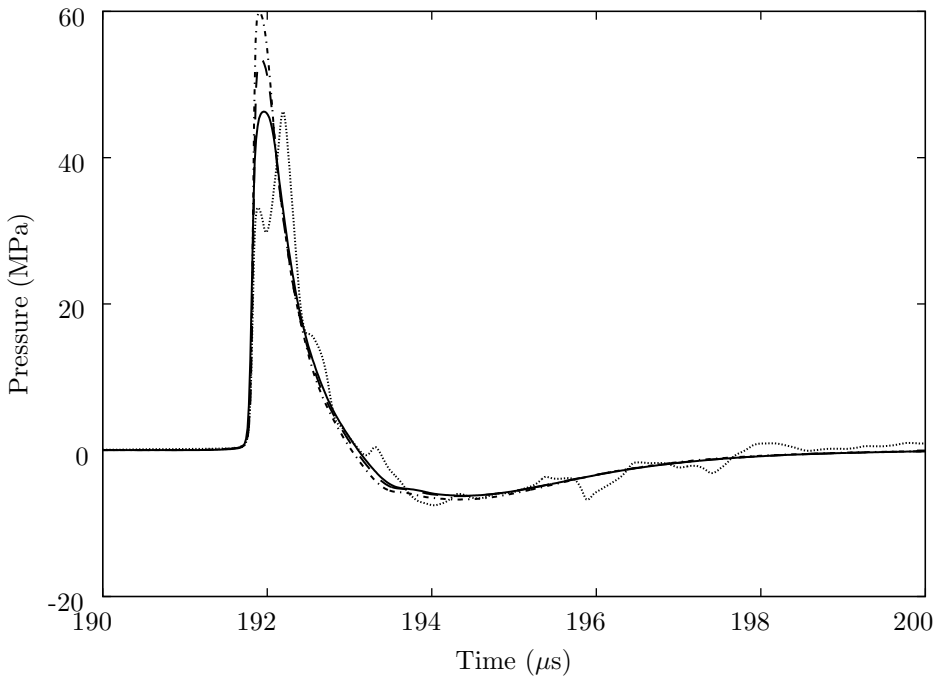

Figure 4.7: Pressure versus time at a point on the axis 5 mm postfocus for the Dornier HM3: water bath (———), with body cavity (– – –), with body cavity and kidney (-·-·-), VOXEL-MAN Group data (·····).

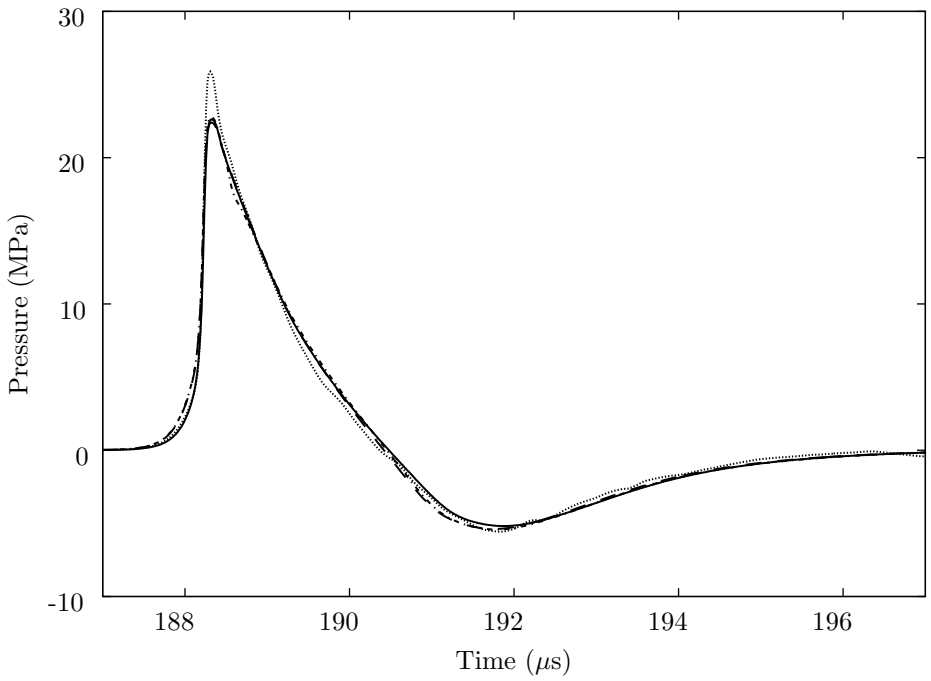

Figure 4.8: Pressure versus time in the focal plane 5 mm off-axis for the Dornier HM3: water bath (———), with body cavity (– – –), with body cavity and kidney (–·–·–), VOXEL-MAN Group data (·····).

4.4.2 Piezoelectric Lithotripter Array

Figure 4.9 shows the calculated pressure versus time for the piezoelectric lithotripter array for four cases: with the water bath, with the model body cavity alone, with the model body cavity and kidney together, and with the VOXEL-MAN Group data. Amplitudes increase when our simple anatomical models increase for the same reason as for the Dornier HM3: the weaker, off-axis portion of the focusing front moves more quickly than the stronger, near-axis portion, and counterintuitively focusing occurs more coherently in this case. This effect is much weaker for the piezoelectric lithotripter array than for the HM3, because at its inception, the focusing wavefront is of uniform strength. However, the diffractive wavefield behind the focusing front weakens the off-axis portion of the front more considerably than the near-axis front. Also, waveform healing causes adjustments to the focusing front near the axis that do not occur as strongly farther away from the axis. Also as we saw with the Dornier HM3, the leading compressive phase of the focal region waveform becomes double peaked with the use of the more complex geometries of the VOXEL-MAN Group data.

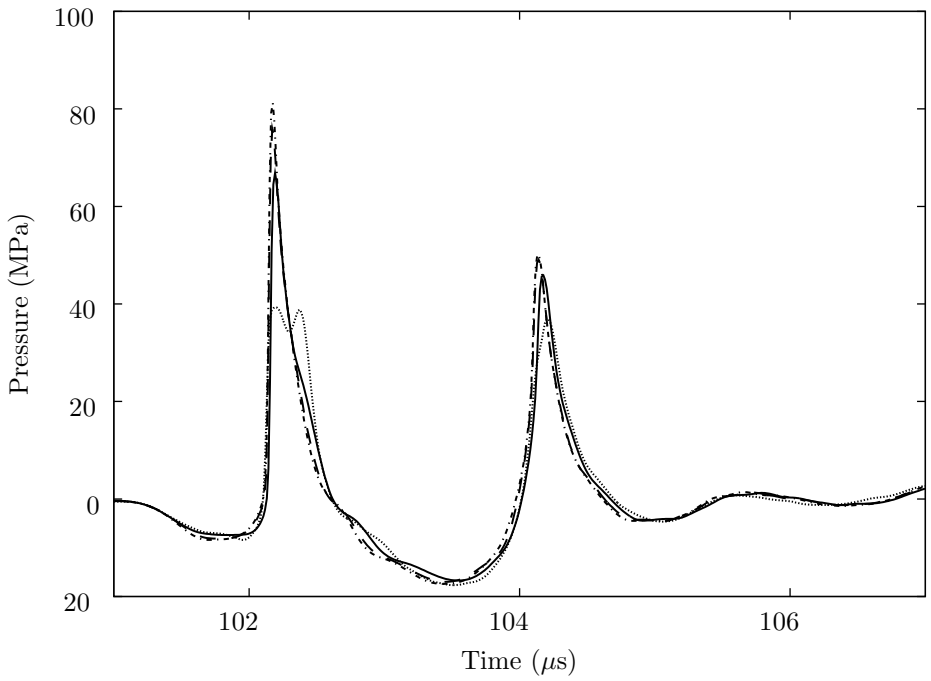

Figure 4.9: Pressure versus time at the focus for piezoelectric lithotripter array: water bath (———), body cavity (– – –), body cavity and kidney (–·–·–), VOXEL-MAN Group data (·····).

Figures 4.10 and 4.11 show the calculated pressure versus time at points 5 mm prefocus and postfocus, respectively. Results from the same four cases are shown: the water bath, the model body cavity alone, the model body cavity and kidney together, and the VOXEL-MAN Group data. Figure 4.10 shows how complex the wave structure is upstream of the focus. Even the results for the water bath case show a multiple peaked structure that vanishes at the focus. The VOXEL-MAN Group case produces waveforms with smaller amplitudes but larger temporal pulse widths. Figure 4.11 shows how much the character of these focal region waveforms change for the piezoelectric lithotripter array, the lithotripter with the smallest focal zone and largest focal region gradients of those we study. The multiple peaked structures have vanished for all cases, and amplitudes here are nearly three times as large as they are 5 mm prefocus, a spatial separation of only 1 cm. Finally, figure 4.12 shows the results from these same simulations 5 mm off-axis. Amplitudes are an order of magnitude smaller than those at the focus. The waveforms again exhibit multiple peaked structures here, consistent with the knowledge that the focal region has a 1 to 2 mm radius.

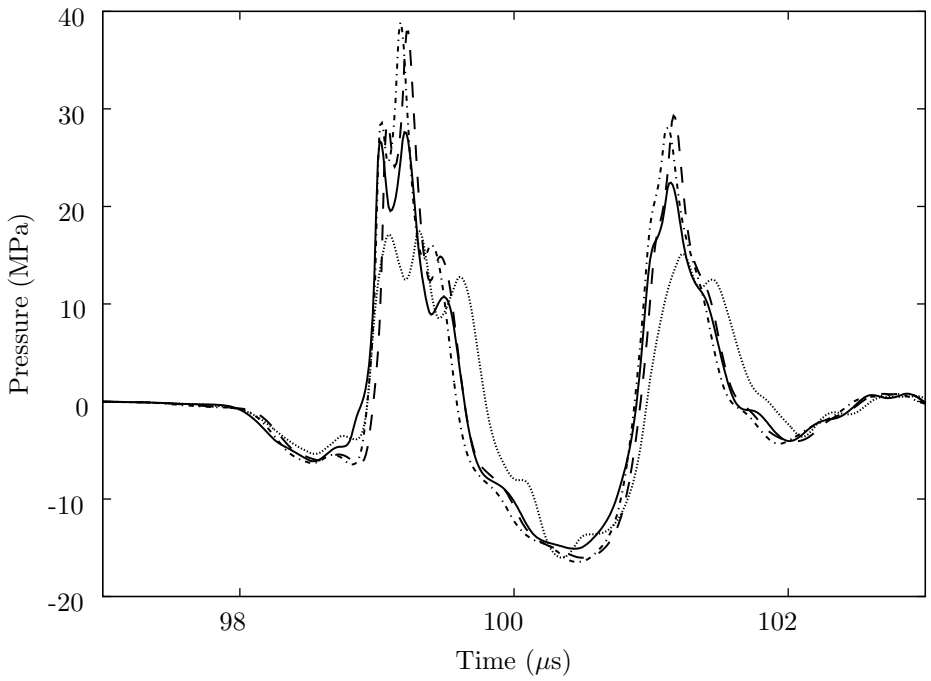

Figure 4.10: Pressure versus time at a point on the axis 5 mm prefocus for the piezoelectric lithotripter array: water bath (———), body cavity (– – –), body cavity and kidney (–·–·–), VOXEL-MAN Group data (·····).

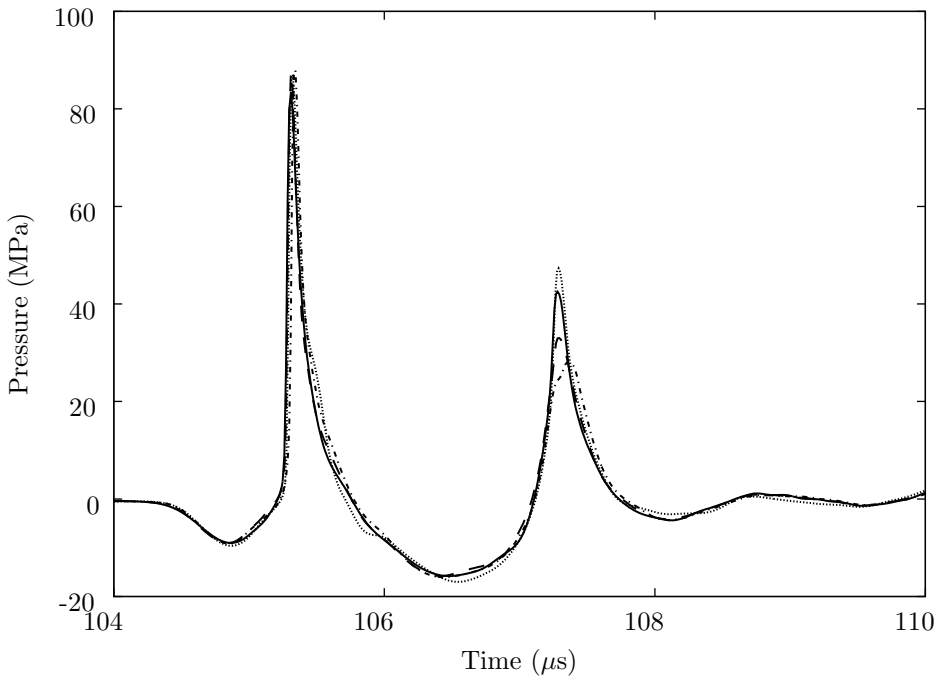

Figure 4.11: Pressure versus time at a point on the axis 5 mm postfocus for the piezoelectric lithotripter array: water bath (———), body cavity (– – –), body cavity and kidney (–·–·–), VOXEL-MAN Group data (·····).

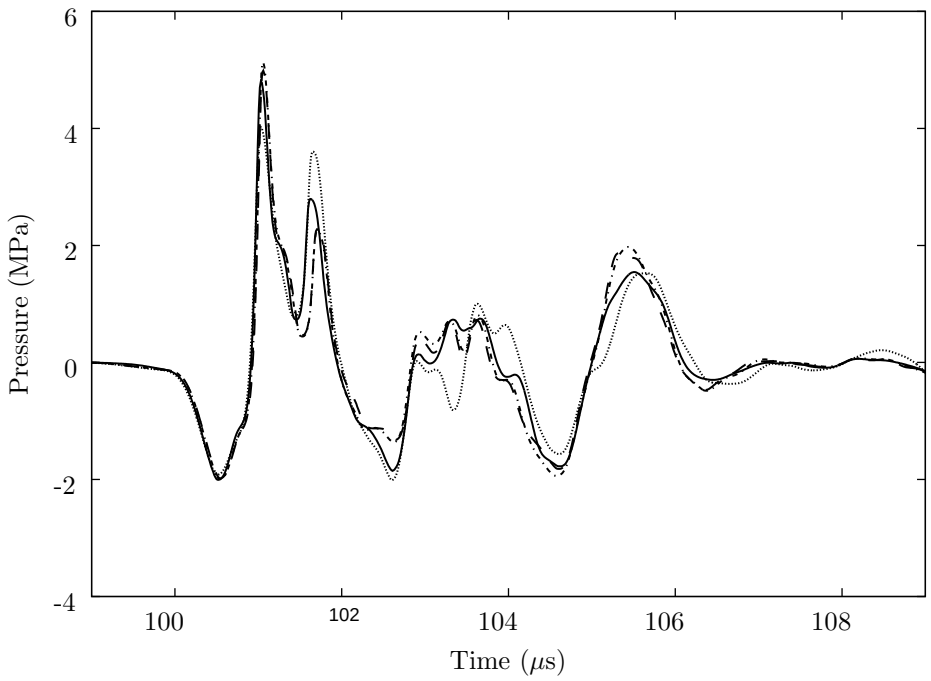

Figure 4.12: Pressure versus time at a point on the axis 5 mm off-axis for the piezoelectric lithotripter array: water bath (———), body cavity (– – –), body cavity and kidney (–·–·–), VOXEL-MAN Group data (·····).

4.4.3 XX-Es

Figure 4.13 shows the calculated pressure versus time at the focus for the XX-Es lithotripter. This waveform shows a trend that is evident for the other focal region waveforms for this particular lithotripter: very little difference is found between the waveforms computed using different heterogeneous materials in the focal region. As a result, we only show the waveforms at the focus, because the plots showing the waveforms 5 mm from the focus (prefocus, postfocus, and off-axis) would only differ trivially from the waveforms shown in figure 4.13.

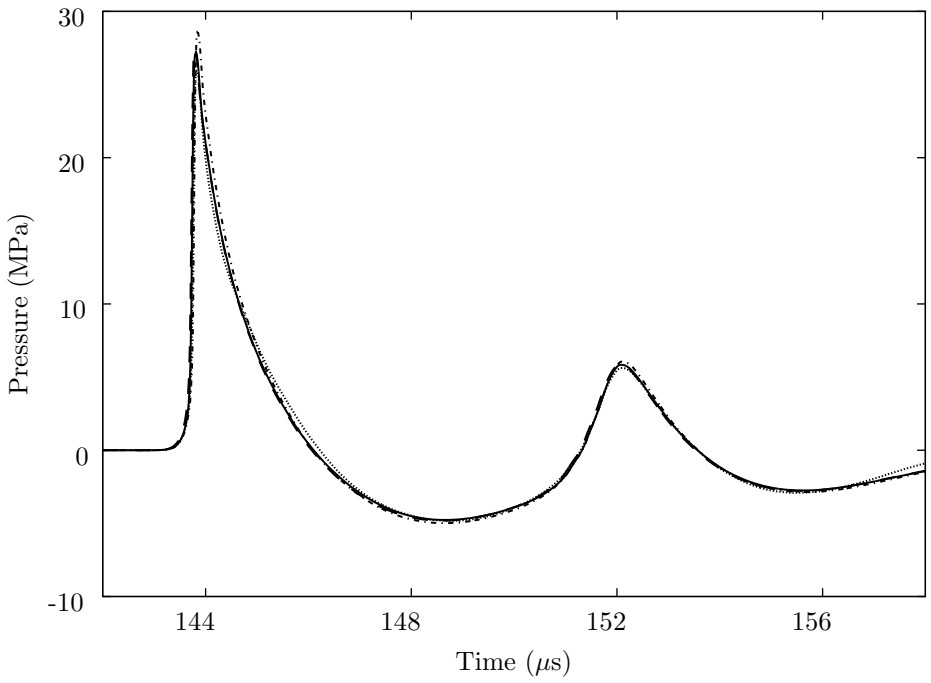

Figure 4.13: Pressure versus time at the focus for the XX-Es: water bath (———), body cavity (– – –), body cavity and kidney (–·–·–), VOXEL-MAN Group data (·····).

4.5 Maximum Pressures

If we plotted the pressures 25 mm postfocus and beyond, the water bath case would show higher pressure amplitudes than the model body cavity and kidney cases. The presence of the model anatomy basically shifts the higher pressures observed postfocally in the water bath case toward the focus, though the highest pressures are still observed postfocally. Figure 4.14 shows flooded contours of maximum pressure for the water bath case and the case where the VOXEL-MAN Group data is used. A global maximum pressure is found 35 mm postfocus. The 20 MPa contour is drawn on top of the flooded contours. We see that the radial extent of the region enclosed by the 20 MPa does not change appreciably when acoustic impedance interfaces are added to the focal region.

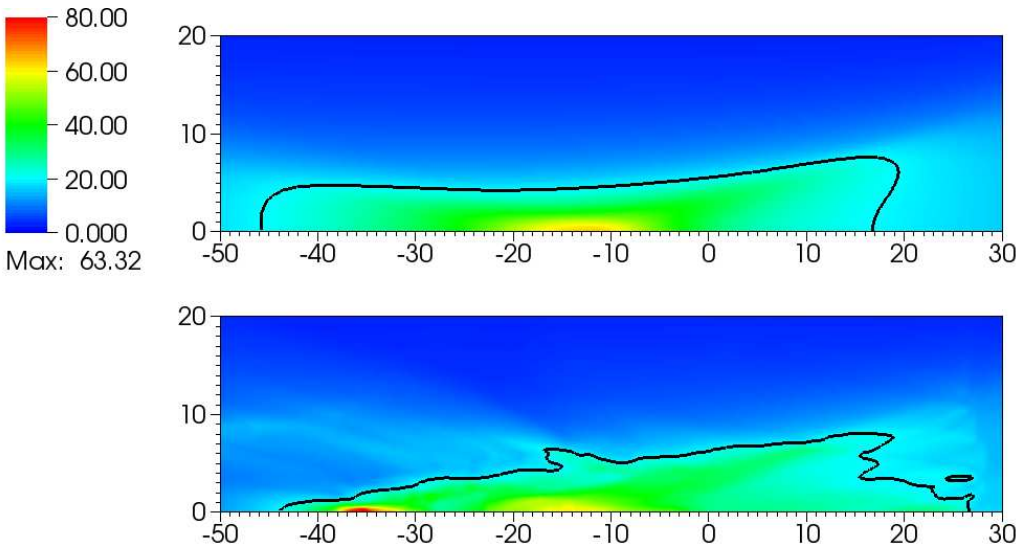

Figure 4.14: Flooded contour plots of maximum pressures for the Dornier HM3: water bath (top) and VOXEL-MAN Group (bottom) cases. Axis labels are distance from focus in millimeters. The 20 MPa contour line is drawn.

Figure 4.15 shows the maximum recorded pressure along the axis as a function of distance from the focus for the piezoelectric lithotripter array. The peak positive pressure within 20 mm of the focus falls between 60 and 80 MPa for all four cases. The pressure in this region decreases slightly, by approximately 5 MPa when the VOXEL-MAN Group data is used. The most significant difference between all the cases is the large jump in pressures 30 to 40 mm postfocus for the VOXEL-MAN Group case. The other cases produce pressures between 20 and 30 MPa in this region. The VOXEL-MAN Group case produces a peak positive pressure over 90 MPa in this region. This effect was also shown in the flooded contour data in figure 4.14. Tissue in this region, which at 3 to 4 cm downstream is outside the scope of the kidney, will feel a much stronger insult than would have been predicted using the water bath data alone.

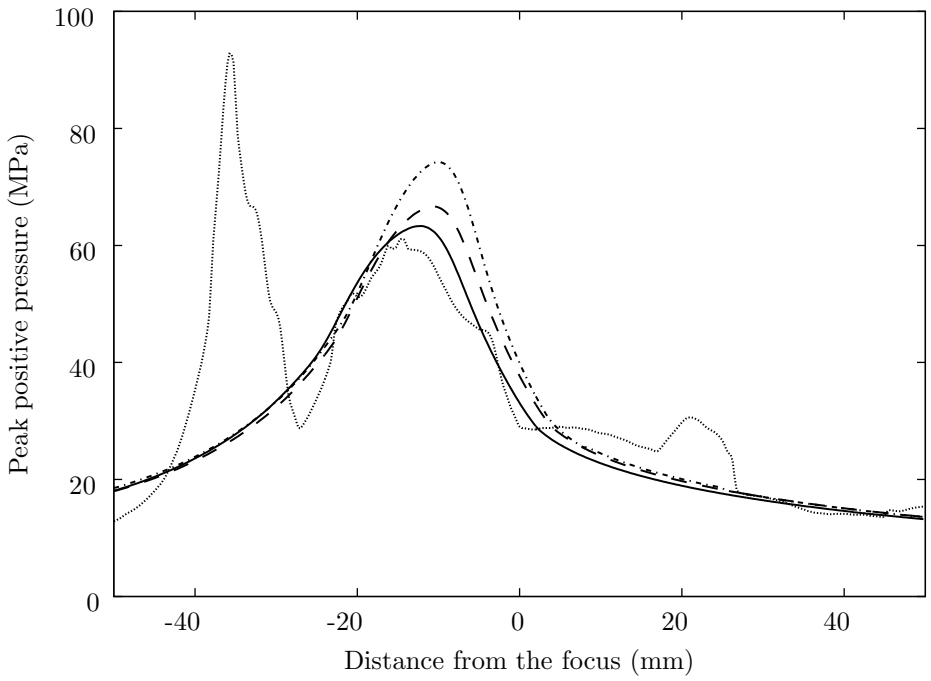

Figure 4.15: Peak positive pressure recorded along the axis as a function of distance from the focus for the Dornier HM3: water bath (———), body cavity (– – –), body cavity and kidney (–·–·–), VOXEL-MAN Group data (·····).

Figure 4.16 shows the maximum recorded pressure along the axis as a function of distance from the focus for the piezoelectric lithotripter array. The peak positive pressure for all cases falls between 70 and 80 MPa. For the water bath case, a peak positive pressure of 72 MPa is found 5 mm postfocus. The body cavity model alone and the body cavity and kidney models together produce peak positive pressures of 73 and 76 MPa, respectively, which are found 3 mm postfocus. Use of the VOXEL-MAN Group data produces the highest peak pressure of 79 MPa, which is found 5 mm postfocus.

Between 15 and 30 mm postfocus, the VOXEL-MAN Group data case produces peak positive pressures that are 5 to 10 MPa smaller than the pressures computed for the other cases. A secondary, local maximum in peak positive pressure is found for this case between 30 and 35 mm postfocus, where peak positive pressures are between 20 and 25 MPa, compared with peak positive pressures between 10 and 15 MPa found for the other cases.

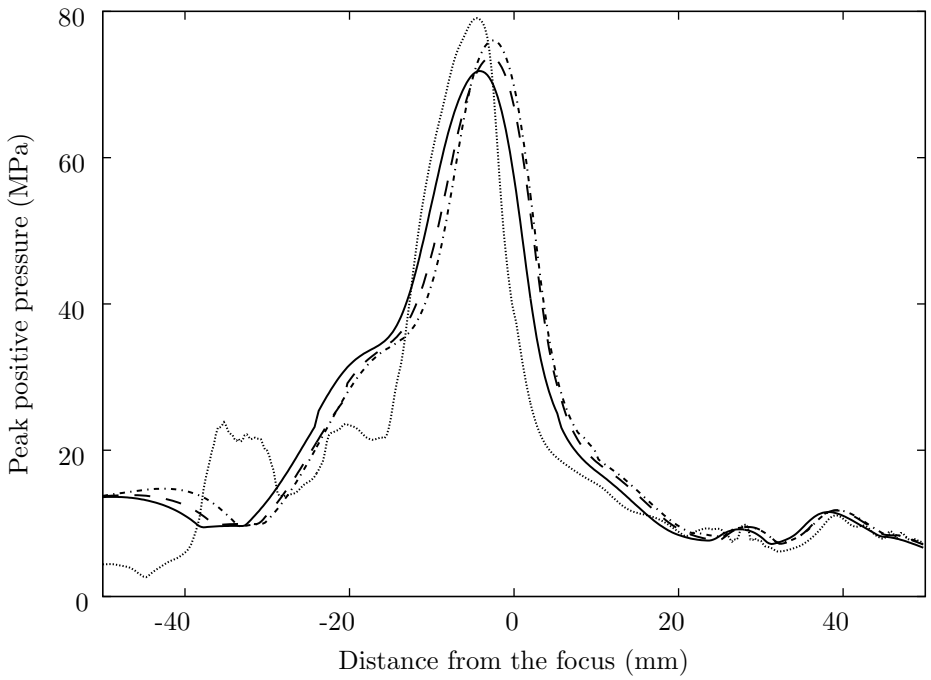

Figure 4.16: Peak positive pressure recorded along the axis as a function of distance from the focus for the piezoelectric lithotripter array: water bath (———), body cavity (– – –), body cavity and kidney (–·–·–), VOXEL-MAN Group data (·····).

Figure 4.17 shows the maximum recorded pressure along the axis as a function of distance from the focus for the XX-Es. The water bath case and the case where we use the body cavity alone produce almost identical results. In these cases, a peak positive pressure of 27 MPa is found very near the focus. When the body cavity and kidney models are used together, a peak positive pressure around 29 MPa is found 12 mm postfocus. Use of the VOXEL-MAN Group data produces a much more oscillatory structure than the other cases. Here a peak positive pressure of 29 MPa is found 15 mm prefocus. Beginning from this axial location, peak positive pressures for this last case are consistently below those for the other cases, by as much as 10 MPa.

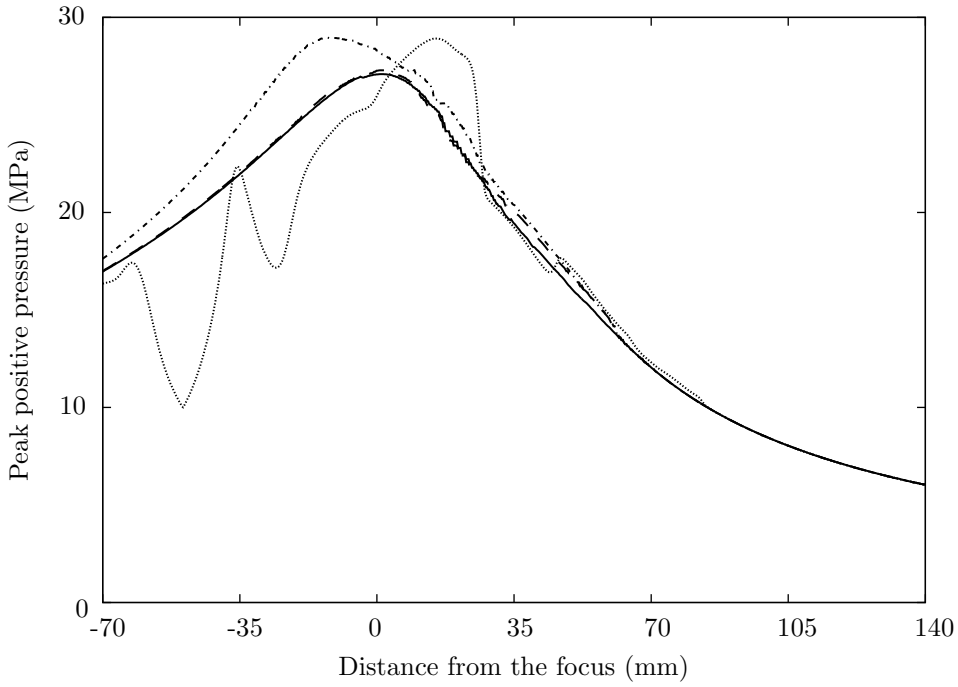

Figure 4.17: Peak positive pressure recorded along the axis as a function of distance from the focus for the XX-Es: water bath (——), body cavity (– – –), body cavity and kidney (–·–·–), VOXEL-MAN Group data (·····).

4.6 Pulse Intensity Integral

The pulse intensity integral (PII) measures the amount of acoustic energy per unit area being carried by a propagating wave. We can define the PII by

$$PII(\vec{x},t) = \int p(\vec{x},t)u(\vec{x},t)dt, \tag{4.5}$$

where $p(\vec{x},t)$ and $u(\vec{x},t)$ are the pressure and velocity magnitude, respectively, at the point with position vector $\vec{x}$ at time t. The units for PII are reported as J/m^2. In our simulations, we recorded the maximum PII at each spatial location over the duration of the simulation and then selected the largest such value in the computational domain as the reported peak PII. If we assume the temporal pulse length is t_p, we can estimate the acoustic intensity $I(\vec{x},t)$, which has units of W/cm^2, as

$$I(\vec{x},t) = \frac{PII(\vec{x},t)}{t_p}. \tag{4.6}$$

Figure 4.18 shows the PII as a function of distance from the focus along the axis for the Dornier HM3. The water bath case and the body cavity model alone produce peak PII values near 645 J/m^2 from 7 to 10 mm postfocus. The body cavity and kidney models together yield a nearly 15% increase in PII to 735 J/m^2 8 mm postfocus. The VOXEL-MAN Group data produces a peak PII value of 580 J/m^2 around 10 mm postfocus and a secondary maximum of 510 J/m^2 around 35 mm postfocus, whereas the other cases produce PIIs around 200 J/m^2 here. Hence all the peak PII values, regardless of the material structure in the focal region, are found around 1 cm postfocus.

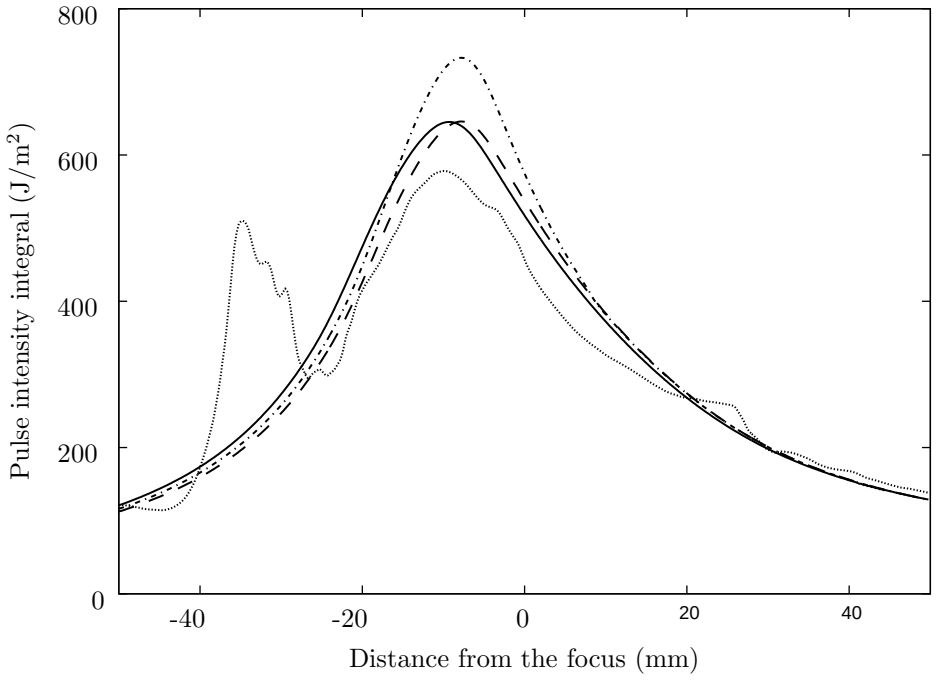

Figure 4.18: Pulse intensity integral (J/m^2) calculated along the axis as a function of distance from the focus for the Dornier HM3: water bath (———), body cavity (– – –), body cavity and kidney (–·–·–), VOXEL-MAN Group data (·····).

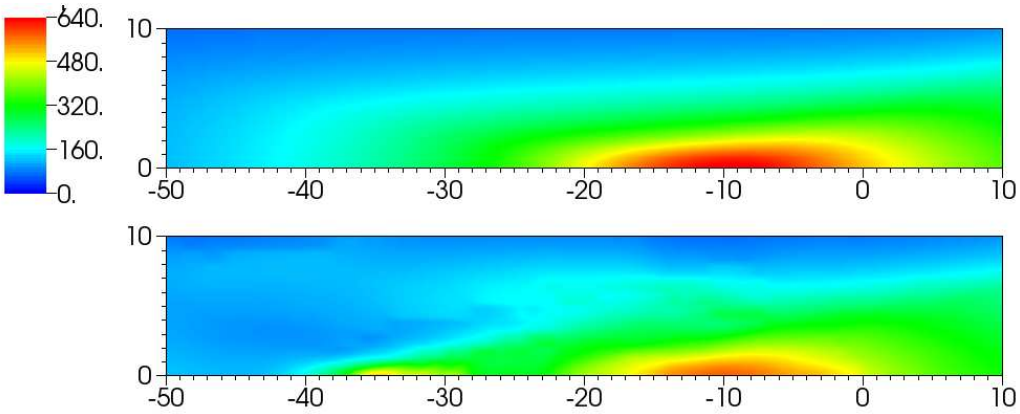

Figure 4.19: Flooded contour plot of pulse intensity integral (J/m^2) in the neighborhood of the focus for the Dornier HM3. The units of distance on the abscissa and ordinate are in mm. The focus is at (0,0). Results for the water bath case (top) and using VOXEL-MAN Group data (bottom).

Figure 4.20 shows the PII as a function of distance from the focus along the axis for the piezoelectric lithotripter array. The water bath case produces peak PII values of 685 J/m^2 3 mm postfocus. When the body cavity model alone and body cavity and kidney models together are used, peak PII values of 660 and 690 J/m^2, respectively, are found 1 mm postfocus. Use of the VOXEL-MAN Group data produces the largest PII value near 710 J/m^2, which is seen 3 mm postfocus. The piezoelectric lithotripter consistently produces peak values for all the relevant flow variables within 5 mm of the focus, as compared with the other two lithotripters where maximum values can be found centimeters from the focus. The VOXEL-MAN Group data produces a second local maximum of 180 J/m^2 30 mm postfocus, almost a factor of four smaller than the peak value found near the focus for this case.

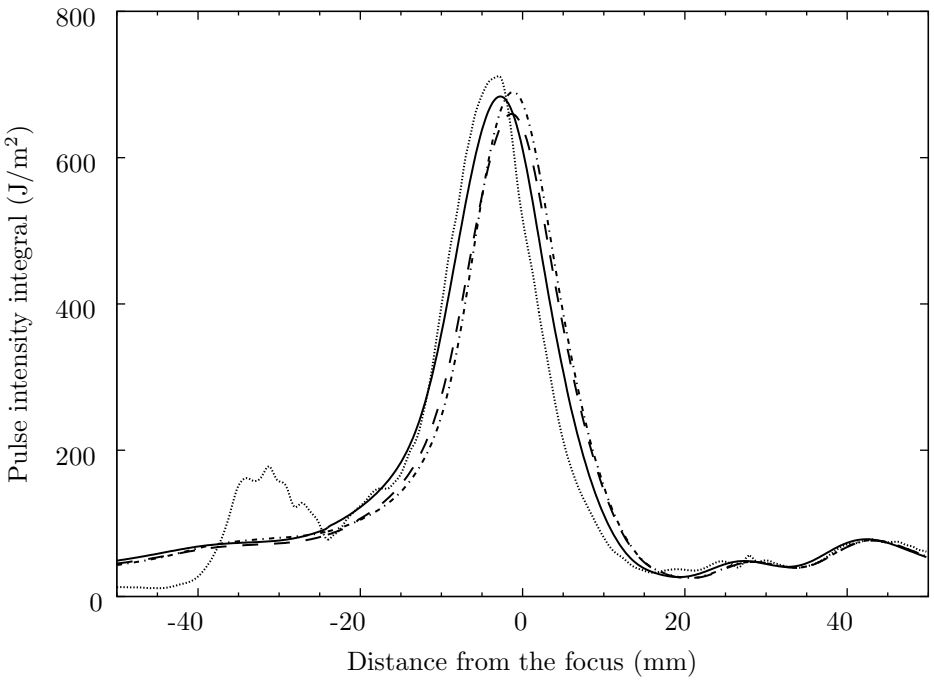

Figure 4.20: Pulse intensity integral (J/m^2) calculated along the axis as a function of distance from the focus for the piezoelectric lithotripter array: water bath (——), body cavity (– – –), body cavity and kidney (–·–·–), VOXEL-MAN Group data (·····).

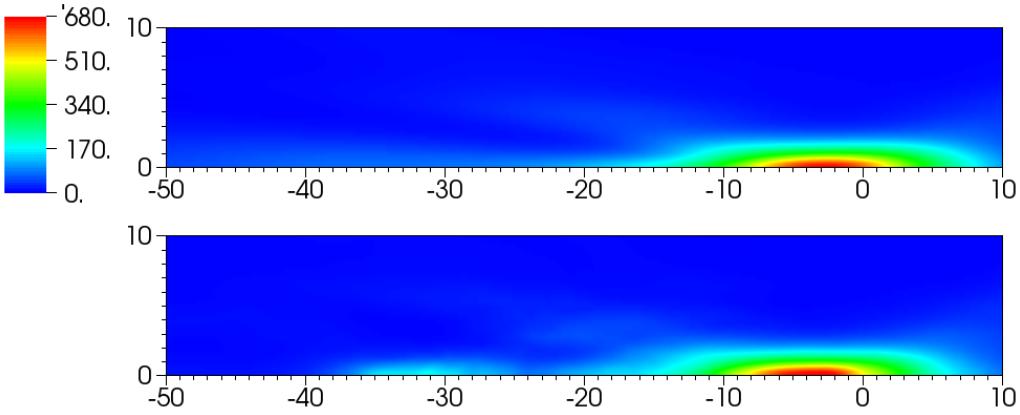

Figure 4.21: Flooded contour plot of pulse intensity integral (J/m^2) in the neighborhood of the focus for the piezoelectric lithotripter array. The units of distance on the abscissa and ordinate are in mm. The focus is at (0,0). Results for the water bath case (top) and using VOXEL-MAN Group data (bottom).

Figure 4.22 shows the PII as a function of distance from the focus along the axis for the XX-Es. The water bath case, and the cases where the body cavity model is used alone and the body cavity

and kidney models are used together generate maximum PII values of 330 J/m^2 approximately 35 mm prefocus. Use of the VOXEL-MAN Group data produces a maximum PII near 370 J/m^2 found 25 mm prefocus. In addition to this global maximum on the axis, a secondary maximum PII of 280 J/m^2 is found 60 mm postfocus.

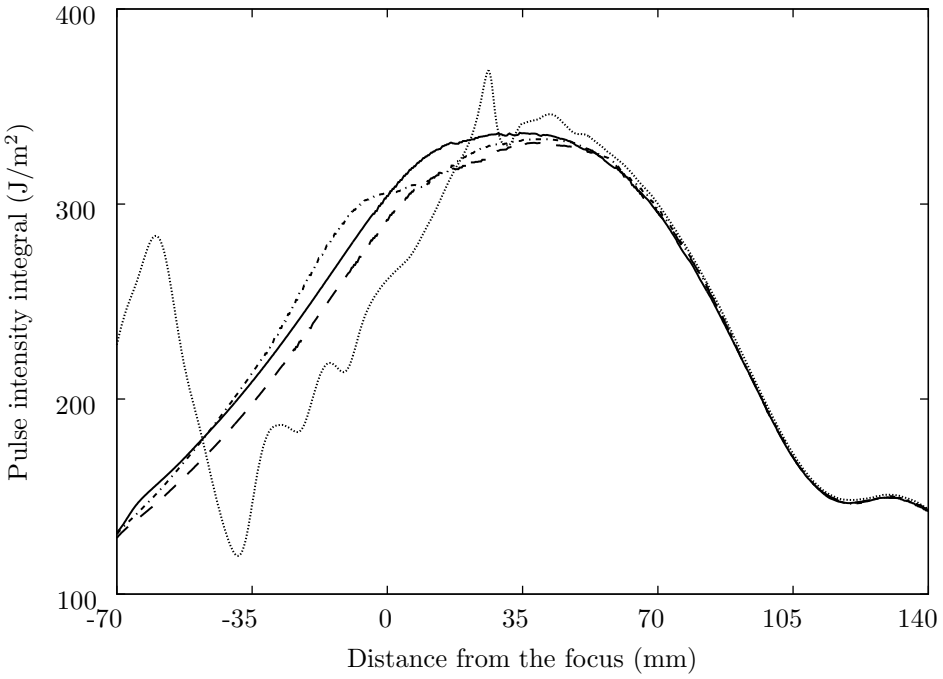

Figure 4.22: Pulse intensity integral (J/m^2) calculated along the axis as a function of distance from the focus for the XX-Es: water bath (———), body cavity (– – –), body cavity and kidney (–·–·–), VOXEL-MAN Group data (·····).

4.7 Summary

In this chapter, we discussed our strategy for introducing materials into the domain that vary in density and sound speed from their surroundings. We prescribed nonuniform densities directly, and to achieve sound speed contrasts we altered the distribution of parameters of the equation of state. We then discussed the expected changes when introducing models for the scattering and absorption that would be found in an *in vivo* environment. We described different models we use, both simple geometrical models we devised ourselves and real anatomical data used directly as inputs. We then studied the changes seen in focal region waveforms, maximum pressure distributions, and pulse intensity integral

distributions.

Chapter 5

Soft Tissue Injury Mechanisms

5.1 Overview

The debate is still open regarding how exactly soft tissue is injured during a typical shock wave lithotripsy treatment. Two often discussed mechanisms are the growth and collapse of bubbles, often within the vasculature in the focal region, and direct tearing as a result of the passage of the shock wave. These mechanisms were discussed in Section 1.3.3. We use surrogates for the damage resulting from each of these mechanisms. In the case of cavitation damage, we will examine the peak negative pressures computed in each lithotripter type. Specifically, for each point in the domain, we record the strongest negative pressure experienced over the course of the entire simulations. These pressure maps will give us insight regarding where the areas of most intense cavitation are likely to be found. For direct shock damage, we will use the maximum principal and shear strains as the surrogate for damage since it is the pulling and tearing of tissue that is likely to cause damage via this mechanism. Studying how these quantities vary across the different lithotripters and through different anatomical models, we will discuss the potential for soft tissue damage in each case.

5.2 Strain Metrics

Ionescu et al. studied failure in soft tissues composed of a matrix supported by fiber bundles[50]. In their work, strain criteria were used to identify failure of each component. Maximum shear and tensile strain thresholds were used to determine failure of the matrix and fibers, respectively. In our case, because we are modeling the various anatomical structures homogeneously, we will adopt the shear

strain metric as a surrogate for potential tissue damage. We will have a brief change of notation in our discussion of strain metrics. Up to this point, we have used $u(\vec{x},t)$ and $v(\vec{x},t)$ to represent the axial and radial velocities, respectively, at point $\vec{x}$ and time t. In this section, we use $v_z(\vec{x},t)$ and $v_r(\vec{x},t)$ to represent the axial and radial velocities. Now we will use $u_z(\vec{x},t)$ and $u_r(\vec{x},t)$ to represent the displacement computed at point $\vec{x}$ from time zero up to time t. These displacements are given as

$$u_z(\vec{x},t) = \int_0^t v_z(\vec{x},\tau)d\tau, \qquad u_r(\vec{x},t) = \int_0^t v_r(\vec{x},\tau)d\tau. \tag{5.1}$$

We should mention that these calculated displacements are not actually the displacement of any single particle in our computational domain. These calculations are Eulerian, and because they are made at a fixed point in space, they will not represent the motion of the particle that originates at point $\vec{x}$. We use these computed displacements as estimates for the actual displacement of the particle that began the simulation at point $\vec{x}$. We feel this approximation is appropriate for at least two reasons. First, the maximum particle drift over the course of the simulation is less than 100 μm, which is between 3 and 4 cell widths on the finest mesh. Focal pressure waveforms for all the lithotripters show trivial changes within 250 μm of the focus itself. This region is where velocity gradients should be greatest. Conditions experienced by a given particle thus will change very little over a drift of 100 μm. Second, we assume tissue would deform exactly as the fluids we use in our simulation. We neglect the mechanical properties of the tissue that would cause its displacement to deviate from that which we calculate. Tens or hundreds of microns of difference between the actual motion and our calculated estimates seem reasonable.

Now that we have access to displacements at each cell in our domain, we can compute estimates for the infinitesimal strain tensor at each cell. In an axisymmetric geometry, the infinitesimal strain tensor ϵ is given as

$$\epsilon = \begin{bmatrix} \dfrac{\partial u_r}{\partial r} & 0 & \dfrac{1}{2}\left(\dfrac{\partial u_z}{\partial r} + \dfrac{\partial u_r}{\partial u_z}\right) \\ 0 & \dfrac{u_r}{r} & 0 \\ \frac{1}{2}\left(\dfrac{\partial u_r}{\partial z} + \dfrac{\partial u_z}{\partial r}\right) & 0 & \dfrac{\partial u_z}{\partial z} \end{bmatrix}. \tag{5.2}$$

The three eigenvalues $\epsilon_p^{(i)}$ of the infinitesimal strain tensor are the three principal strains for the given infinitesimal tissue element. We choose the maximum of these principal strains at each point over the course of the simulation as one surrogate for the damage potential of the passing shock wave. The maximum shear strain ϵ_s at each point over the course of the domain is also used as a surrogate for damage potential and is given as

$$\epsilon_s = \frac{1}{2}\left[\epsilon_p^{(1)} - \epsilon_p^{(3)}\right], \tag{5.3}$$

where $\epsilon^{(1)}$ and $\epsilon^{(3)}$ are the maximum and minimum principal strains, respectively.

Estimates for the strain induced by the passage of a single shock wave through tissue are less than 2%[37]. Freund et al. noted these values are much less than the 10% threshold that is seemingly required to initiate damage in kidney parenchyma and proposed a cumulative shear hypothesis. Rather than the shear induced by a single shock, it could be the cumulative effect of many (hundreds, possibly thousands of) shock waves that initiate damage in SWL. While it is beyond the scope of this work to simulate the firing of hundreds of shocks that would occur in a SWL treatment, we can identify areas where our shear strain estimates are highest and thus are most likely to be sites of damage via the cumulative shear hypothesis.

5.3 Maximum Strain

We will now examine the distribution of maximum principal normal and shear strains for the Dornier HM3, the piezoelectric lithotripter array, and the XX-Es. The strain data for the *in vitro* case will be compared with the case where we use the body cavity model alone, the body cavity and kidney models together, and the VOXEL-MAN Group data.

5.3.1 Principal Normal Strain

The *in vitro* case shows a maximum principal normal strain of 0.25% 10 mm prefocus, as shown in figure 5.1. The use of the body cavity model alone and the body cavity and kidney models together actually decrease the maximum principal normal strain. In these two cases, strains between 0.23% and

0.24% are observed 8 to 12 mm prefocus. One reason these anatomical models reduce strain relative to the *in vitro* case is related to the reason we see a deformed shock tip in the calculated focal pressure profile *in vitro*. When no anatomical models are used, the portion of the shock front along the axis is stronger than the off-axis portion and thus travels at a faster speed. The near-axis portion of the front then arrives at the focus before the off-axis portion, and the delayed arrival of this latter portion of the front creates a secondary, smooth increase in pressure at the focus after arrival of the incident focused shock front.

When using the body cavity and kidney models, the off-axis portion of the focusing front encounters the higher speed materials before the near-axis portion, and the delay in arrival times of the different portions of the front is decreased. As a result, the shock tip begins to recover its expected form, as shown in figure 4.5. Likewise, strains are actually decreased as a result of the use of these models, because the pressure gradients near the focus become weaker as the different waveform components focus more coherently. This result does not match the expectation for focusing in an actual *in vivo* environment and occurs only because the axisymmetry of our simulation counter-intuitively disrupts the focusing of the *in vitro* case slightly. If we could capture the small perturbations in the azimuthal direction that almost certainly occur experimentally, the *in vitro* strains would likely be lower than we calculate, and the use of the anatomical models would produce the expected result of an increase in focal region strains.

Use of the VOXEL-MAN Group data creates a divergence from the trends of the other cases. The peak principal normal strain shows multiple local maxima along the axis. A strain of 0.27% is observed 27 mm prefocus, while strains between 0.2% and 0.36% are found between 20 and 40 mm postfocus. Maximum normal strains 50% larger than observed at the focus are thus found several centimeters beyond the focus in this case, outside of the kidney and possibly affecting other organs, e.g., the pancreas, where damage has been observed as a result of extracorporeal shock wave lithotripsy treatment for kidney stones[47].

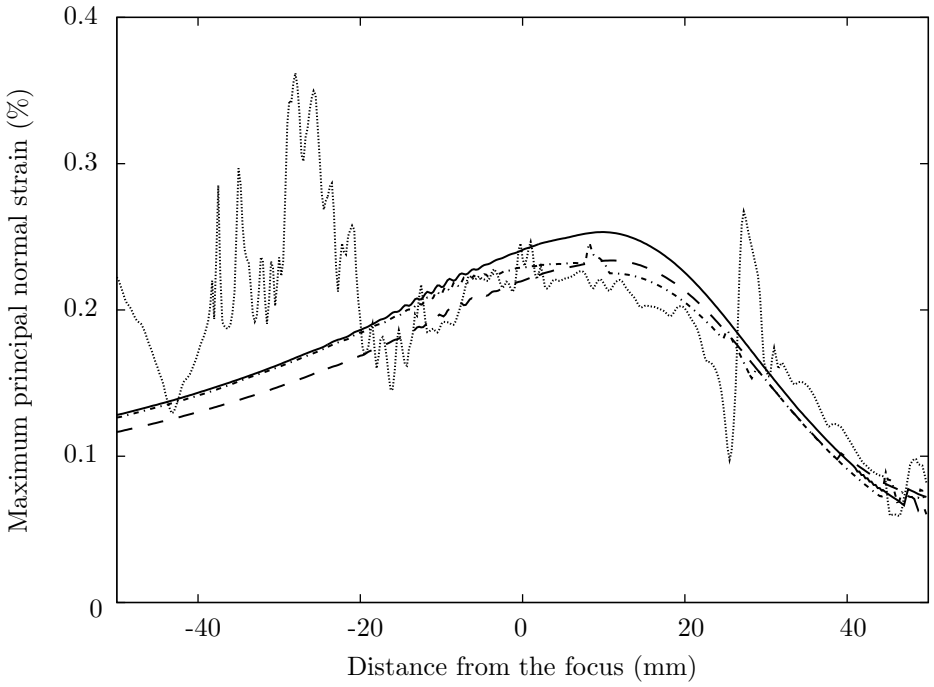

Figure 5.1: Maximum principal normal strain (%) recorded along the axis as a function of distance from the focus for the Dornier HM3: water bath (——), body cavity (– – –), body cavity and kidney (–·–·–), VOXEL-MAN Group data (·····).

Figure 5.2 shows the maximum principal normal strain, as a percentage, as a function of distance from the focus along the axis for the piezoelectric lithotripter array. Peak strains between 0.5% and 0.6% are observed for all cases within 3 mm of the focus. These strains are approximately twice as large as the normal strains observed near the focus for the Dornier HM3. Another trend for the piezoelectric lithotripter array is that the body cavity model alone and the body cavity and kidney models together produce results very similar to the *in vitro* case. We see this trend here for normal strain data, and we will see it for peak shear strains and negative pressures as well. As with the Dornier HM3, use of the VOXEL-MAN Group data produces a secondary local maximum in normal strain data. Strains of around 0.45% are found 25 to 35 mm postfocus.

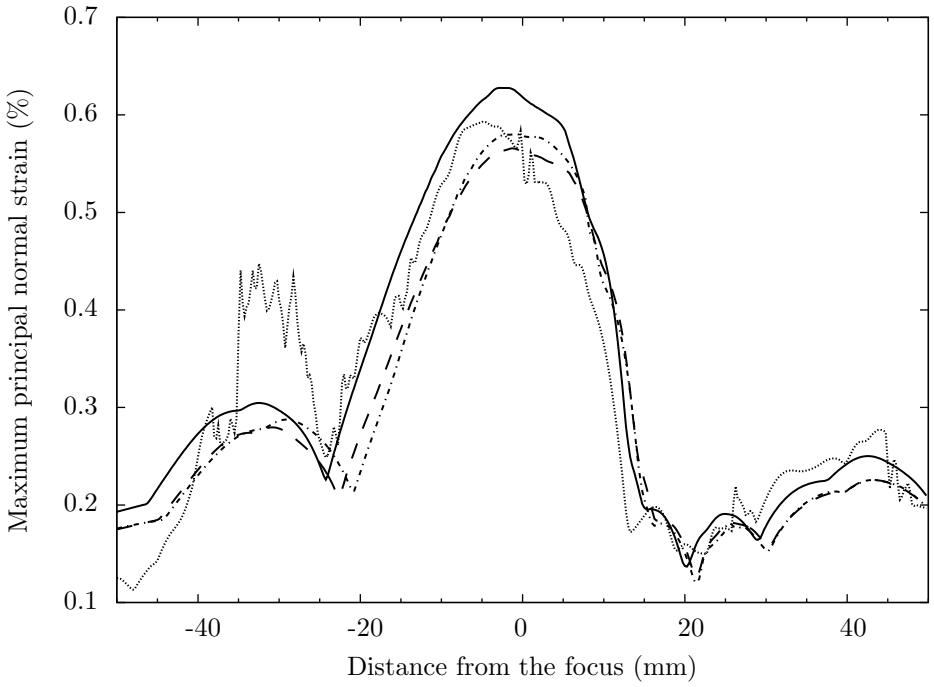

Figure 5.2: Maximum principal normal strain (%) recorded along the axis as a function of distance from the focus for the piezoelectric lithotripter array: water bath (———), body cavity (– – –), body cavity and kidney (–·–·–), VOXEL-MAN Group data (·····).

Figure 5.3 shows the maximum principal normal strain, as a percentage, as a function of distance from the focus along the axis for the XX-Es. This lithotripter again shows different trends than the other two lithotripters we simulate. Here peak strains of 0.4% are found 110 to 140 mm prefocus, outside the body cavity in a vast majority of treatments. Within the body cavity, nominally beginning at 60 mm prefocus, strains between 0.15% and 0.3% are found nearly uniformly along the axis. The behavior is oscillatory, as expected, but the variations in normal strain along the axis are weaker for the XX-Es than for the other lithotripters.

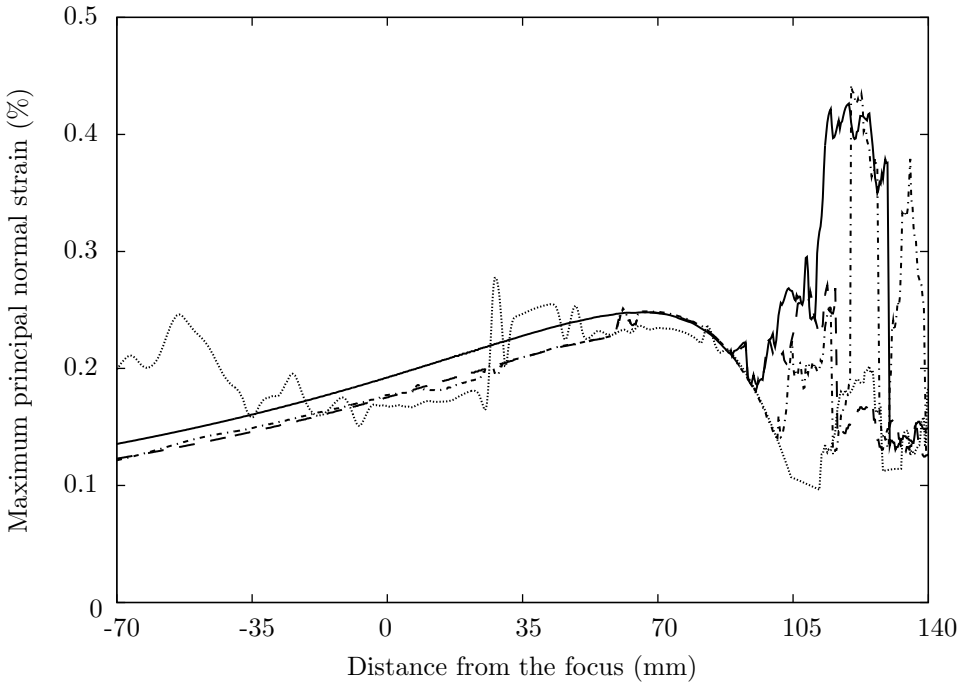

Figure 5.3: Maximum principal normal strain (%) recorded along the axis as a function of distance from the focus for the XX-Es: water bath (———), body cavity (– – –), body cavity and kidney (–·–·–), VOXEL-MAN Group data (·····).

5.3.2 Shear Strain

We will now study the maximum shear strains calculated to occur in each of the three lithotripters when the various heterogeneous materials are used. Figure 5.4 shows these values along the axis for the Dornier HM3 lithotripter. The *in vitro* case shows a peak strain of 1.25% about 12 mm postfocus. Two differences are already seen between the shear strain and normal strain data for the HM3: the shear strain values are larger, almost by an order of magnitude, and the peak values near the focus are found postfocally, rather than prefocally for the normal strains. Most observed damage occurs at the focal site or postfocally, an observation with which our calculations are in agreement. The body cavity model alone and the body cavity and kidney models together produce shear strains of 1.2% and 1.3%, respectively, which are found 10 mm postfocus.

Use of the VOXEL-MAN Group data produces smaller shear strains than the other cases in the 20 mm region immediately postfocus. As with the normal strains, though, this case produces a second shear strain maximum of 1.6% approximately 35 mm postfocus, a strain that is larger than those found

with 20 mm of the focus. We again find a situation where peak strains are found sufficiently far from the focus as to impact other anatomical structures from the kidney entirely.

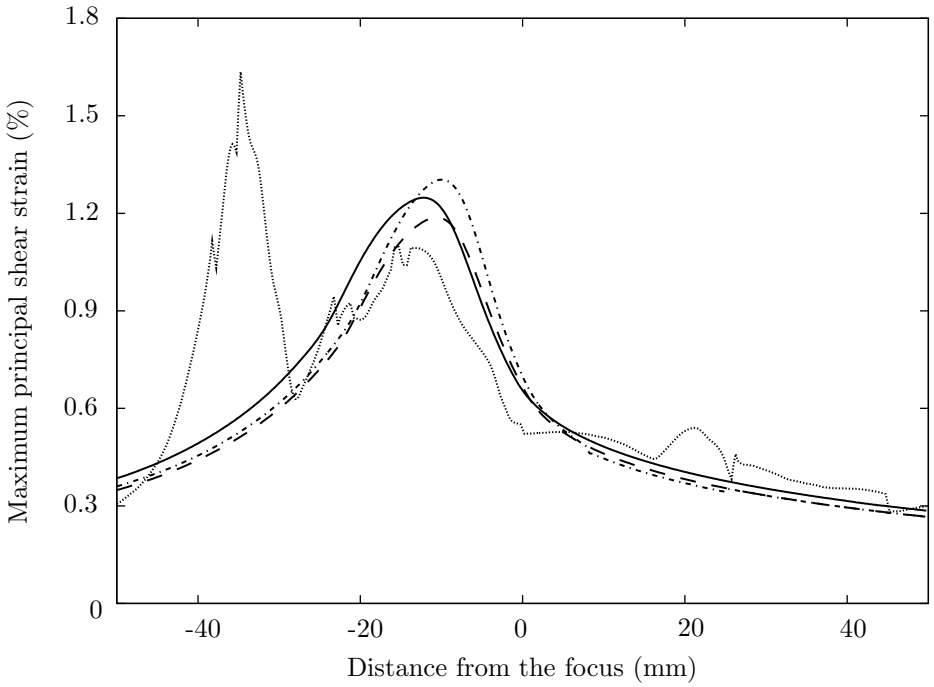

Figure 5.4: Maximum principal shear strain (%) recorded along the axis as a function of distance from the focus for the Dornier HM3: water bath (———), body cavity (– – –), body cavity and kidney (–·–·–), VOXEL-MAN Group data (·····).

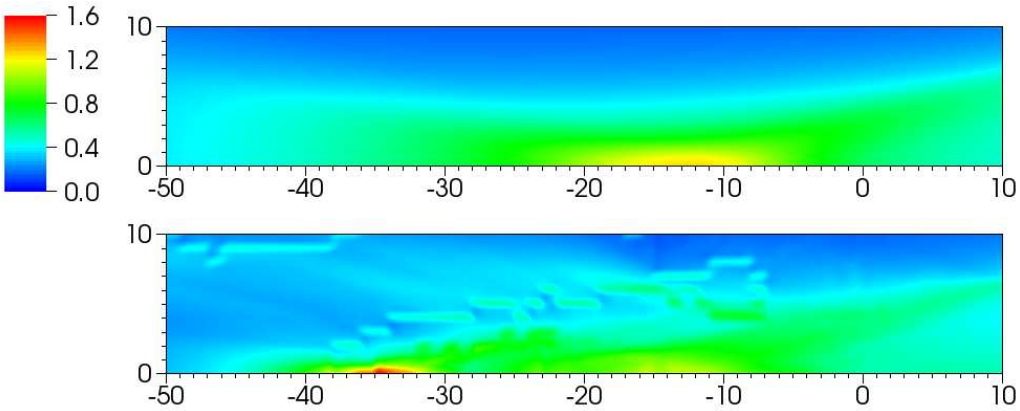

Figure 5.5: Flooded contour plot of maximum shear strain (%) in the neighborhood of the focus for the Dornier HM3. The units of distance on the abscissa and ordinate are in mm. The focus is at (0,0). Results for the water bath case (top) and using VOXEL-MAN Group data (bottom).

Figure 5.6 shows the maximum principal shear strain, as a percentage, as a function of distance from the focus along the axis for the piezoelectric lithotripter array. The *in vitro* case produces a peak strain of 1.32% found 4 mm postfocus. The body cavity model alone and body cavity and kidney models together produce peak strains of 1.22% and 1.24%, respectively, 2 mm postfocus. The VOXEL-MAN Group data shows a peak strain close to 1.35% about 5 mm postfocus.

These shear strains are comparable to those produced by the Dornier HM3. In this case, use of the VOXEL-MAN Group data produces a secondary shear strain maximum of 0.45% between 32 and 35 mm postfocus. A secondary shear strain peak was seen with the Dornier HM3 as well, but in that case the shear strain several centimeters beyond the focus was larger than the focal shear strains. For the piezoelectric lithotripter array, the focal region strains are a factor of three larger than the secondary strain maximum. Using this metric alone, we would expect strain damage to primarily be found near the focus for this lithotripter, while for the Dornier HM3, two sites of nominally equally high strain are found, one at the focus and one 3 to 4 cm postfocus.

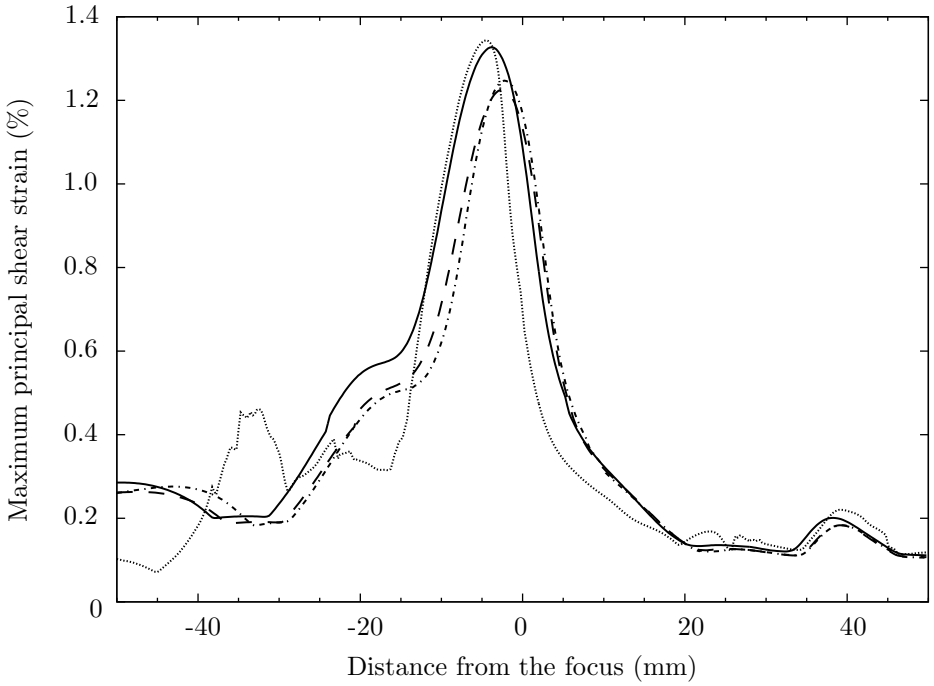

Figure 5.6: Maximum principal shear strain (%) recorded along the axis as a function of distance from the focus for the piezoelectric lithotripter array: water bath (———), body cavity (– – –), body cavity and kidney (–·–·–), VOXEL-MAN Group data (·····).

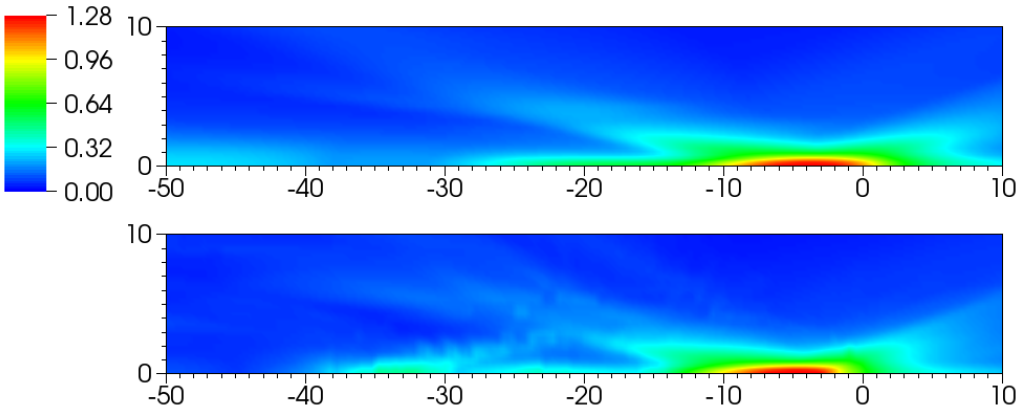

Figure 5.7: Flooded contour plot of maximum shear strain (%) in the neighborhood of the focus for the piezoelectric lithotripter array . The units of distance on the abscissa and ordinate are in mm. The focus is at (0,0). Results for the water bath case (top) and using VOXEL-MAN Group data (bottom).

Figure 5.8 shows the maximum principal shear strain, as a percentage, as a function of distance from the focus along the axis for the XX-Es. The shear strain trends for this lithotripter are considerably different from the normal strain trends. The *in vitro* case produces the largest shear strains seen in any of our XX-Es simulations, with a strain of 0.57% being found within 2 mm of the focus. The body cavity model produces a maximum shear strain of 0.52% also found within 2 mm of the focus. When the body cavity and kidney models are both used, peak strains near 0.55% are seen 12 mm postfocus. The VOXEL-MAN Group data produces strain amplitudes that oscillate along the axis. The largest strain of 0.52% found 15 mm prefocus.

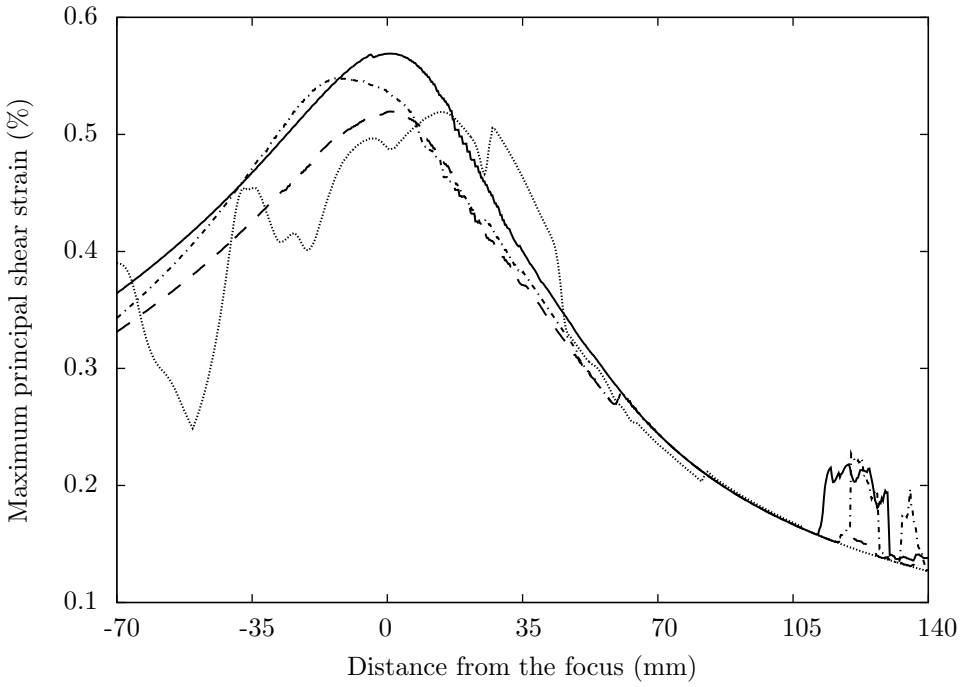

Figure 5.8: Maximum principal shear strain (%) recorded along the axis as a function of distance from the focus for the XX-Es: water bath (———), body cavity (– – –), body cavity and kidney (–·–·–), VOXEL-MAN Group data (·····).

5.4 Strain Rate

Howard and Sturtevant studied the effect of focusing shock wave on thin membranes of tissuelike materials[48]. They show that small-scale heterogeneities in tissue will cause the strength of the focusing shock wave to vary more strongly on these small scales, and the resulting strains will be larger than those strains found in the absence of the heterogeneities. In this sense, the tissue contributes to its own damage. The authors also discuss the significance of strain rate. For high strain rates, the failure stress and the number of cycles to failure increase. The tissue becomes more resistant to failure at high strain rates. Conversely, decreased strain rates are more likely to be damaging. If small-scale heterogeneities can cause both the shock strength to vary on these small scales and can decrease the strain rates resulting from the action of the shock on the tissue, damage is more likely to occur as a result of shearing from the shock itself.

We calculated the strain rate for each lithotripter in each of the domains previously discussed: *in*

vitro, with the body cavity model alone, with the body cavity and kidney models together, and with the VOXEL-MAN Group data. We want to study how the strain changes across the different lithotripter, but even more importantly relative to this particular proposed failure mechanism, we would like to study how the strain rate is affected by the presence of the different heterogeneous materials in our simulations. We do not model heterogeneities on the scale of 10 to 100 μm like Howard and Sturtevant, and as a result we expect the effect on strain rate to be smaller than predicted in their work. However, we would like to learn how strong, if any, the effect of the heterogeneous materials on strain rate is for our simulations.

Figure 5.9 shows the maximum strain rate as a function of distance from the focus along the axis for the Dornier HM3. The *in vitro* case shows a maximum strain rate of 4.7×10^5 s^{-1} approximately 13 mm postfocus. The body cavity model alone and the body cavity and kidney models together produce maximum strain rates of 5.4×10^5 s^{-1} and 4.8×10^5 s^{-1}, respectively, both found 11 mm postfocus. The VOXEL-MAN Group data case does indeed reduce the peak strain rate found within 20 mm of the focus to 4.1×10^5 s^{-1}, which is found between 12 and 14 mm postfocus. As with the other flow variables, a more oscillatory behavior for the strain rate is observed in this case. A secondary maximum of 6×10^5 s^{-1} is found 36 mm postfocus.

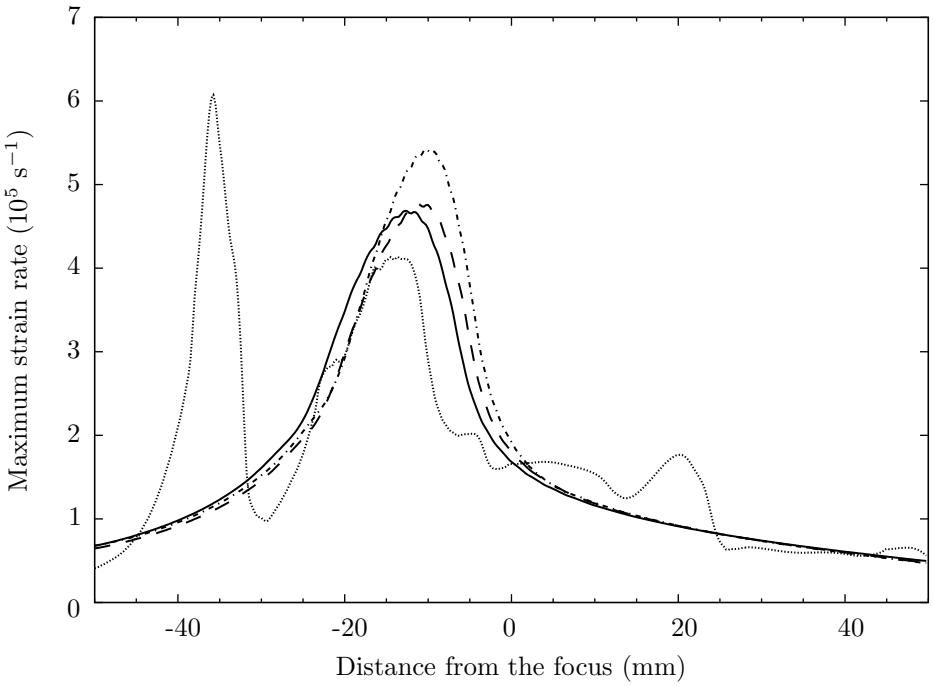

Figure 5.9: Maximum strain rate (10^5 Hz) recorded along the axis as a function of distance from the focus for the Dornier HM3: water bath (———), body cavity (– – –), body cavity and kidney (–·–·–), VOXEL-MAN Group data (·····).

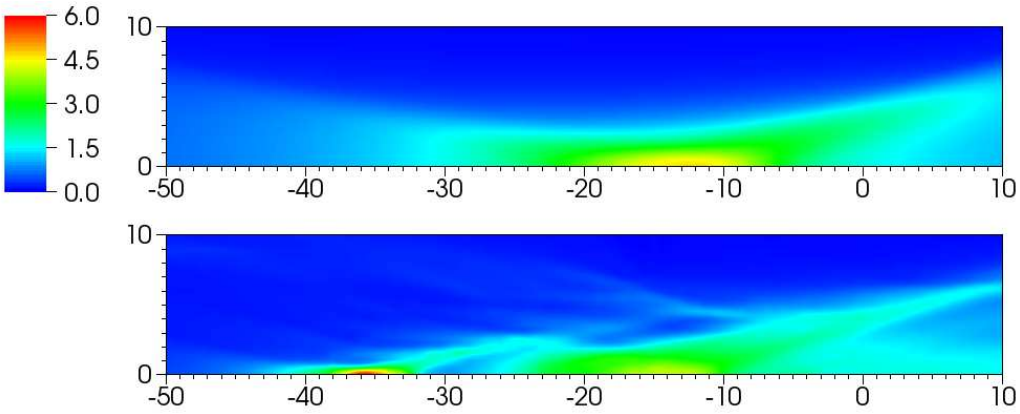

Figure 5.10: Flooded contour plot of maximum strain rate (10^5 s^{-1}) in the neighborhood of the focus for the Dornier HM3. The units of distance on the abscissa and ordinate are in mm. The focus is at (0,0). Results for the water bath case (top) and using VOXEL-MAN Group data (bottom).

Figure 5.11 shows a combined plot where both the maximum shear strain (%) and maximum strain rate (10^5 s^{-1}) are shown as a function of distance from the focus for the Dornier HM3 simulation where

the VOXEL-MAN Group data is used. The shear strain data uses the values shown on the left ordinate; the strain rate data corresponds to the right ordinate. One area of interest in the strain field is where strains are highest, but strain rates are lowest. Howard and Sturtevant explain why this region would be of interest[48]: high strains are necessary to damage tissue, but the tissue is less likely to fail at high strain rates. As a result, regions of high strain and lower strain rate would produce conditions most likely to damage tissue. Figure 5.11 shows one such area between 28 and 30 mm postfocus. The strain here is 0.6%, and the strain rate is approximately 1×10^5 s^{-1}. Even though the strain here is about 2.5 times smaller than the peak strain in this region, the strain rate is a factor of 5 below its maximum value. It is possible the tissue is most susceptible to the dynamic shear failure mechanism at this location.

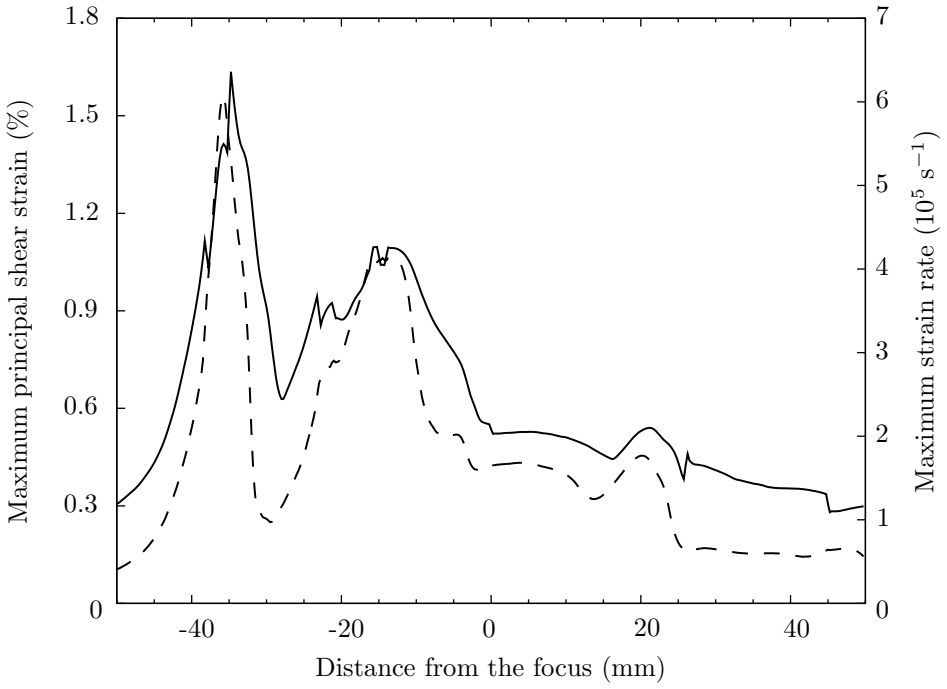

Figure 5.11: Maximum shear strain (——— , left ordinate) and maximum strain rate (– – – , right ordinate) recorded along the axis as a function of distance from the focus for the Dornier HM3 using the VOXEL-MAN Group data.

Figure 5.12 shows the maximum strain rate as a function of distance from the focus along the axis for the piezoelectric lithotripter array. All cases produce peak strain rates found between 2 and 5 mm postfocus. The *in vitro* case shows a maximum strain rate of 5.7×10^5 s^{-1}. This rate decreases by less

than 5% for the body cavity model alone and the body cavity and kidney models together. For the case where the VOXEL-MAN Group data is used, the peak strain rate increases by 10% compared with the *in vitro* case. In the region from 20 to 50 mm postfocus, the strain rate for the VOXEL-MAN Group data case is consistently less than for the other cases, with the exception of 31 to 36 mm postfocus, where a secondary, local maximum is found.

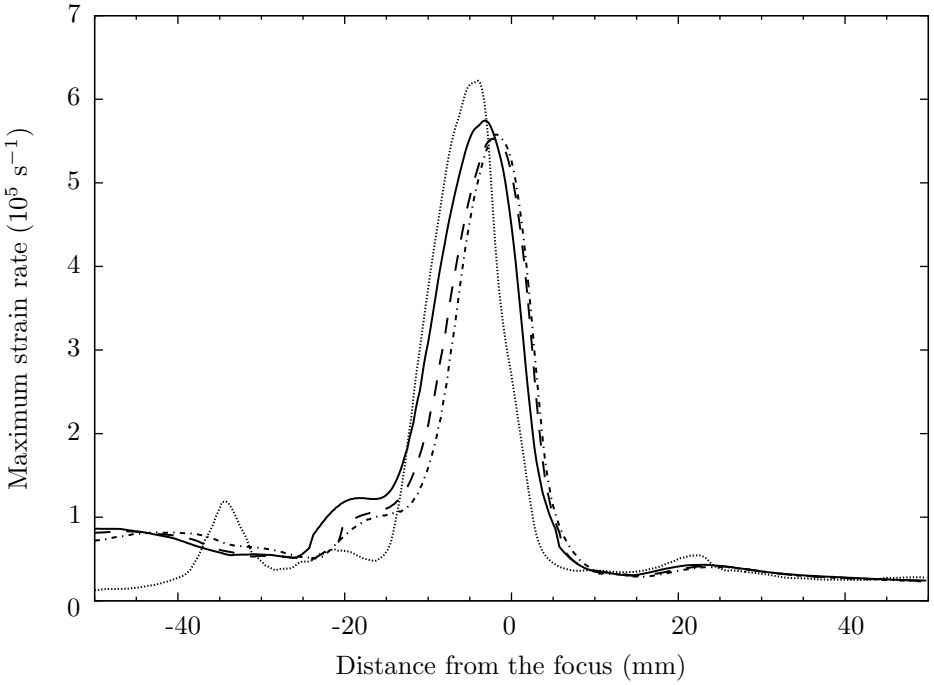

Figure 5.12: Maximum strain rate (10^5 Hz) recorded along the axis as a function of distance from the focus for the piezoelectric lithotripter array: water bath (———), body cavity (– – –), body cavity and kidney (–·–·–), VOXEL-MAN Group data (·····).

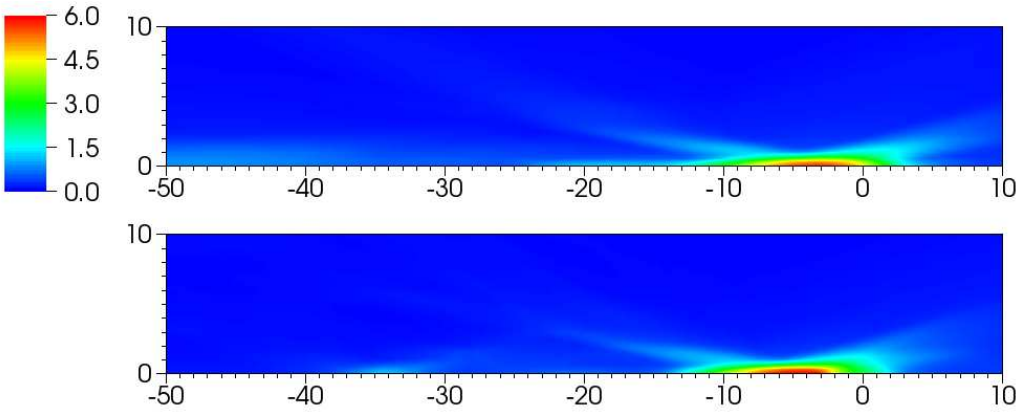

Figure 5.13: Flooded contour plot of maximum strain rate (10^5 s^{-1}) in the neighborhood of the focus for the piezoelectric lithotripter array. The units of distance on the abscissa and ordinate are in mm. The focus is at (0,0). Results for water bath case (top) and using VOXEL-MAN Group data (bottom).

Figure 5.14 shows a combined plot where both the maximum shear strain (%) and maximum strain rate (10^5 s^{-1}) are shown as a function of distance from the focus for the piezoelectric lithotripter array simulation where the VOXEL-MAN Group data is used. The shear strain data uses the values shown on the left ordinate; the strain rate data corresponds to the right ordinate. Peak values for both quantities are found approximately 5 mm postfocus. In the region between 20 and 30 mm postfocus, strains between 0.3% and 0.4% are found along with strain rates between 4×10^4 and 6×10^4 s^{-1}. Strains have thus fallen by a factor of 4 from their peak value near the focus, while strain rates have decreased by a factor of 10. This combination of relatively higher strains with relatively lower strain rates could indicate a region more susceptible to failure by a dynamic shear mechanism.

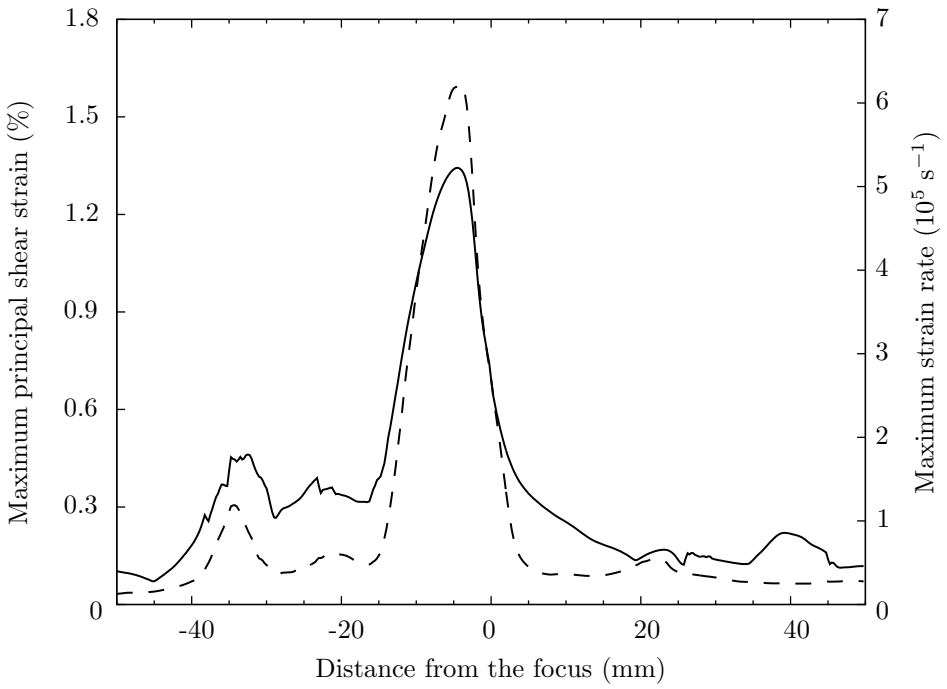

Figure 5.14: Maximum shear strain (——— , left ordinate) and maximum strain rate (– – – , right ordinate) recorded along the axis as a function of distance from the focus for the piezoelectric lithotripter array using the VOXEL-MAN Group data.

Figure 5.15 shows the maximum strain rate as a function of distance from the focus along the axis for the piezoelectric lithotripter array. The VOXEL-MAN Group cases produces strain rates that are up to 20% lower than the other cases from 10 mm prefocus to 30 mm postfocus. The global maximum strain rate on the axis is found approximately 40 mm postfocus and is over 50% larger than the local maximum found within 20 mm of the focus. Strain rates for the XX-Es are a factor of three smaller than the other lithotripters, which is an effect that potentially promotes damage via the dynamic fatigue mechanism and counters the protective effect of the lower strain estimates for this lithotripter.

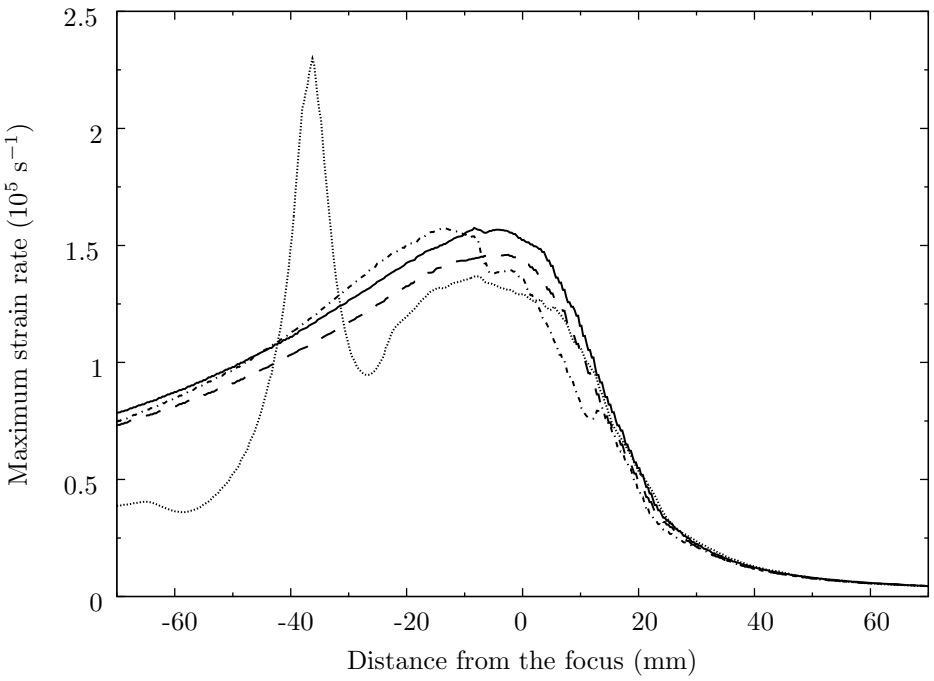

Figure 5.15: Maximum strain rate (10^5 Hz) recorded along the axis as a function of distance from the focus for XX-Es: water bath (———), body cavity (– – –), body cavity and kidney (–·–·–), VOXEL-MAN Group data (·····).

Figure 5.16 shows a combined plot where both the maximum shear strain (%) and maximum strain rate (10^5 s^{-1}) are shown as a function of distance from the focus for the XX-Es simulation where the VOXEL-MAN Group data is used. The shear strain data uses the values shown on the left ordinate; the strain rate data corresponds to the right ordinate. Regions of high strains and low strain rates are the most likely to cause damage via dynamic fatigue. In this sense, the regions from 20 to 60 mm prefocus and from 20 to 30 mm postfocus produce strains within 50% of the global maximum and strain rates 60% to 90% below the peak value. This lithotripter was designed with the primary motivation of concentrating energy at the stone site while minimizing adverse effects in surrounding tissue. It is likely from an empirical perspective that the strains in this lithotripter are sufficiently low that the calculated changes in strain rate with the introduction of heterogeneous materials would not change damage predictions from the water bath case to the VOXEL-MAN Group case.

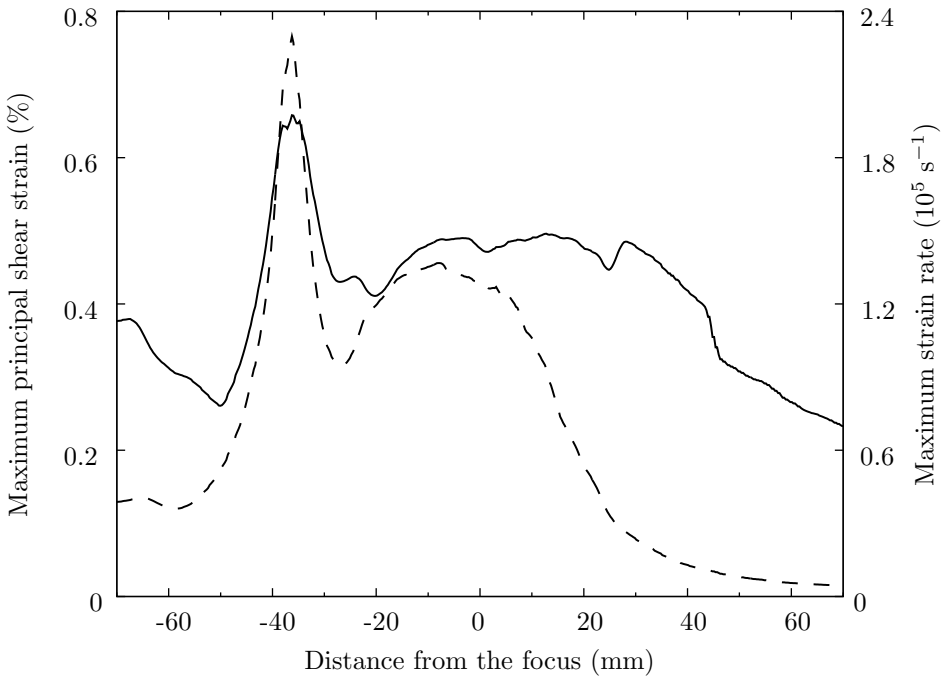

Figure 5.16: Maximum shear strain (——— , left ordinate) and maximum strain rate (– – – , right ordinate) recorded along the axis as a function of distance from the focus for the XX-Es using the VOXEL-MAN Group data.

5.5 Negative Pressure

The negative pressure contours are possibly the most robust flow feature relative to changes in the materials found in the focal region. Figure 5.17 shows the peak negative pressure in MPa as a function of distance from the focus along the axis. Use of the body cavity model alone and the body cavity and kidney models together produces little change from the *in vitro* case, where peak negative pressures around -7 MPa are found 10 mm prefocus, which is in agreement with experimental measurements[74]. The VOXEL-MAN Group data again produces a much more oscillatory structure for the negative pressures, as it does for all the flow quantities. Of greatest interest is the region 25 to 40 mm postfocus, where peak negative pressures up to -16 MPa are observed.

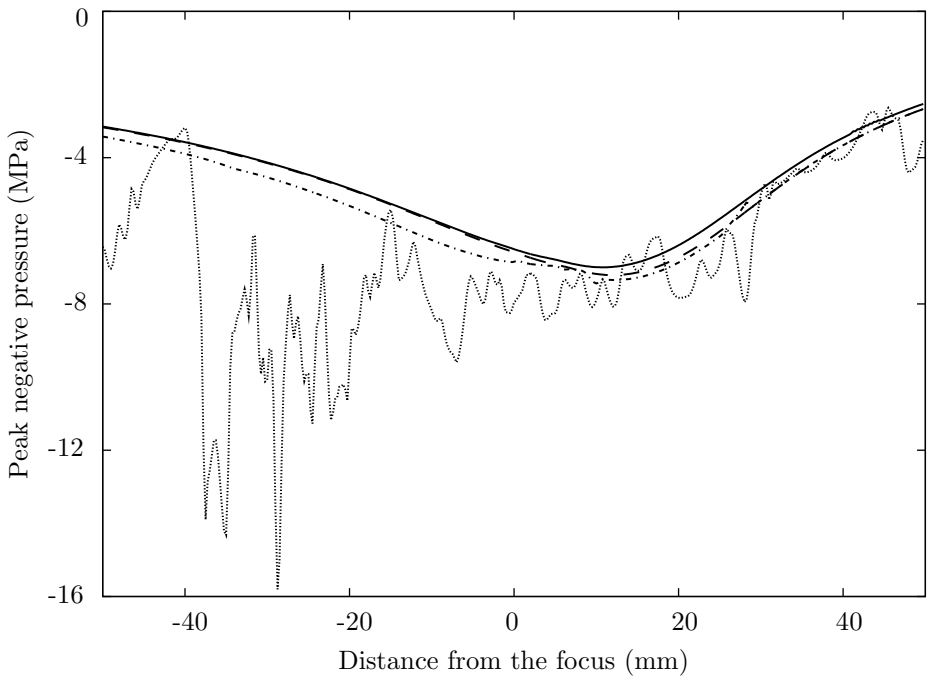

Figure 5.17: Peak negative pressure recorded along the axis as a function of distance from the focus for the Dornier HM3: water bath (———), body cavity (– – –), body cavity and kidney (–·–·–), VOXEL-MAN Group data (·····).

The largest peak negative pressures for any of the lithotripters are found in the piezoelectric lithotripter array. Figure 5.18 shows these peak negative pressures in MPa as a function of distance from the focus along the axis. In this case, pressures around -16 MPa are found within 3 mm of the focus. The body cavity and kidney models produce negative pressure contours that are very similar to the *in vitro* case. Again the VOXEL-MAN Group data produce the largest disparity. A secondary maximum in negative pressures of -12 MPa is observed 30 to 40 mm postfocus.

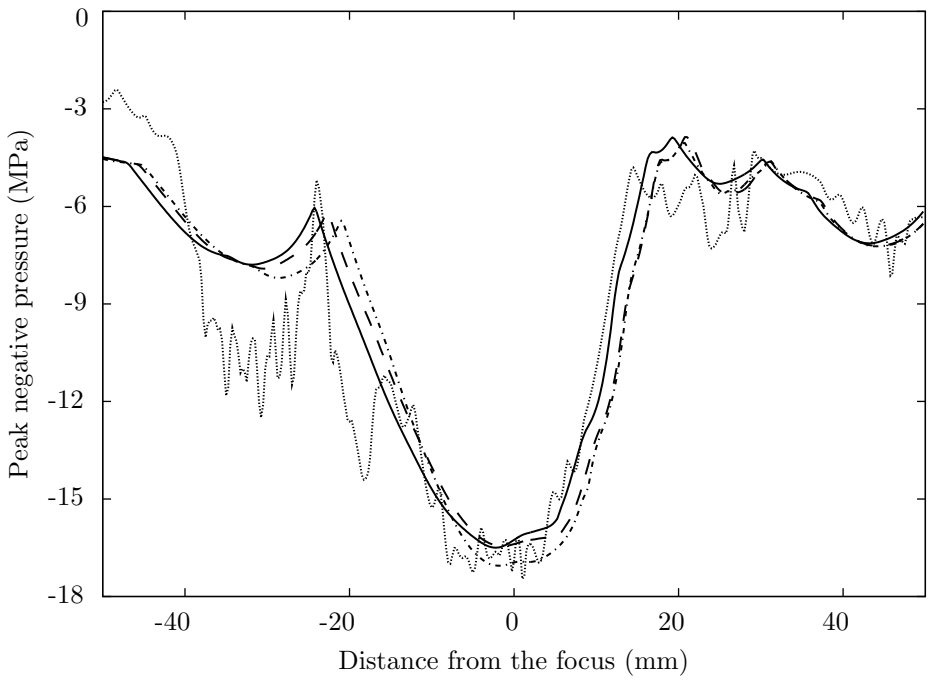

Figure 5.18: Peak negative pressure recorded along the axis as a function of distance from the focus for the piezoelectric lithotripter array: water bath (———), body cavity (– – –), body cavity and kidney (–·–·–), VOXEL-MAN Group data (·····).

Figure 5.19 shows the peak negative pressure as a function of distance from the focus along the axis for the XX-Es lithotripter. This lithotripter shows a unique trend in negative pressure where the largest amplitudes of -7 MPa are observed around 70 mm prefocus, outside the body entirely for most patients, assuming a 6 cm penetration depth from skin to focus[19]. Peak negative pressures decline nearly linearly from 70 mm prefocus to values around -3 MPa 70 mm postfocus. Our simple anatomical models produce similar results to the water bath case, while use of the VOXEL-MAN Group data produces more oscillatory results, as expected. With this data, peak negative pressures at the focus are the same as the other cases, while a local minimum near -7 MPa is found 60 mm postfocus.

These negative pressure amplitudes are slightly smaller near the focus than for the Dornier HM3 and are smaller by a factor of three compared with the piezoelectric lithotripter array. One significant deviation from the negative pressures observed in the Dornier HM3 is the secondary minimum in negative pressures for the XX-Es shows amplitudes within 2 MPa of those observed at the focus. For the Dornier HM3, the secondary peak showed amplitudes over twice as large as those seen at the focus.

Given the broad focal zone design of the XX-Es, weaker focal region gradients in the various flow quantities are expected.

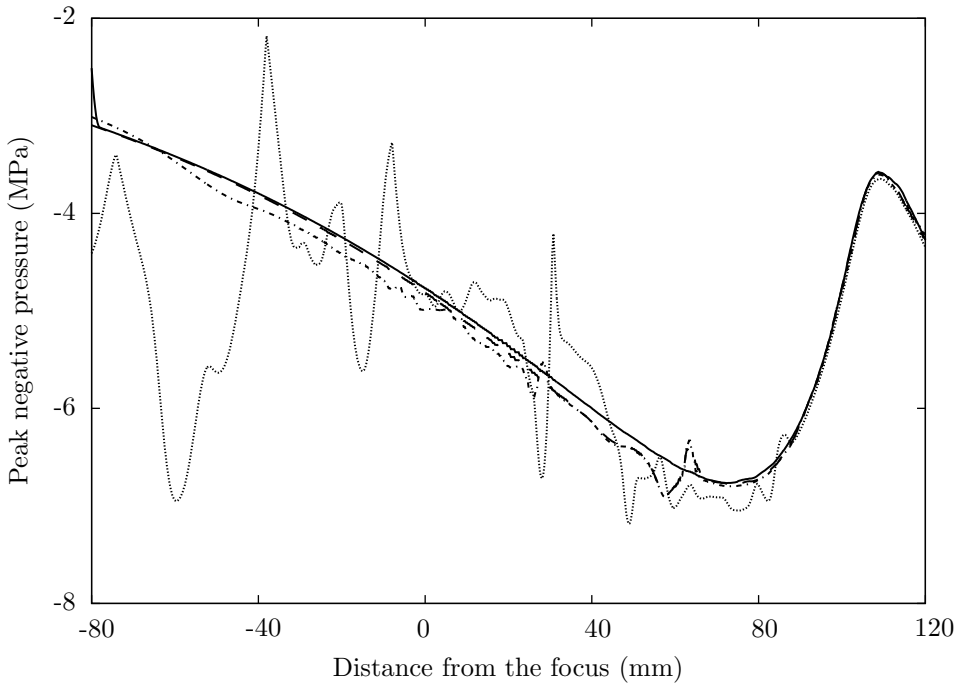

Figure 5.19: Peak negative pressure recorded along the axis as a function of distance from the focus for the XX-Es: water bath (———), body cavity (– – –), body cavity and kidney (–·–·–), VOXEL-MAN Group data (·····).

5.6 Summary

In this chapter, we discussed our approach to making estimates regarding the damage potential of the different lithotripters. We integrated the calculated velocities from our code to estimate the displacement of each fluid element, and gradients of these displacements produce strains. We rotated to the principal coordinate direction to compute the maximum principle normal strain and maximum shear strain. In addition to the strains, we took gradients of the fluid velocities to compute an estimate for the observed strain rate. Both strain and strain rate are important in making estimates about tissue failure via the dynamic fatigue mechanism. We studied the distribution of negative pressure and used this quantity as a surrogate for the potential for damage via cavitation.

Chapter 6

Conclusions

We simulated shock generation, propagation, and focusing resulting from the action of three different types of lithotripters: electrohydraulic, piezoelectric, and electromagnetic. In addition to studying wave propagation characteristics in a pure water bath for each lithotripter, we introduced heterogeneous materials in the neighborhood of the focus to investigate how the material interfaces in an *in vivo* environment would affect shock focusing.

Our conclusions are divided into two parts: observations made about (1) focal region acoustics and (2) tissue injury. We study the focal region acoustics to learn how the fundamental fluid mechanical phenomena change from one lithotripter to the next and under different configurations of materials in the focal region. We make statements about the potential for tissue injury in order to steer future investigations into techniques useful for protecting the health of the patient while still vigorously attacking kidney stones. We compute strains and strain rates and use these quantities along with peak negative pressures as surrogates for the most widely discussed mechanisms of tissue injury: shear and cavitation.

6.1 Utilization and Development of Simulation Technology

For our simulations, we used a multidimensional second-order method of the Godunov type with slope limiters and shock capturing capability to solve the inviscid Euler equations. We utilized and further developed, in the case of modeling molecular absorption, the AMROC numerical infrastructure to study shock wave lithotripsy in a novel fashion. Some of our contributions involving the technology of shock wave lithotripsy simulation are listed below.

- We used the level set capability built into the AMROC numerical infrastructure to replicate the

complex geometry of the different lithotripters. The Dornier HM3 has an ellipsoidal reflector that focuses a diverging spherical shock wave at the location of the kidney stone. The piezoelectric lithotripter array and the XX-Es both have spherical actuation surfaces that create a self-focusing shock wave. A signed distance function was prescribed for each case and used in conjunction with the Ghost Fluid Method to capture the geometry of these surfaces playing prominent roles in shock wave generation and/or focusing.

- We modeled boundary motion and calibrated with experimental data to accurately capture shock wave generation in the piezoelectric lithotripter array and the XX-Es. For the piezoelectric lithotripter array, we used a linear argument, i.e., the Rayleigh integral, to calculate the boundary motion from the experimental pressure measurements for the case where the center element alone is fired. For the XX-Es, we leveraged known displacement profiles for another electromagnetic lithotripter to estimate the boundary motion via the Gompertz function. Adjustment of the free parameters and comparison with the measured focal pressure profile eventually led us to a choice of parameters that produced a satisfactory simulation of the acoustics for this lithotripter.

- We appealed to the fundamental physics of bubble dynamics to model the vaporization event, and hence shock generation, in an electrohydraulic lithotripter. For this purpose, we used the Rayleigh-Plesset equation governing the dynamics of a single spherical bubble. Using measured collapse times for the vapor bubble produced by the electrode pair, we were able to calibrate our bubble model to replicate important features of the vaporization event. The model provided an estimate of the equivalent mass and energy that would have to be supplied by a source to mimic the behavior of a vapor bubble at this location. Inclusion of the corresponding source terms in our model allowed us to accurate model shock generation for this type of lithotripter.

- We introduced interfaces between materials of different acoustic impedances to study the effect these interfaces have on shock focusing. AMROC utilizes a multicomponent algorithm that allows for the specification of γ and p_∞, two parameters appearing in the equation of state, in a nonuniform fashion. The density can similarly be prescribed nonuniformly such that stable interfaces between materials with different acoustic impedances can be formed. These interfaces have

nontrivial effects on shock propagation and focusing, as discussed in previous chapters and in the next section.

- We augmented the classical inviscid Euler system to account for the effects of molecular absorption. The internal energy of a given fluid element was partitioned into a number of degrees of freedom that immediately attain their equilibrium value and a further number of degrees of freedom that take finite time to relax to equilibrium values. The classical inviscid Euler system was then supplemented with a finite number of relaxation equations that govern the rate at which these latter degrees of freedom relax to equilibrium energies. We state our conclusions regarding molecular absorption in the next section.

6.2 Focal Region Acoustics

We use the computed pressures and energies to characterize the focal region dynamics for each lithotripter both in a water bath and in the presence of heterogeneous materials. When taking the water bath results as a reference, our use of the VOXEL-MAN Group data changed focal region acoustics much more strongly than our simple models of the body cavity and kidney. Because the real anatomical data provided by the VOXEL-MAN Group has a larger number of acoustic impedance interfaces than our simple models, the effects of scattering are more significant and more clearly identified for this case. As a result, in this section we will compare the water bath results with those using the VOXEL-MAN Group data, with the understanding that our simple body cavity and kidney models produce much more subtle effects.

- Our results confirm the observations of previous researchers that the shock dynamics in the focal region of lithotripters exhibit the signatures of weak shock focusing. Wave fronts beyond the focus are crossed and folded, and diffraction fields behind the converging shock fronts suppress focal pressures. The size of the focal region for each lithotripter is a function of the aperture size, the strength of the converging front, and the nature of the resulting diffractive wavefield behind this front.

- Scattering from acoustic impedance interfaces affects shock propagation and focusing more than

absorption. We implemented a model where absorption is assumed to be a power law function of frequency. Because we have a time domain code, the frequency-dependent absorption was approximated with the use of two relaxation processes. Absorption has two primary effects: attenuation and dispersion. We found attenuation of focal region waveforms due to absorption was approximately 10% for all lithotripters, and the dispersion due to absorption was negligible. However, scattering of the waves from acoustic impedance interfaces produced changes in amplitudes of as much as 25%, and when the VOXEL-MAN Group data is used, multiple peaks are observed in the focal waveforms.

- The flow fields of the Dornier HM3 show the greatest variability when materials with different acoustic impedances are added to the computational domain. The output of the piezoelectric lithotripter array and the XX-Es are more robust to the introduction of new materials. One primary reason for this difference is the nonuniformity in the strength of the focusing shock in the Dornier HM3. The near-axis portion of the front is considerably stronger than the farther off-axis portion, and as a result the near-axis portion contributes more dominantly to the focal region acoustics. For cases where we use our anatomical models or the VOXEL-MAN Group data, the largest number of acoustic impedance interface are found along the axis of the lithotripter. For the other two lithotripters, all parts of the converging shock front contribute roughly equally to the pressures and energies observed in the focal region, and as a result, disturbing the portion of the shock front near the axis to a greater degree than the rest of the front is less disruptive to the focal region acoustics than for the nonuniform focusing front seen in the HM3. We will discuss the specific differences between these lithotripters later in this section.

- The radial distribution of peak positive pressure changes little when heterogeneous materials are present. Sapozhnikov et al. performed a series of numerical tests studying various possible failure mechanisms in artificial cylindrical kidney stones[69]. The dominant failure mechanism in their study was dynamic squeezing, where shear waves generated at the stone edge are reinforced by the shock wave traveling in the fluid along the surface of the stone. Lithotripters with higher pressures away from the axis apply the dynamic squeezing mechanism more effectively. The size of the focal region, defined as the -6 dB contour relative to the peak pressure at the focus, is

known for each lithotripter under *in vitro* conditions. We used the 20 MPa contour to compare how the peak pressure distribution varies across the different lithotripters when heterogeneous materials are present in the focal region. While the axial extent of this contour changes from the water bath simulation to the case with heterogeneous materials, the radial extent is insensitive to these changes. As a result, we continue to expect the Dornier HM3 and XX-Es, with beam widths of 5 and 3 mm in radius, respectively, to be more effective at utilizing the dynamic squeezing mechanism than the piezoelectric lithotripter array, whose beam width is between 1 and 2 mm in radius.

- The presence of heterogeneous materials increases calculated pressures and energy densities several centimeters downstream of the focus. For all the lithotripters, pressures and energy densities within 15 mm of the focus change little in amplitude with the introduction of heterogeneous materials. In all cases the structure of axial pressures and energy densities becomes more highly oscillatory, and an additional local maximum is found 30 to 40 mm postfocus. For the Dornier HM3, this second maximum is a global maximum for pressure, where 90 MPa amplitudes are 30 MPa larger than those found closer to the focus. The energy density 30 to 40 mm postfocus is within 10% of the peak values found near the focus. For the piezoelectric lithotripter array, the amplitudes found downstream are weaker compared with focal values. The second maximum produces pressure amplitudes around 25 MPa, 10 MPa larger than what is found in the water bath case. Energy densities double from around 80 to 160 J/m^2, but these larger energy densities are still a factor of three smaller than those found near the focus. The XX-Es shows much smaller variation in pressures and energy densities than the other two lithotripters. Pressure amplitudes are largely unchanged, and a second, local maximum in energy density is found 50 to 70 mm postfocus. The energy densities double here relative to the water bath case, but amplitudes remain below those found near the focus. The higher pressures and energy densities found several centimeters downstream of the focus when heterogeneous material are used provide the increased forces and work capacity to damage tissue in this region.

6.3 Tissue Injury

Two mechanisms of soft tissue injury often discussed in the context of shock wave lithotripsy are tearing due to gradients in forces applied to the tissue, i.e., shear, and rupture of the vasculature as a result of the energetic collapse of cavitation bubbles. As a surrogate metric for the potential for tearing, we study the maximum principal normal and shear strains computed in the focal region. We integrate the computed velocities to estimate the displacement of each fluid particle. The gradients of these displacements then provide strain data. Rotating to a principal coordinate system, we can produce estimated values for the maximum principal normal and shear strains. If two regions of our domain differ only in the magnitude of their estimated strains, the region with higher strains will identify tissue more likely to be susceptible to shearing. For cavitation potential, we study the distribution of negative pressures and how this distribution changes with different configurations of heterogeneous materials in the neighborhood of the focus. Larger negative pressures are more likely to induce larger bubble growth and, hence, more energetic bubble collapse. If two regions of our domain differ only in the calculated negative pressure amplitudes, the region with stronger tensions will identify tissue more likely to be susceptible to damage via cavitation.

- Our largest strain estimates are an order of magnitude larger than those used by Freund et al[37]. The difference occurs because Freund et al. integrate the velocity fields after the focused shock completely passes through the domain. In our case, we compute strains at each moment in time and report the largest values found over the course of the simulation. In this sense, the conclusions drawn by Freund et al. can be taken as conservative in the context of the strain values we report. As the shear damage mechanism is further explored, the notions of which strains are most germane and the means of computing the most accurate estimates for these strains should become more clear.

- Maximum principal normal strains are less than the corresponding shear strains for all the lithotripters, with and without the presence of heterogeneous materials in the focal region. For the Dornier HM3, maximum principal normal strains vary from 0.25% in the water bath simulation to 0.35% when the VOXEL-MAN Group data is used. For the piezoelectric lithotripter

array, these values 0.6%, and for the XX-Es, within the body cavity of the patient, the maximum principal normal strain is at most 0.25%. The maximum shear strain amplitudes are a factor of two to five higher for each lithotripter, with values greater than 1.2% in both the Dornier HM3 and piezoelectric lithotripter array.

- Following the trend of peak pressure and energy density, the presence of heterogeneous materials produce local shear strain maxima several centimeters downstream of the focus. The peak shear strain for the Dornier HM3 within 20 mm of the focus in the water bath simulation is 1.25%. When the VOXEL-MAN Group data is used, a second, global maximum shear strain over 1.6% is observed 35 mm postfocus. Between 30 and 35 MPa, a second, local maximum shear strain of 0.45% is seen for the piezoelectric lithotripter array. When the domain contains only pure water, strains in this region are less than half of this value. The shear strain data for the XX-Es lithotripter becomes more oscillatory, but the changes in amplitude relative to the water bath simulation are not as significant as for the other lithotripters. For almost all chosen blast paths, kidney tissue will extend no more than two centimeters postfocus. These hot spots of estimated shear strain that are found three to four centimeters downstream of the focus will be in different tissue: pancreas, fat, muscle, colon, etc. These other tissue types are then potentially threatened by a treatment ostensibly isolating the kidney, a clearly undesirable side effect.

- When heterogeneous materials are used, both strains and strain rates generally decrease slightly within two centimeters of the focus. Lower strains are less likely to be damaging, but lower strain rates promote damage via the dynamic fatigue mechanism[71, 48]. When the VOXEL-MAN Group data is used, the Dornier HM3 simulation shows strain rates universally below the *in vitro* case between the focus and 30 mm postfocus. Around 8 mm postfocus, the strain rate is approximately half of its value for the same location in the water bath simulation. A local minimum strain rate is found 30 mm postfocus for this case, though a region of increased strain rate is found further downstream, corresponding with the increases in pressure, energy density, and shear strain. When the VOXEL-MAN Group data is used in the piezoelectric lithotripter array simulation, strain rates decrease relative to the *in vitro* case from 10% to 50% from 6 mm prefocus to 2 mm postfocus. A second region of decreased strain rates is observed from 14 to 30

mm postfocus. For the XX-Es, strain rates are lower than the water bath case between 5 mm prefocus and 30 mm postfocus. Between 32 and 42 mm postfocus, strain rates increase slightly. A local minimum strain rate is found 27 mm postfocus. Further investigation is needed to determine whether the trends of decreasing strain and strain rates near the focus are more or less likely to damage tissue relative to what is expected given the water bath results.

- Between two and three centimeters downstream, the presence of the heterogeneous materials tends to increase strains and decrease strain rates, the combination most likely to be damaging via the dynamic fatigue mechanism. The two strain maxima for each lithotripter, one found within one centimeter of the focus and the other found two to four centimeters downstream, are accompanied with higher strain rates. Within 5 mm of the location of the maxima, though, strain rates fall off much more rapidly than the strain amplitudes. For the Dornier HM3, the strain 30 mm postfocus is nearly the same as the water bath case, but the strain rate has decreased by almost 50%. The same trend is found for the piezoelectric lithotripter array 5 mm prefocus.

- The introduction of acoustic impedance interfaces caused peak negative pressures for the Dornier HM3 to more than double three to four centimeters downstream of the focus. For the water bath case, peak negative pressures of -7 MPa are found 10 mm prefocus. The VOXEL-MAN Group data produces similar negative pressures within one centimeter of the focus, but negative pressures 20 to 40 mm postfocus are considerably higher than for the water bath case. Peak negative pressures near -16 MPa are found 29 mm postfocus, again well out of the range where kidney tissue is expected to be found in most cases. Negative pressures are consistently below -10 MPa from 20 to 40 mm postfocus, while for the water bath case, negative pressures are typically around -4 MPa. The other two lithotripters show the same trend but with much smaller changes in amplitudes between the two cases. Negative pressures several MPa lower than the water bath cases would indicate regions that are potentially more susceptible to damage via cavitation.

6.4 Future Work

While the axisymmetric simulations discussed in this work can help identify areas where pressures, acoustic energies, and strains are strongest, a three-dimensional simulation with realistic anatomical models would be tremendously useful to explore variabilities that cannot be captured in the current simulations. It is likely that the axisymmetric cases we study provide an upper bound on the various flow quantities observed in the focal region. In the three-dimensional case, disruptions in the focusing process can occur in the azimuthal direction in addition to the radial effects we study in this work. Allowing azimuthal perturbations will further degrade the coherence of the focusing process, and a more complicated flow field with three-dimensional relevance will be found in the focal region.

In addition to lifting the axisymmetric restriction, another modeling improvement will be resolution of small-scale renal structures, e.g., tubules, veins, capillaries, small arteries, etc., which are the primary sites of injury[10]. These structures have characteristic dimensions in the range of tens to hundreds of microns[79]. In the current work, we chose a set of acoustic parameters and assigned these parameters to the entire kidney. In the future, investigators could further explore damage initiation in soft tissue if structures on these smaller scales could be sufficiently resolved and their acoustical properties allowed to vary. The work of Howard and Sturtevant[48] could be used as a motivation to couple the acoustics on the scale of the lithotripter to the anatomy on the scale of individual tubules and vascular elements. The expectation is inclusion of these smaller scale heterogeneities would increase computed strains and decrease corresponding strain rates, exactly the combination that is more likely to cause injury via shear.

Another important extension of the work in the future will be the inclusion of a cavitation model. Tanguay[76] devised a scheme where the ensemble averaged two-phase equations of Zhang and Prosperetti[86] were used to couple the bubble dynamics with the fluid mechanics computed from the integration of the fully nonlinear inviscid Euler equations. The numerical framework used in this work can be manipulated to include this same cavitation model, and the effect of the resulting bubble dynamics on the focal region acoustics could be studied in the vicinity of heterogeneous materials.

Appendix A

Modifying the model to include relaxation processes

A.1 Augmenting the Euler System

First we will present again the system of conservation laws we integrate to simulate shock propagation in the various lithotripters, both in homogeneous and heterogeneous environments. Next we will discuss how we augment the basic system to include two time-domain relaxation processes that are designed to model the absorption observed in various classes of soft tissue. We will add i equations to our system, where i is the number of relaxation processes we want to include. We use the approaches of Whitham[81] and Pierce[66], and these references contain many of the details of the formalism we describe. We have edited the Riemann solver in our code to properly couple the relaxation equations with the fully nonlinear Euler system.

A.1.1 Basic System

Our system of equations from Chapter 2, i.e. the fully nonlinear Euler equations, is

$$\frac{\partial \boldsymbol{q}}{\partial t} + \frac{\partial \boldsymbol{f}}{\partial x} + \frac{\partial \boldsymbol{g}}{\partial r} = -\frac{\boldsymbol{s_g}}{r}, \tag{A.1}$$

where t is time, x is the axial coordinate, r is the radial coordinate, $\boldsymbol{q}$ is the state vector of conserved variables, $\boldsymbol{f}$ and $\boldsymbol{g}$ are the flux vectors in the axial and radial directions, respectively, and $\boldsymbol{s_g}$ is the geometrical source term vector:

$$\boldsymbol{q} = \begin{bmatrix} \rho \\ \rho u \\ \rho v \\ \rho e_t \end{bmatrix}, \quad \boldsymbol{f} = \begin{bmatrix} \rho u \\ \rho u^2 + p \\ \rho uv \\ (\rho e_t + p)\, u \end{bmatrix}, \quad \boldsymbol{g} = \begin{bmatrix} \rho v \\ \rho uv \\ \rho v^2 + p \\ (\rho e_t + p)\, v \end{bmatrix}, \quad \boldsymbol{s_g} = \begin{bmatrix} \rho v \\ \rho uv \\ \rho v^2 \\ (\rho e_t + p)\, v \end{bmatrix}. \tag{A.2}$$

In this formalism, ρ is the fluid density, u and v are the fluid velocities in the axial and radial directions, respectively, e_t is the total specific internal energy, and p is the pressure.

The total specific energy e_t has the following definition:

$$\rho e_t = \rho e + \frac{1}{2}\rho \left(u^2 + v^2\right), \tag{A.3}$$

where e is the specific internal energy. We close this system using the stiffened gas equation of state:

$$\rho e = \frac{p + \gamma p_\infty}{\gamma - 1}, \tag{A.4}$$

where p_∞ and γ are parameters that provide thermodynamic information, e.g. the small signal sound speed, for the material. In addition to these equations, we also have two advection equations, one each for the quantities $1/(\gamma - 1)$ and $\gamma p_\infty/(\gamma - 1)$[72].

A.1.2 Augmented System

To this point we have used γ, analogous to the ratio of specific heats for a perfect gas, as one of the two parameters that characterize a material. The other such parameter is p_∞. With an appeal to statistical thermodynamics, we know the ratio of specific heats, γ, can be related to the number of degrees of freedom of a system, ν,

$$\gamma = \frac{\nu + 2}{\nu}, \tag{A.5}$$

or

$$\nu = \frac{2}{\gamma - 1}. \tag{A.6}$$

The primary assumption made in our use of various relaxation processes is that our fluid system has ν_e degrees of freedom that relax instantaneously to equilibrium conditions, while $\nu_{r,i}$ degrees of freedom take a finite time to relax, characterized by the relaxation time τ_i. In this case,

$$\nu = \nu_e + \sum_i \nu_{r,i}, \tag{A.7}$$

where again ν is the total number of degrees of freedom of our fluid system and i is the number of relaxation processes we choose to include in our model.

In this formulation, without any relaxation processes, the stiffened gas equation of state (A.4) would be written as

$$\rho e = \frac{\nu}{2} p + \left(1 + \frac{\nu}{2}\right) p_\infty. \tag{A.8}$$

Including i relaxation processes, the equation of state becomes

$$\rho e = \frac{\nu_e}{2} p + \left(1 + \frac{\nu_e}{2}\right) p_\infty + \sum_i \rho E_i, \tag{A.9}$$

where E_i is the specific energy stored in the $\nu_{r,i}$ degrees of freedom that relax to equilibrium conditions in finite time characterized by relaxation time τ_i. At the equilibrium condition, the equation of state implies

$$(\rho E_i)_{\text{equil}} = \frac{\nu_{r,i}}{2} \left(p + p_\infty\right). \tag{A.10}$$

Finally, we need a relaxation equation for each relaxation process. This equation takes the form

$$\frac{\partial \rho E_i}{\partial t} + \frac{\partial \rho E_i u}{\partial x} + \frac{\partial \rho E_i v}{\partial y} = -\frac{\rho E_i v}{r} + \frac{1}{\tau_i} \left[\frac{\nu_{r,i}}{2} \left(p + p_\infty\right) - \rho E_i\right]. \tag{A.11}$$

We can now revisit our original Euler system (A.1) and add a term for the relaxation source terms,

$$\frac{\partial \boldsymbol{q}}{\partial t} + \frac{\partial \boldsymbol{f}}{\partial x} + \frac{\partial \boldsymbol{g}}{\partial r} = -\frac{\boldsymbol{s_g}}{r} + \boldsymbol{s_r}. \tag{A.12}$$

The vectors retain their physical significance but now have i additional elements,

$$\begin{gathered}
\boldsymbol{q} = \begin{bmatrix} \rho \\ \rho u \\ \rho v \\ \rho e_t \\ \rho E_i \end{bmatrix}, \quad \boldsymbol{f} = \begin{bmatrix} \rho u \\ \rho u^2 + p \\ \rho uv \\ (\rho e_t + p)\, u \\ \rho E_i u \end{bmatrix}, \quad \boldsymbol{g} = \begin{bmatrix} \rho v \\ \rho uv \\ \rho v^2 + p \\ (\rho e_t + p)\, v \\ \rho E_i v \end{bmatrix}, \\
\boldsymbol{s_g} = \begin{bmatrix} \rho v \\ \rho uv \\ \rho v^2 \\ (\rho e_t + p)\, v \\ \rho E_i v \end{bmatrix}, \quad \boldsymbol{s_r} = \begin{bmatrix} 0 \\ 0 \\ 0 \\ 0 \\ \frac{1}{\tau_i}\left[\frac{\nu_{r,i}}{2}\left(p + p_\infty\right) - \rho E_i\right] \end{bmatrix}.
\end{gathered} \tag{A.13}$$

A.2 Linear Wave Equation for a Relaxing Fluid

We will begin by investigating a fluid in one dimension with a single relaxation process,

$$\frac{\partial \rho}{\partial t} + \frac{\partial \rho u}{\partial x} = 0, \tag{A.14}$$

$$\frac{\partial \rho u}{\partial t} + \frac{\partial \rho u^2}{\partial x} + \frac{\partial p}{\partial x} = 0, \tag{A.15}$$

$$\frac{\partial \rho e_t}{\partial t} + \frac{\partial \rho e_t u}{\partial x} + \frac{\partial p u}{\partial x} = 0, \tag{A.16}$$

$$\frac{\partial \rho E}{\partial t} + \frac{\partial \rho E u}{\partial x} = \frac{1}{\tau}\left(\rho E_{\text{equil}} - \rho E\right), \tag{A.17}$$

where all the variables retain their previously stated meanings. The linearized version of these four equations are

$$\frac{\partial \rho'}{\partial t} + \rho_0 \frac{\partial u'}{\partial x} = 0, \tag{A.18}$$

$$\rho_0 \frac{\partial u'}{\partial t} + \frac{\partial p'}{\partial x} = 0, \tag{A.19}$$

$$\rho_0 \frac{\partial e_t'}{\partial t} + e_{t,0} \frac{\partial \rho'}{\partial t} + \rho_0 e_{t,0} \frac{\partial u'}{\partial x} + p_0 \frac{\partial u'}{\partial x} = 0, \tag{A.20}$$

$$\rho_0 \frac{\partial E'}{\partial t} + E_0 \frac{\partial \rho'}{\partial t} + \rho_0 E_0 \frac{\partial u'}{\partial x} = \frac{1}{\tau} \left[\frac{\nu_r}{2} (p + p_\infty) - \rho E \right], \tag{A.21}$$

where we have substituted $\rho = \rho_0 + \rho'$, $u = u'$, $p = p_0 + p'$, $e_t = e_{t,0} + e_t'$, and $E = E_0 + E'$. In this formalism, the quantities with subscript zero, e.g. ρ_0, are ambient values that are spatially uniform and temporally constant. The primed quantities, e.g. ρ', are all small disturbances relative to the ambient state that generally vary in space and time, and we discard terms second order and higher in the primed quantities. Taking the definition of the total energy per unit volume and using the stiffened gas equation of state, we can derive the expression relating the small disturbances in the various flow variables,

$$\rho e_t = \rho e + \frac{1}{2} \rho u^2, \tag{A.22}$$

$$\rho e_t = \frac{\nu_e}{2} p + \left(1 + \frac{\nu_e}{2} \right) p_\infty + \rho E + \frac{1}{2} \rho u^2, \tag{A.23}$$

$$\rho_0 e_t' + \rho' e_{t,0} = \frac{\nu_e}{2} p' + \rho_0 E' + \rho' E_0. \tag{A.24}$$

Substituting this relation into the linearized energy equation, (A.20), gives us

$$\frac{\nu_e}{2} \frac{\partial p'}{\partial t} + \rho_0 \frac{\partial E'}{\partial t} + E_0 \frac{\partial \rho'}{\partial t} + (\rho_0 e_{t,0} + p_0) \frac{\partial u'}{\partial x} = 0. \tag{A.25}$$

Using the relaxation equation, (A.21), we now have

$$\frac{\nu_e}{2} \frac{\partial p'}{\partial t} + \frac{1}{\tau} \left[\frac{\nu_r}{2} (p + p_\infty) - \rho E \right] + (\rho_0 e_{t,0} + p_0 - \rho_0 E_0) \frac{\partial u'}{\partial x} = 0. \tag{A.26}$$

Taking the partial derivative of this expression with respect to t, and keeping quantities up to and

including first order in the small disturbances, yields

$$\frac{\nu_e}{2}\frac{\partial^2 p'}{\partial t^2} + \frac{1}{\tau}\left[\frac{\nu_r}{2}\frac{\partial p'}{\partial t} - \rho_0\frac{\partial E'}{\partial t} - E_0\frac{\partial \rho'}{\partial t}\right] + \left(\rho_0 e_{t,0} + p_0 - \rho_0 E_0\right)\frac{\partial^2 u'}{\partial t \partial x} = 0. \tag{A.27}$$

Now we can use the partial derivative with respect to x of the linearized momentum equation, (A.19), to substitute for $\partial^2 u'/\partial t \partial x$,

$$\frac{\nu_e}{2}\frac{\partial^2 p'}{\partial t^2} + \frac{1}{\tau}\left(\frac{\nu_r}{2}\frac{\partial p'}{\partial t} - \rho_0\frac{\partial E'}{\partial t} - E_0\frac{\partial \rho'}{\partial t}\right) - \left(\frac{\rho_0 e_{t,0} + p_0 - \rho_0 E_0}{\rho_0}\right)\frac{\partial^2 p'}{\partial x^2} = 0. \tag{A.28}$$

We will now rearrange terms to move closer to a recognizable wave equation,

$$\frac{\partial^2 p'}{\partial t^2} - \frac{2}{\nu_e}\left(\frac{\rho_0 e_{t,0} + p_0 - \rho_0 E_0}{\rho_0}\right)\frac{\partial^2 p'}{\partial x^2} + \frac{2}{\tau\nu_e}\left(\frac{\nu_r}{2}\frac{\partial p'}{\partial t} - \rho_0\frac{\partial E'}{\partial t} - E_0\frac{\partial \rho'}{\partial t}\right) = 0. \tag{A.29}$$

Using the definition of total energy per unit volume with the stiffened gas equation of state, we can derive an expression relating the ambient state variables,

$$\rho_0 e_{t,0} = \frac{\nu_e}{2}p_0 + \left(1 + \frac{\nu_e}{2}\right)p_\infty + \rho_0 E_0. \tag{A.30}$$

Substituting (A.30) into (A.29), we have

$$\frac{\partial^2 p'}{\partial t^2} - \left(1 + \frac{2}{\nu_e}\right)\left(\frac{p_0 + p_\infty}{\rho_0}\right)\frac{\partial^2 p'}{\partial x^2} + \frac{2}{\tau\nu_e}\left(\frac{\nu_r}{2}\frac{\partial p'}{\partial t} - \rho_0\frac{\partial E'}{\partial t} - E_0\frac{\partial \rho'}{\partial t}\right) = 0. \tag{A.31}$$

Using the definition of the frozen sound speed, c_f, for a fluid obeying the stiffened gas equation of state,

$$c_f^2 = \left(1 + \frac{2}{\nu_e}\right)\frac{p_0 + p_\infty}{\rho_0}, \tag{A.32}$$

we get

$$\frac{\partial^2 p'}{\partial t^2} - c_f^2\frac{\partial^2 p'}{\partial x^2} + \frac{2}{\tau\nu_e}\left(\frac{\nu_r}{2}\frac{\partial p'}{\partial t} - \rho_0\frac{\partial E'}{\partial t} - E_0\frac{\partial \rho'}{\partial t}\right) = 0. \tag{A.33}$$

Using the version of the linearized energy equation into which the equation of state has been substituted, (A.25), we can substitute for $-\rho_0\partial E'/\partial t - E_0\partial\rho'/\partial t$ in the previous expression,

$$\frac{\partial^2 p'}{\partial t^2} - c_f^2 \frac{\partial^2 p'}{\partial x^2} + \frac{2}{\tau \nu_e} \left[\frac{\nu_r}{2} \frac{\partial p'}{\partial t} + \frac{\nu_e}{2} \frac{\partial p'}{\partial t} + (\rho_0 e_{t,0} + p_0) \frac{\partial u'}{\partial x} \right] = 0. \tag{A.34}$$

Taking the partial derivative of this expression with respect to t, and again using the partial derivative with respect to x of the linearized momentum equation, (A.19) to substitute for $\partial u'/\partial t \partial x$, we have

$$\frac{\partial}{\partial t} \left(\frac{\partial^2 p'}{\partial t^2} - c_f^2 \frac{\partial^2 p'}{\partial x^2} \right) + \frac{2}{\tau \nu_e} \left[\frac{\nu}{2} \frac{\partial^2 p'}{\partial t^2} - \left(\frac{\rho_0 e_{t,0} + p_0}{\rho_0} \right) \frac{\partial p'}{\partial x^2} \right] = 0. \tag{A.35}$$

We can again rearrange terms,

$$\frac{\nu_e}{\nu} \tau \frac{\partial}{\partial t} \left(\frac{\partial^2 p'}{\partial t^2} - c_f^2 \frac{\partial^2 p'}{\partial x^2} \right) + \frac{\partial^2 p'}{\partial t^2} - \frac{2}{\nu} \left(\frac{\rho_0 e_{t,0} + p_0}{\rho_0} \right) \frac{\partial p'}{\partial x^2} = 0. \tag{A.36}$$

We will make use of the equation of state for the ambient flow variables here, recognizing

$$\rho_0 E_0 = \frac{\nu_r}{2} \left(p_0 + p_\infty \right), \tag{A.37}$$

so that we now have

$$\frac{\nu_e}{\nu} \tau \frac{\partial}{\partial t} \left(\frac{\partial^2 p'}{\partial t^2} - c_f^2 \frac{\partial^2 p'}{\partial x^2} \right) + \frac{\partial^2 p'}{\partial t^2} - \left(1 + \frac{2}{\nu} \right) \left(\frac{p_0 + p_\infty}{\rho_0} \right) \frac{\partial p'}{\partial x^2} = 0. \tag{A.38}$$

Given the definition of the equilibrium sound speed for this fluid, c_0,

$$c_0^2 = \left(1 + \frac{2}{\nu} \right) \frac{p + p_\infty}{\rho_0}, \tag{A.39}$$

we finally have the linearized wave equation for a relaxing fluid,

$$\boxed{\frac{\nu_e}{\nu} \tau \frac{\partial}{\partial t} \left(\frac{\partial^2 p'}{\partial t^2} - c_f^2 \frac{\partial^2 p'}{\partial x^2} \right) + \frac{\partial^2 p'}{\partial t^2} - c_0^2 \frac{\partial p'}{\partial x^2} = 0.} \tag{A.40}$$

This wave equation, (A.40), is the same as equation (C-4) in the acoustics book by Blackstock[9], with the addition of the ν_e/ν term. We could redefine τ to include this term and have an identical form of this equation.

With this wave equation, we can follow Blackstock with the derivation of the associated dispersion

relation[9]. This dispersion relation is, of course, identical the one derived for a relaxing fluid by Pierce in Section 10-8 of his book [67]. Pierce augments this dispersion relation in Section 11-6 of his book to account for nonlinear distortion. The ultimate result is the form of the KZK equation used by Yang and Cleveland[84], whose attenuation model we have used in this work. The details of these derivations can be found in the cited references.

Appendix B

Modifying the Riemann Solver to Include Relaxation Processes

We will use the two dimensional Euler equations as a model system to demonstrate the modifications to the Riemann solver necessary to account for the effects of a single relaxation process:

$$\frac{\partial \boldsymbol{q}}{\partial t} + \frac{\partial \boldsymbol{f}}{\partial x} + \frac{\partial \boldsymbol{g}}{\partial y} = 0, \tag{B.1}$$

where $\boldsymbol{f}$, the flux vector in the x direction, is

$$\boldsymbol{f} = \begin{bmatrix} \rho u \\ \rho u^2 + p \\ \rho uv \\ (\rho e_t + p)\, u \\ \rho E u \end{bmatrix}. \tag{B.2}$$

The total energy per unit volume is defined to be

$$\rho e_t = \rho e + \frac{1}{2}\rho \left(u^2 + v^2\right), \tag{B.3}$$

where ρe is the internal energy per unit volume. We use the stiffened gas equation of state,

$$\rho e = \frac{\nu_e}{2} p + \left(1 + \frac{\nu_e}{2}\right) p_s + \rho E. \tag{B.4}$$

As described previously, ν_e is the number of degrees of freedom that relax instantaneously to equilibrium

values. Through an appeal to statistical mechanics, we can relate ν, the total number of degrees of freedom of our system, to the ratio of specific heats, γ, by

$$\frac{\nu}{2} = \frac{1}{\gamma - 1}. \tag{B.5}$$

Some of these degrees of freedom, ν_e, relax instantaneously to equilibrium values. The remaining degrees of freedom, ν_r, take a finite time to relax to equilibrium values,

$$\nu = \nu_e + \nu_r. \tag{B.6}$$

With the stiffened gas equation of state, the total energy per unit volume is now

$$\rho e_t = \frac{\nu_e}{2} p + \left(1 + \frac{\nu_e}{2}\right) p_s + \frac{1}{2}\rho\left(u^2 + v^2\right) + \rho E. \tag{B.7}$$

Rearranging to solve for the pressure, p, yields

$$p = \frac{2}{\nu_e}\left[\rho e_t - \frac{1}{2}\rho\left(u^2 + v^2\right) - \rho E - \left(1 + \frac{\nu_e}{2}\right) p_s\right], \tag{B.8}$$

or in terms of conserved variables,

$$p = \frac{1}{q_6}\left(q_4 - \frac{1}{2}\frac{q_2^2 + q_3^2}{q_1} - q_5 - q_7\right), \tag{B.9}$$

where the conservative variable vector of state is given as

$$\boldsymbol{q} = \begin{bmatrix} q_1 \\ q_2 \\ q_3 \\ q_4 \\ q_5 \\ q_6 \\ q_7 \end{bmatrix} = \begin{bmatrix} \rho \\ \rho u \\ \rho v \\ \rho e_t \\ \rho E \\ \frac{\nu_e}{2} \\ \left(1 + \frac{\nu_e}{2}\right) p_s \end{bmatrix}. \tag{B.10}$$

The final two variables in the vector $\boldsymbol{q}$ are not actually conserved, which is why $\boldsymbol{q}$ has seven elements while $\boldsymbol{f}$ only has five. These two additional elements are the advected quantities associated with the equation of state, the details of which are further described by Shyue[72]. They cannot be represented via the conservation law. The flux vector in the x direction, $\boldsymbol{f}$, in conservative variables becomes

$$\boldsymbol{f} = \begin{bmatrix} q_2 \\ \frac{q_2^2}{q_1} + \frac{1}{q_6}\left(q_4 - \frac{1}{2}\frac{q_2^2+q_3^2}{q_1} - q_5 - q_7\right) \\ \frac{q_2 q_3}{q_1} \\ \left[q_4 + \frac{1}{q_6}\left(q_4 - \frac{1}{2}\frac{q_2^2+q_3^2}{q_1} - q_5 - q_7\right)\right]\frac{q_2}{q_1} \\ \frac{q_2 q_5}{q_1} \end{bmatrix}. \tag{B.11}$$

We now need to compute the elements of the flux Jacobian in the x direction, $\boldsymbol{A} = \partial \boldsymbol{f}/\partial \boldsymbol{q}$,

$$\frac{\partial \boldsymbol{q}}{\partial t} + \boldsymbol{A}\frac{\partial \boldsymbol{q}}{\partial x} + \boldsymbol{B}\frac{\partial \boldsymbol{q}}{\partial y} = 0, \tag{B.12}$$

where $\boldsymbol{B} = \partial \boldsymbol{q}/\partial y$ is the flux Jacobian in the y direction.

The last two rows of $\boldsymbol{A}$ are set with the knowledge that q_6 and q_7 advect with the fluid. Separated into columns, where A_i is the ith column, the flux Jacobian is

$$A_1 = \begin{bmatrix} 0 \\ -\frac{q_2^2}{q_1^2} + \frac{1}{2}\frac{q_2^2+q_3^2}{q_6 q_1^2} \\ -\frac{q_2 q_3}{q_1^2} \\ \frac{1}{2}\frac{q_2^2+q_3^2}{q_6 q_1^2}\frac{q_2}{q_1} - \left[q_4 + \frac{1}{q_6}\left(q_4 - \frac{1}{2}\frac{q_2^2+q_3^2}{q_1} - q_5 - q_7\right)\right]\frac{q_2}{q_1^2} \\ -\frac{q_2 q_5}{q_1^2} \\ 0 \\ 0 \end{bmatrix}, \tag{B.13}$$

$$A_2 = \begin{bmatrix} 1 \\ 2\frac{q_2}{q_1} - \frac{q_2}{q_6 q_1} \\ \frac{q_3}{q_1} \\ \left[q_4 + \frac{1}{q_6}\left(q_4 - \frac{1}{2}\frac{q_2^2+q_3^2}{q_1} - q_5 - q_7\right)\right]\frac{1}{q_1} - \frac{q_2}{q_6 q_1}\frac{q_2}{q_1} \\ \frac{q_5}{q_1} \\ 0 \\ 0 \end{bmatrix}, \tag{B.14}$$

$$A_3 = \begin{bmatrix} 0 \\ -\frac{q_3}{q_6 q_1} \\ \frac{q_2}{q_1} \\ -\frac{q_3 q_2}{q_6 q_1^2} \\ 0 \\ 0 \\ 0 \end{bmatrix}, \quad A_4 = \begin{bmatrix} 0 \\ \frac{1}{q_6} \\ 0 \\ \frac{q_2}{q_1} + \frac{q_2}{q_6 q_1} \\ 0 \\ 0 \\ 0 \end{bmatrix}, \quad A_5 = \begin{bmatrix} 0 \\ -\frac{1}{q_6} \\ 0 \\ -\frac{q_2}{q_6 q_1} \\ \frac{q_2}{q_1} \\ 0 \\ 0 \end{bmatrix}, \tag{B.15}$$

$$A_6 = \begin{bmatrix} 0 \\ -\frac{1}{q_6^2}\left(q_4 - \frac{1}{2}\frac{q_2^2+q_3^2}{q_1} - q_5 - q_7\right) \\ 0 \\ -\frac{q_2}{q_6^2 q_1}\left(q_4 - \frac{1}{2}\frac{q_2^2+q_3^2}{q_1} - q_5 - q_7\right) \\ 0 \\ u \\ 0 \end{bmatrix}, \quad A_7 = \begin{bmatrix} 0 \\ -\frac{1}{q_6} \\ 0 \\ -\frac{q_2}{q_6 q_1} \\ 0 \\ 0 \\ u \end{bmatrix}. \tag{B.16}$$

We can simplify one of the often repeated expressions by introducing the enthalpy, h:

$$\begin{aligned} &\frac{1}{q_1}\left[q_4 + \frac{1}{q_6}\left(q_4 - \frac{1}{2}\frac{q_2^2+q_3^2}{q_1} - q_5 - q_7\right)\right] \\ =&\frac{1}{\rho}\left\{\rho e_t + \frac{2}{\nu_e}\left[\rho e_t - \frac{1}{2}\rho\left(u^2+v^2\right) - \rho E - \left(1+\frac{\nu_e}{2}\right)p_s\right]\right\} = e_t + \frac{p}{\rho} = h. \end{aligned} \tag{B.17}$$

$$\boldsymbol{A} = \begin{bmatrix} 0 & 1 & 0 & 0 & 0 & 0 & 0 \\ -u^2 + \frac{1}{\nu_e}\left(u^2+v^2\right) & 2u - \frac{2u}{\nu_e} & -\frac{2v}{\nu_e} & \frac{2}{\nu_e} & -\frac{2}{\nu_e} & -\frac{2p}{\nu_e} & -\frac{2}{\nu_e} \\ -uv & v & u & 0 & 0 & 0 & 0 \\ \frac{u}{\nu_e}\left(u^2+v^2\right) - uh & h - \frac{2}{\nu_e}u^2 & -\frac{2}{\nu_e}uv & u + \frac{2}{\nu_e}u & -\frac{2}{\nu_e}u & -\frac{2}{\nu_e}up & -\frac{2}{\nu_e}u \\ -uE & E & 0 & 0 & u & 0 & 0 \\ 0 & 0 & 0 & 0 & 0 & u & 0 \\ 0 & 0 & 0 & 0 & 0 & 0 & u \end{bmatrix} \tag{B.18}$$

Making the substitution

$$h = \frac{\nu_e}{2}c_f^2 + \frac{1}{2}\left(u^2+v^2\right) + E, \tag{B.19}$$

the eigenvectors of A are

$$r_1 = \begin{bmatrix} 1 \\ u - c_f \\ v \\ h - uc_f \\ E \\ 0 \\ 0 \end{bmatrix}, \quad r_2 = \begin{bmatrix} 1 \\ u \\ v \\ \frac{1}{2}(u^2 + v^2) \\ 0 \\ 0 \\ 0 \end{bmatrix}, \quad r_3 = \begin{bmatrix} 0 \\ 0 \\ 1 \\ v \\ 0 \\ 0 \\ 0 \end{bmatrix},$$

$$r_4 = \begin{bmatrix} 1 \\ u + c_f \\ v \\ h + uc_f \\ E \\ 0 \\ 0 \end{bmatrix}, \quad r_5 = \begin{bmatrix} 0 \\ 0 \\ 0 \\ 1 \\ 1 \\ 0 \\ 0 \end{bmatrix}, \quad r_6 = \begin{bmatrix} 0 \\ 0 \\ 0 \\ p \\ 0 \\ 1 \\ 0 \end{bmatrix}, \quad r_7 = \begin{bmatrix} 0 \\ 0 \\ 0 \\ 1 \\ 0 \\ 0 \\ 1 \end{bmatrix}, \tag{B.20}$$

where the associated eigenvalues are

$$\lambda_1 = u - c_f, \quad \lambda_2 = \lambda_3 = u, \quad \lambda_4 = u + c_f, \quad \lambda_5 = \lambda_6 = \lambda_7 = u. \tag{B.21}$$

For a given Riemann problem, the jump between left and right hand states is given as

$$\Delta q = q_R - q_L = \sum_{k=1}^{7} \alpha_k r_k, \tag{B.22}$$

where the solution for the scalar α_k, the strength of the kth discontinuity, can be computed using this relation. The remaining details follow the analysis of Shyue[72].

Appendix C

Verification of relaxation implementation

In order to verify our implementation of the relaxation processes, we performed simulations of planar acoustic wavetrains of different frequencies each traveling a distance of 40 wavelengths. The three frequencies we chose were 100 kHz, 1 MHz, and 10 MHz. In the work of Yang and Cleveland[84], where the details of these relaxation processes were developed, an attenuation power law was approximated by the behavior of two relaxation processes over the frequency band of 100 kHz to 30 MHz. Our frequency choices thus produce three frequencies of three different orders of magnitude within this range.

In the acoustics book of Blackstock[9], expressions are given for both the phase velocity and attenuation in a relaxing fluid. The phase velocity, $c_{ph,r}$, for a monorelaxing fluid, according to equation C-11b in Blackstock, is

$$\frac{c_{ph,r}}{c_0} = \sqrt{\frac{1+\omega^2\tau_r^2\left(1+m_r\right)^2}{1+\omega^2\tau_r^2\left(1+m_r\right)}}, \tag{C.1}$$

where c_0 is the small signal sound speed (aka the equilibrium sound speed), ω is the frequency of the traveling wave, τ_r is the relaxation time, and m_r is the dispersion metric, as per equation C-6 in Blackstock,

$$m_r \equiv \frac{c_{\infty,r}^2 - c_0^2}{c_0^2} = \frac{c_{\infty,r}^2}{c_0^2} - 1, \tag{C.2}$$

where $c_{\infty,r}$ is the frozen sound speed associated with relaxation process r. The absorption α, as per equation C-13 in Blackstock, is

$$\alpha_r = \frac{m_r}{2c_0}\frac{\omega_r\omega^2}{\omega^2+\omega_r^2}, \tag{C.3}$$

where $\omega_r = 1/\tau_r$ is the relaxation frequency.

In our case, we have a birelaxing fluid, and we need to use linear combinations of the above expressions to find the attenuation and phase speed. In the case of the phase speed, let us discuss the phase speed increment $c'_{ph,r} = c_{ph,r} - c_0$ (i.e. the difference between the phase speed and the small signal sound speed),

$$\frac{c'_{ph,r}}{c_0} = \frac{c_{ph,r}-c_0}{c_0} = \sqrt{\frac{1+\omega^2\tau_r^2\left(1+m_r\right)^2}{1+\omega^2\tau_r^2\left(1+m_r\right)}} - 1, \tag{C.4}$$

which means the phase speed increment due to each relaxation process is

$$\frac{c'_{ph,1}}{c_0} = \sqrt{\frac{1+\omega^2\tau_1^2\left(1+m_1\right)^2}{1+\omega^2\tau_1^2\left(1+m_1\right)}} - 1, \quad \frac{c'_{ph,2}}{c_0} = \sqrt{\frac{1+\omega^2\tau_2^2\left(1+m_2\right)^2}{1+\omega^2\tau_2^2\left(1+m_2\right)}} - 1. \tag{C.5}$$

The total phase speed for a wave traveling in a fluid characterized by N relaxation processes is then (where in our case $N = 2$)

$$c_{ph} = c_0 + \sum_{r=1}^{N} c'_{ph,r} = c_0 + c'_{ph,1} + c'_{ph,2}. \tag{C.6}$$

The total attenuation due to the two relaxation processes is

$$\alpha = \sum_{r=1}^{N} \frac{m_r}{2c_0}\frac{\omega_r\omega^2}{\omega^2+\omega_r^2} = \frac{m_1}{2c_0}\frac{\omega_1\omega^2}{\omega^2+\omega_1^2}, + \frac{m_2}{2c_0}\frac{\omega_2\omega^2}{\omega^2+\omega_2^2}. \tag{C.7}$$

Table C.1 provides the values we use in our code.

Table C.1: Values for the two relaxation processes we use in our simulations, both for verification and for the results in previous chapters.

relaxation process	$c_{\infty,r} - c_0$	τ_r (ns)
1	1.3990×10^{-3}	671.54
2	1.6597×10^{-3}	42.453

We can thus compare our computed results for the attenuation of a traveling sine wavetrain in two ways. First, we can compare the amplitude of the computed waveform after it has traveled a given distance with the attenuation we would expect given (C.7). We can also time shift the computed waveform backward by using (C.4) and determine whether it overlays the initial waveform. In our case, we have a birelaxing fluid, and as a result, we use linear combinations of the above expressions to find the expected attenuation and phase velocity. Both of these comparison are shown in the plots in Figure C.1. The solid line is the initial waveform. The dashed line is the initial waveform after it has been scaled using (C.7), which provides us with the expected amplitude after the wavetrain has traveled 40 wavelengths. The dotted line is the computed waveform after it has been time shifted backward by assuming it travels with a constant speed given by (C.4). The amplitudes and temporal signatures agree nearly perfectly, which gives us confidence we have implemented the relaxation processes correctly in our code.

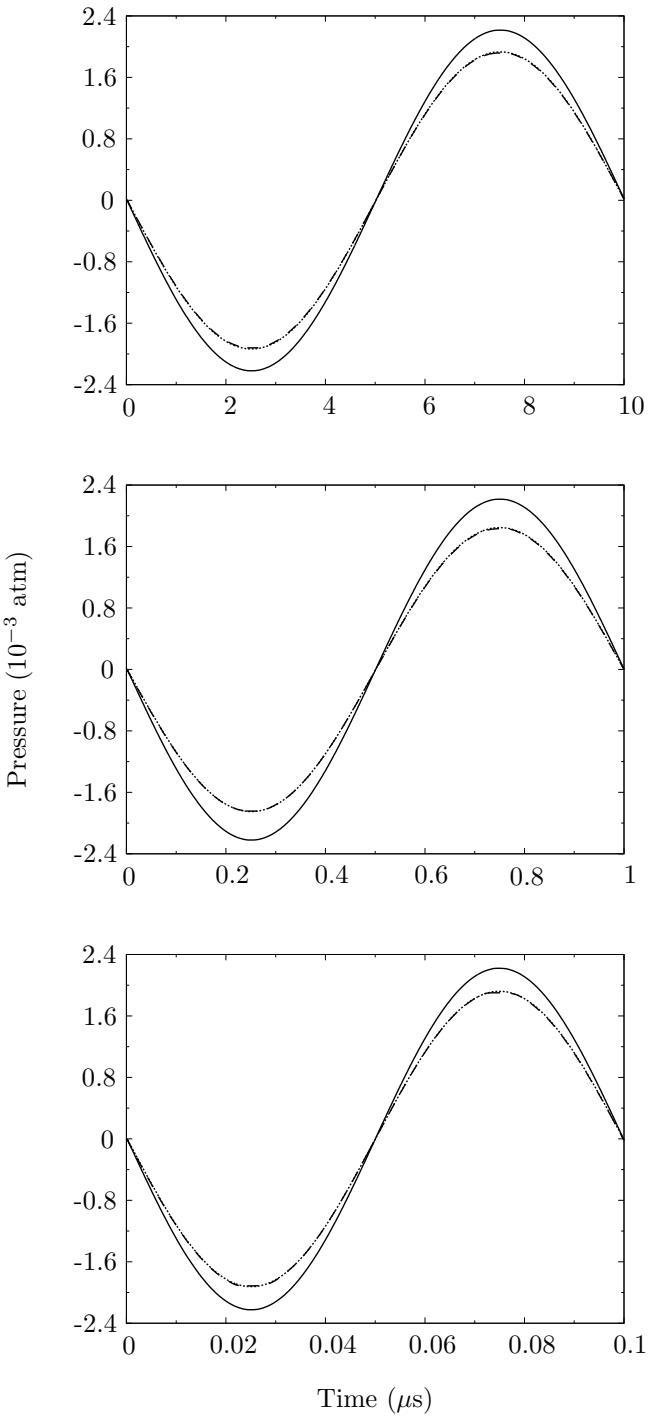

Figure C.1: Pressure (10^{-3} atm) versus time (μs) for planar sine wavetrain of three different frequencies: 100 kHz (top), 1 MHz (middle), 10 MHz (bottom). Amplitudes of the initial waveform (———), the initial waveform scaled using the closed form absorption expression (– – –), and the computed waveform after traveling 40 wavelengths (·····).

References

[1] Segmented inner organs of the Visible Human male. http://www.voxel-man.de/data/, 2010. VOXEL-MAN Group.

[2] K. S. J. W. Ackaert and F. H. Schröder. Effects of extracorporeal shock wave lithotripsy (ESWL) on renal tissue. *Urological Research*, 17:3–7, 1989.

[3] Athanasios N. Argyropoulos and David A. Tolley. Optimizing shock wave lithotripsy in the 21st century. *European Urology*, 52:344–354, 2007.

[4] Michalakis A. Averkiou and Robin O. Cleveland. Modeling of an electrohydraulic lithotripter with the KZK equation. *Journal of the Acoustical Society of America*, 106(1):102–112, 1999.

[5] Michael R. Bailey, David T. Blackstock, Robin O. Cleveland, and Lawrence A. Crum. Comparison of electrohydraulic lithotripters with rigid and pressure-release ellipsoidal reflectors. II. cavitation fields. *Journal of the Acoustical Society of America*, 106(2):1149–1160, 1999.

[6] Michael R. Bailey, Yuri A. Pishchalnikov, Oleg A. Sapozhnikov, Robin O. Cleveland, James A. McAteer, Nathan A. Miller, Irina V. Pishchalnikov, Bret A. Connors, Lawrence A. Crum, and Andrew P. Evan. Cavitation detection during shock-wave lithotripsy. *Ultrasound in Medicine & Biology*, 31(9):1245–1256, 2005.

[7] Marsha J. Berger and Joseph Oliger. Adaptive mesh refinement for hyperbolic partial differential equations. *Journal of Computational Physics*, 53:484–512, 1984.

[8] M.J. Berger and P. Colella. Local adaptive mesh refinement for shock hydrodynamics. *Journal of Computational Physics*, 82:64–84, 1989.

[9] David T. Blackstock. *Fundamentals of physical acoustics*. John Wiley & Sons, Inc., New York, 2000.

[10] Philip M. Blomgren, Bret A. Connors, James E. Lingeman, Lynn R. Willis, and Andrew P. Evan. Quantitation of shock wave lithotripsy-induced lesion in small and large pig kidneys. *The Anatomical Record*, 249:341–348, 1997.

[11] Christopher E. Brennen. *Cavitation and Bubble Dynamics*, chapter 2. Oxford University Press, New York, 1995.

[12] Edwin L. Carstensen, Kam Li, and Herman P. Schwan. Determintion of the acoustic properties of blood ands its components. *The Journal of the Acoustical Society of America*, 25(2), 1953.

[13] J.E. Cates and B. Sturtevant. Shock wave focusing using geometrical shock dynamics. *Physics of Fluids*, 9(10):3058–3068, 1997.

[14] Christian Chaussy and Egbert Schmiedt. Extracorporeal shock wave lithotripsy (ESWL) for kidney stones. An alternative to surgery? *Urologic Radiology*, 6:80–87, 1984.

[15] Christian Chaussy, Egbert Schmiedt, Dieter Jocham, Walter Brendel, Bernd Forssman, and Volker Walther. First clinical experience with extracorporeally induced destruction of kidney stones by shock wave. *The Journal of Urology*, 127:417–420, 1981.

[16] Parag V. Chitnis, Paul E. Barbone, and Robin O. Cleveland. Customization of the acoustic field produced by a piezoelectric array through interelement delays. *Journal of the Acoustical Society of America*, 123(6):4174–4185, 2008.

[17] Charles C. Church. A theoretical study of cavitation generated by an extracorporeal shock wave lithotripter. *Journal of the Acoustical Society of America*, 86(1):215–227, 1989.

[18] Robin O. Cleveland, Michael R. Bailey, Naomi Fineberg, Bruce Hartenbaum, Murtuza Lokhandwalla, James A. McAteer, and Bradford Sturtevant. Design and characterization of a research electrohydraulic lithotripter patterned after the Dornier HM3. *Review of Scientific Instruments*, 71(6):2514–2525, 2000.

[19] Robin O. Cleveland, David A. Lifshitz, Bret A. Connors, Andrew P. Evan, Lynn R. Willis, and Lawrence A. Crum. In vivo pressure measurements of lithotripsy shock waves in pigs. *Ultrasound in Medicine & Biology*, 24(2):293–306, 1998.

[20] Fredric L. Coe, Andrew Evan, and Elaine Worcester. Kidney stone disease. *The Journal of Clinical Investigation*, 115(10):2598–2608, 2005.

[21] Robert H. Cole. *Underwater Explosions*, chapter 2. Princeton University Press, Princeton, New Jersey, 1948.

[22] A.J. Coleman, M.J. Choi, and J.E. Saunders. Theoretical predictions of the acoustic pressure generated by a shock wave lithotripter. *Ultrasound in Medicine & Biology*, 17(3):245–255, 1991.

[23] A.J. Coleman and J.E. Saunders. A review of the physical properties and biological effects of the high amplitude acoustic field used in extracorporeal lithotripsy. *Ultrasonics*, 31(2):75–89, 1993.

[24] A.J. Coleman, J.E. Saunders, R.C. Preston, and D.R. Bacon. Pressure waveforms generated by a Dornier extracorporeal shock-wave lithotripter. *Ultrasound in Medicine & Biology*, 13(10):651–657, 1987.

[25] Lawrence A. Crum. Cavitation microjets as a contributory mechanism for renal calculi disintegration in ESWL. *The Journal of Urology*, 140:1587–1590, 1988.

[26] Gary C. Curhan. Epidemiology of stone disease. *Urologic Clinics in North America*, 34(3):287–293, 2007.

[27] Ralf Deiterding. *Parallel adaptive simulation of multi-dimensional detonation structures*. PhD thesis, Brandenburgische Technische Universtät Cottbus, 2003.

[28] Ralf Deiterding. Construction and application of an AMR algorithm for distributed memory computers. In Tomasz Plewa, Timur Linde, and V. Gregory Weirs, editors, *Adaptive Mesh Refinement - Theory and Applications : Proceedings of the Chicago Workshop on Adaptive Mesh Refinement Methods*, pages 361–372. Springer Berlin Heidelberg, 2005.

[29] Ralf Deiterding, Raul Radovitzky, Sean P. Mauch, Ludovic Noels, Julian C. Cummings, and Daniel I. Meiron. A virtual test facility for the efficient simulation of solid material response under strong shock and detonation wave loading. *Engineering with Computers*, 22:325–347, 2006.

[30] M. Delius. Medical applications and bioeffects of extracorporeal shock waves. *Shock Waves*, 4:55–72, 1994.

[31] Floyd Dunn, P.D. Edmonds, and W.J Fry. Absorption and dispersion of ultrasound in biological media. In H.P. Schwan, editor, *Biological Engineering*. McGraw-Hill, New York, 1969.

[32] W. Eisenmenger, X. X. Du, C. Tang, S. Zhao, Y. Wang, F. Rong, D. Dai, M. Guan, and A. Qi. The first clinical results of "wide-focus and low-pressure" ESWL. *Ultrasound in Medicine & Biology*, 28(6):769–774, 2002.

[33] Wolfgang Eisenmenger. The mechanisms of stone fragmentation in ESWL. *Ultrasound in Medicine & Biology*, 27(5):683–693, 2001.

[34] Andrew P. Evan, Fredic L. Coe, James E. Lingeman, and Elaine Worcester. Insights on the pathology of kidney stone formation. *Urological Research*, 33(5):383–389, 2005.

[35] Andrew P. Evan, Lynn R. Willis, James E. Lingeman, and James A. McAteer. Renal trauma and the risk of long-term complications in shock wave lithotripsy. *Nephron*, 78:1–8, 1998.

[36] Andrew P. Evan, Lynn R. Willis, James A. McAteer, Michael R. Bailey, Bret A. Connors, Youzhi Shao, James E. Lingeman, James C. Williams, Jr., Naomi S. Fineberg, and Lawrence A. Crum. Kidney damage and renal functional changes are minimized by waveform control that suppresses cavitation in shock wave lithotripsy. *The Journal of Urology*, 168:1556–1562, 2002.

[37] Jonathan B. Freund, Tim Colonius, and Andrew P. Evan. A cumulative shear mechanism for tissue damage initiation in shock-wave lithotripsy. *Ultrasound in Medicine & Biology*, 33(9):1495–1503, 2007.

[38] D.E. Goldman and T.F. Hueter. Tabular data for the velocity and absorption of high-frequency sound in mammalian tissues. *The Journal of the Acoustical Society of America*, 28(1):35–37, 1956.

[39] Benjamin Gompertz. On the nature of the function expressive of the law of human mortality, and on a new mode of determining the value of life contingencies. *Philosophical Transactions of the Royal Society of London*, 115:513–583, 1825.

[40] S. A. Goss, R. L. Johnston, and F. Dunn. Comprehensive compilation of empirical ultrasonic properties of mammalian tissues. *Journal of the Acoustical Society of America*, 64(2):423–457, 1978.

[41] S. A. Goss, R. L. Johnston, and F. Dunn. Compilation of empirical ultrasonic properties of mammalian tissues. II. *Journal of the Acoustical Society of America*, 68(1):93–108, 1980.

[42] B. Granz, M. Lanski, R. Nanke, M. Mahler, A. Rohwedder, C. Chaussy, and S. Thüroff. LITHOSTAR Modularis - a proven system with new, innovative features. *Electromedica*, 71(1):53–57, 2003.

[43] John W. Grove and Ralph Menikoff. Anomalous reflection of a shock wave at a fluid interface. *Journal of Fluid Mechanics*, 219:313–336, 1990.

[44] Satoshi Hamano, Hiroomi Nakatsu, Noriyuki Suzuki, Susumu Tomioka, Masashi Tanaka, and Shino Murakami. Kidney stone disease and risk factors for coronary heart disease. *International Journal of Urology*, 12:859–863, 2005.

[45] Mark F. Hamilton. Transient axial solution for the reflection of a spherical wave from a concave ellipsoidal mirror. *Journal of the Acoustical Society of America*, 93(3):1256–1266, 1993.

[46] Francis Harlow and Anthony A. Amsden. Fluid dynamics. Technical Report LA-4700, Los Alamos Scientific Laboratory, 1971.

[47] Imran Hassan and Scott P. Zietlow. Acute pancreatitis after extracorporeal shock wave lithotripsy for a renal calculus. *Urology*, 60(6):1111, 2002.

[48] Danny Howard and Bradford Sturtevant. *In vitro* study of the mechanical effects of shock-wave lithotripsy. *Ultrasound in Medicine & Biology*, 23(7):1107–1122, 1997.

[49] Jonathan I. Iloreta, Yufeng Zhou, Georgy N. Sankin, Pei Zhong, and Andrew J. Szeri. Assessment of shock wave lithotripters via cavitation potential. *Physics of Fluids*, 19:086103, 2007.

[50] Irina Ionescu, James E. Guilkey, Martin Berzins, Robert M. Kirby, and Jeffrey A. Weiss. Simulations of soft tissue failure using the material point method. *Journal of Biomechanical Engineering*, 128:917–924, 2006.

[51] Eric Johnsen. *Numerical simulations of non-spherical bubble collapse with applications to shock wave lithotripsy*. PhD thesis, California Institute of Technology, 2007.

[52] Juri V. Kaude, Clyde M. Williams, Michael R. Millner, Katherine N. Scott, and Birdwell Finlayson. Renal morphology and function immediately after extracorporeal shock-wave lithotripsy. *American Journal of Roentgenology*, 145:305–313, 1985.

[53] Joseph B. Keller. Geometrical acoustics. I. the theory of weak shock waves. *Journal of Applied Physics*, 25(8):938–947, 1954.

[54] V.P. Kuznetsov. Equations of nonlinear acoustics. *Soviet Physics Acoustics*, 16:467–470, 1971.

[55] Anna Kane Laird. Dynamics of tumor growth. *British Journal of Cancer*, 18(3):490–502, 1964.

[56] Stuart J. Laurence, R. Deiterding, and H.G. Hornung. Proximal bodies in hypersonic flow. *Journal of Fluid Mechanics*, 590:209–237, 2007.

[57] James Lighthill. *Waves in Fluids*, chapter 1-4. Cambridge University Press, New York, 1978.

[58] Murtuza Lokhandwalla, James A. McAteer, James C. Williams, Jr., and Bradford Sturtevant. Mechanical haemolysis in shock wave lithotripsy (SWL): II. *In vitro* cell lysis due to shear. *Physics in Medicine and Biology*, 46:1245–1264, 2001.

[59] Murtuza Lokhandwalla and Bradford Sturtevant. Fracture mechanics model of stone comminution in ESWL and implications for tissue damage. *Physics in Medicine and Biology*, 45:1923–1940, 2000.

[60] Attilio Losito, Emidio Giovanni Nunzi, Carla Covarelli, Elisabetta Nunzi, and Gaetano Ferrara. Increased acid excretion in kidney stone formers with essential hypertension. *Nephrology Dialysis Transplantation*, 24:137–141, 2009.

[61] George D. Ludwig. The velocity of sound through tissues and the acoustic impedance of tissues. *The Journal of the Acoustical Society of America*, 22(6):862–866, 1950.

[62] C. Pantano, R. Deiterding, D.J. Hill, and D.I. Pullin. A low numerical dissipation patch-based adaptive mesh refinment method for large-eddy simulation of compressible flows. *Journal of Computational Physics*, 221:63–87, 2007.

[63] Kevin J. Parker. Ultrasonic attenuation and absorption in liver tissue. *Ultrasound in Medicine & Biology*, 9(4):363–369, 1983.

[64] Margaret S. Pearle, Elizabeth A. Calhoun, and Gary C. Curhan. Urologic diseases in America project: Urolithiasis. *The Journal of Urology*, 173(3):848–857, 2005.

[65] Allan D. Pierce. *Acoustics: an introduction to its physical principles and applications*, chapter 5-2. McGraw-Hill Book Company, New York, 1981.

[66] Allan D. Pierce. *Acoustics: an introduction to its physical principles and applications*, chapter 10-7. McGraw-Hill Book Company, New York, 1981.

[67] Allan D. Pierce. *Acoustics: an introduction to its physical principles and applications*. McGraw-Hill Book Company, New York, 1981.

[68] Yuri A. Pishchalnikov, Joshua S. Neucks, R. Jason VonDerHaar, Irina V. Pishchalnikova, James C. Williams Jr., and James A. McAteer. Air pockets trapped during routine coupling in dry-head lithotripsy can significantly reduce the delivery of shock wave energy. *Journal of Urology*, 176(6):2706–2710, 2006.

[69] Oleg A. Sapozhnikov, Adam D. Maxwell, Brian McConaghy, and Michael R. Bailey. A mechanistic analysis of stone fracture in lithotripsy. *Journal of the Acoustical Society of America*, 121(2):1190–1202, 2007.

[70] Richard Saurel and Rémi Abgrall. A multiphase Godunov method for compressible multifluid and multiphase flows. *Journal of Computational Physics*, 150:425–467, 1999.

[71] V. Sharma, S. Nemat-Nasser, and K. S. Vecchio. Dynamic-compression fatigue of hot-pressed silicon-nitride. *Experimental Mechanics*, 34(4):315–323, 1994.

[72] Keh-Ming Shyue. An efficient shock-capturing algorithm for compressible multicomponent problems. *Journal of Computational Physics*, 142:208–242, 1998.

[73] Keh-Ming Shyue. A fluid-mixture type algorithm for compressible multicomponent flow with van der Waals equation of state. *Journal of Computational Physics*, 156:42–88, 1999.

[74] Dahlia L. Sokolov, Michael R. Bailey, Lawrence A. Crum, Philip M. Blomgren, Bret A. Connors, and Andrew P. Evan. Prefocal aligment improves stone comminution in shockwave lithotripsy. *Journal of Endourology*, 16(10):709–715, 2002.

[75] B. Sturtevant and V. A. Kulkarny. The focusing of weak shock waves. *Journal of Fluid Mechanics*, 73(4):651–671, 1976.

[76] Michel Tanguay. *Computation of bubbly cavitating flow in shock wave lithotripsy*. PhD thesis, California Institute of Technology, 2004.

[77] Eric N. Taylor, Meir J. Stampfer, and Gary C. Curhan. Obesity, weight gain, and the risk of kidney stones. *Journal of the American Medical Association*, 293(4):455–462, 2005.

[78] Philip A. Thompson. *Compressible-fluid dynamics*, chapter 2. McGraw-Hill Book Company, New York, 1972.

[79] Larry W. Welling, Matt T. Zupka, and Dan J. Welling. Mechanical properties of basement membrane. *News in Physiological Sciences*, 10(1):30–35, 1995.

[80] G.B. Whitham. A new approach to problems of shock dynamics. Part I Two-dimensional problems. *Journal of Fluid Mechanics*, 2(2):145–171, 1957.

[81] G.B. Whitham. *Linear and nonlinear waves*, chapter 10.5. John Wiley & Sons, Inc., New York, 1974.

[82] D. M. Wilbert, H. Reichenberger, G. Hutschenreiter, H. Riedmiller, P. Alken, and R. Hohenfellner. Second generation shock wave lithotripsy: experience with the Lithostar. *World Journal of Urology*, 5:225–228, 1987.

[83] R. W. Wood and A. Loomis. The physical and biological effects of high frequency sound-waves of great intensity. *Philosophical Magazine*, 4(22):417–436, 1927.

[84] Xinmai Yang and Robin O. Cleveland. Time domain simulation of nonlinear acoustic beams generated by rectangular pistons with application to harmonic imaging. *Journal of the Acoustical Society of America*, 117(1):113–123, 2005.

[85] E.A. Zabolotskaya and R.V. Khokhlov. Quasi-plane waves in the nonlinear acoustics of confined beams. *Soviet Physics Acoustics*, 15:35–40, 1969.

[86] D.Z. Zhang and A. Prosperetti. Ensemble phase-averaged equations for bubbly flows. *Physics of Fluids*, 6(9):2956–2970, 1994.

[87] Pei Zhong, Iulian Cioanta, Franklin H. Cocks, and Glenn M. Preminger. Inertial cavitation and associated acoustic emission produced during electrohydraulic shock wave lithotripsy. *Journal of the Acoustical Society of America*, 101(5):2940–2950, 1997.

[88] U. Zwergel, D. Neisius, T. Zwergel, and M. Ziegler. Results and clinical management of extracorporeal piezoelectric lithotripsy (EPL) in 1321 consecutive treatments. *World Journal of Urology*, 5:213–217, 1987.

[89] M. H. Zwietering, I. Jongenburger, F. R. Rombouts, and K. van 't Riet. Modeling of the bacterial growth curve. *Applied and Environmental Microbiology*, 56(6):1875–1881, 1990.